



TECHNISCHE  
UNIVERSITÄT  
WIEN

Vienna University of Technology

## DISSERTATION

# **Improved ground and excited states using MBPT and DFT methods within the APW framework**

ausgeführt zum Zwecke der Erlangung des akademischen Grades  
eines Doktors der technischen Wissenschaften unter der Leitung von

Ao.Univ.Prof. Dipl.-Ing. Dr.techn. Peter Blaha  
E165  
Institut für Materialchemie

eingereicht an der Technischen Universität Wien  
Fakultät für Technische Chemie

von

Ferenc Karsai, MSc  
0601442  
Belvederegasse 4  
2000 Stockerau

Wien, am 2.3.2015



## Abstract

Density functional theory (DFT) using the local density approximation or the generalized gradient approximation for the description of exchange and correlation of the electrons has been the workhorse of theoretical solid state physics since the last few decades. Although a lot of materials are described successfully using these methods, the number of cases steadily grows where standard DFT calculations are not sufficient to give accurate results. This concerns for instance ground state properties like lattice parameters of solids, in particular also excited state properties (spectroscopy), since DFT is a theory of the ground state. In this work improved exchange-correlation functionals for the electrons and many body perturbation theory methods within the full potential augmented plane wave method using the WIEN2k package are investigated and applied to selected materials and their properties, where standard DFT calculations are not accurate enough.

In the first part of this work the so called  $F$  center in lithium fluoride is investigated. The  $F$  center is the simplest type of color center, which is created, when a single fluorine atom is removed from the host crystal. Different schemes for the DFT exchange and correlation are compared such as the functionals PBE, YS-PBE0 and TB-mBJ, but also the GW method. Since the removal of a single fluorine leaves an electron of a lithium strongly localized in the vacant fluorine site, strong excitonic (or electron-hole) effects are present. These effects are included by solving the Bethe-Salpeter equation for electron-hole pairs. Additionally the results have been closely compared to quantum chemistry calculations. Very good agreement is found between our calculations using TB-mBJ and GW (plus Bethe-Salpeter corrections), quantum chemistry calculations and experiment.

In the second part the methods established for lithium fluoride have been applied to other alkali halides. The dependence of their absorption energy on the lattice parameter, or the Mollwo-Ivey relation which states that the absorption energy with respect to the lattice constant has an exponential decay, has been studied since the 1920s. Good agreement is found between our calculations and experiment. Previous investigations claimed that the Madelung potential is the main factor for the Mollwo-Ivey behavior. Our investigations prove that ion-size effects and exchange of the electrons play the major role.

The last part is dedicated to the investigation of correlation energies obtained from the adiabatic connection fluctuation dissipation theorem. This method links the response function to the correlation energy and is in principle exact. We investigate the convergence of the correlation energy within the random phase approximation. Finally geometrical properties of selected materials are

calculated and compared to former calculations and experiment. Although we find good agreement for materials, such as diamond, Ar and Kr, in many cases we have some differences to former calculations and experiment that are not negligible. The disagreements might be due to the possible neglect of core states in the calculation of the correlation energy and to incomplete basis sets for the excited states within the spheres around the atoms. Unfortunately we cannot exclude possible errors in our code.

## Übertragung des Abstracts

Dichtefunktionaltheorie (DFT) zusammen mit der lokalen Dichtenäherung (LDA) beziehungsweise der Gradientennäherung (GGA) für den Austausch und die Korrelation der Elektronen war das Zugpferd der theoretischen Festkörperphysik in den letzten Jahrzehnten. Obwohl eine Vielzahl an Materialien erfolgreich mit dieser Methode beschrieben werden kann, steigt die Anzahl der Fälle in denen DFT Rechnung nicht ausreichend genau sind stetig an. Dies betrifft Grundzustandseigenschaften wie zum Beispiel die Gitterparameter von Festkörpern, aber vor allem auch Eigenschaften abgeleitet aus angeregten Zuständen (Spektroskopie), weil DFT nur für den Grundzustand eine gültige Theorie ist. In dieser Arbeit werden verbesserte Austausch- und Korrelationsfunktionale der Elektronen beziehungsweise Methoden aus der Vielteilchenstörungstheorie im Rahmen der "Full Potential Augmented Plane Wave" (FLAPW) Methode untersucht und an ausgewählten Fällen, für welche standard DFT versagt, angewendet.

Im ersten Teil dieser Arbeit wird das so genannte  $F$ -Zentrum in Lithiumfluorid untersucht. Das  $F$ -Zentrum ist der Prototyp der Farbzentren, welches dann entsteht, wenn ein einzelnes Fluor Atom aus dem Krystallgitter entfernt wird. Mehrere verschiedene Methoden für den Austausch und die Korrelation der Elektronen werden verglichen. Unter anderem sind das die Funktionale PBE, YS-PBE0 und TB-mBJ beziehungsweise auch die GW Methode aus der Vielteilchenstörungstheorie. Da ein fehlendes Fluor Atom ein stark lokalisiertes Elektron an der Fehlstelle zurücklässt sind starke exzitonische (oder Elektron-Loch) Wechselwirkungen vorhanden. Diese Effekte werden in den Rechnungen inkludiert, indem die Bethe-Salpeter Gleichung (BSE) für Elektron-Loch Paare gelöst wird. Alle unsere Rechnungen wurden auch mit quantenchemischen Methoden verglichen. Wir finden hervorragende Übereinstimmung für unsere TB-mBJ und GW (plus BSE) Ergebnisse mit den Resultaten aus der Quantenchemie und den Experimenten.

Im zweiten Teil wurden die aus dem ersten Teil etablierten Methoden auf andere Alkalihalide angewendet. Die exponentielle Abhängigkeit ihrer Absorptionsenergie von der Gitterkonstante ist seit den 1920er Jahren unter der sogenannten Mollwo-Ivey Beziehung bekannt. Wir finden allgemein eine gute Übereinstimmung zwischen unseren und experimentellen Resultaten. Frühere Untersuchungen behaupten alle, dass das Madelung Potential die Hauptursache für das Mollwo-Ivey Verhalten ist. Unsere Ergebnisse zeigen im Gegensatz dazu, dass der Austausch der Elektronen und die Größe der Ionen den größten Einfluss haben.

Der letzte Teil befasst sich mit der Untersuchung der Korrelationsenergien

abgeleitet aus dem sogenannten "Adiabatic Connection Fluctuation Dissipation" Theorem. Diese Methode ist im Prinzip exakt und verknüpft die lineare Antwortfunktion der Elektronendichte mit der Korrelationsenergie. Wir untersuchen die Konvergenz der Korrelationsenergien im Rahmen der "Random Phase Approximation". Im Schlussteil werden die strukturellen Eigenschaften gerechnet und mit anderen Rechnungen bzw. Experimenten aus der Literatur verglichen. Obwohl wir in einigen Fällen, wie zum Beispiel für Diamant, Argon und Krypton gute Übereinstimmung finden, weichen unsere Resultate oft stark von den Literaturergebnissen ab. Die Abweichungen sind höchstwahrscheinlich mit dem Weglassen von Kernzuständen bei der Berechnung der Korrelationsenergien und von nicht vollständigen Basis Sätzen in den Sphären um die Atome herum zu erklären. Wir schließen aber auch Fehler in unserem Programm nicht aus.

## Acknowledgments

First and foremost I want to thank Professor Peter Blaha, who gave me the opportunity to work on this interesting subject and supervised my work with great dedication. He has supported me throughout this time with his patience and knowledge whilst providing me the room to work in my own way.

Special thanks goes to Professor Karl Heinz Schwarz, Dr. Fabien Tran, Dr. Robert Laskowski and Dr. David Koller who always helped me to find solutions for problems arising during my work. I also enjoyed the interesting and stimulating discussions with them.

Lastly I would like to thank my parents and my friends, who supported me during the time of my work.





# Contents

<b>1</b>	<b>Introduction</b>	<b>11</b>
1.1	DFT . . . . .	11
1.2	Basis functions . . . . .	12
1.2.1	APW method . . . . .	13
1.2.2	LAPW method . . . . .	14
1.2.3	APW+lo method . . . . .	15
1.2.4	LAPW+LO and APW+lo+LO method . . . . .	15
1.3	XC functionals . . . . .	16
1.3.1	TB-mBJ . . . . .	17
1.3.2	Hartree–Fock based methods . . . . .	18
1.3.3	Screened hybrid functionals . . . . .	18
1.4	Linear response theory . . . . .	20
1.4.1	Linear response function . . . . .	20
1.4.2	Dielectric function . . . . .	21
1.4.3	Calculation of the dielectric function . . . . .	23
1.5	Adiabatic connection fluctuation dissipation theorem . . . . .	24
1.5.1	Adiabatic connection . . . . .	24
1.5.2	Fluctuation-dissipation theorem . . . . .	25
1.5.3	Total energies within the RPA . . . . .	27
1.6	GWA . . . . .	28
1.6.1	Green’s function . . . . .	28
1.7	Quasi-particle equation . . . . .	29
1.7.1	Hedin’s equations . . . . .	29
1.7.2	GW approximation . . . . .	30
1.8	Electron-hole interactions . . . . .	32
1.8.1	Bethe–Salpeter equation . . . . .	32
1.8.2	Optical spectrum within the BSE . . . . .	35
1.9	Computational details . . . . .	35
<b>2</b>	<b>The <math>F</math> center in LiF</b>	<b>36</b>
2.1	Review of experimental work . . . . .	36
2.2	Review of theoretical work . . . . .	36
2.3	Modeling the $F$ center . . . . .	37
2.4	Pristine LiF . . . . .	38
2.5	$F$ -center relaxations and formation energies . . . . .	43
2.6	Electronic (band) structure of the $F$ -center . . . . .	45
2.7	Absorption spectra of the $F$ -center . . . . .	51
2.8	Summary and conclusions . . . . .	57

<b>3</b>	<b>Mollwo-Ivey relation in alkali halides</b>	<b>59</b>
3.1	Review of theoretical work . . . . .	59
3.2	Computational methods . . . . .	60
3.3	Madelung and exchange-correlation potential . . . . .	60
3.4	Square well potential model . . . . .	63
3.5	Ion-size effects . . . . .	66
3.6	Absorption energies in alkali halides . . . . .	71
3.7	Summary and conclusions . . . . .	74
<b>4</b>	<b>Adiabatic connection fluctuation dissipation theorem calculations</b>	<b>75</b>
4.1	Frequency dependency . . . . .	76
4.2	$k$ mesh dependency . . . . .	77
4.3	basis set dependency . . . . .	79
4.4	ACFDT calculations for solids . . . . .	86
4.5	Summary and conclusions . . . . .	91
<b>5</b>	<b>Appendix</b>	<b>92</b>
5.1	Hohenberg Kohn theorems . . . . .	92
5.2	Matrix elements within the LAPW basis . . . . .	93
5.3	Gauss quadrature . . . . .	94
5.4	Quantum chemistry calculations . . . . .	95
5.4.1	Calculated line-width . . . . .	98
5.5	Tutorials for GW, BSE and ACFDT within the WIEN2k package	102
5.5.1	GW calculations . . . . .	102
5.5.2	BSE calculations . . . . .	104
5.5.3	Volume optimization within the ACFDT formalism . .	111

# 1 Introduction

## 1.1 DFT

The basis of this work is the static (non-relativistic) Schrödinger equation within the Born–Oppenheimer approximation

$$\left( -\frac{\hbar^2}{2m} \sum_{i=1}^N \nabla_{\mathbf{x}_i}^2 + \frac{1}{2} \sum_{i \neq j} \frac{e^2}{|\mathbf{x}_i - \mathbf{x}_j|} + \sum_i v_{\text{ext}}(\mathbf{x}_i, \mathbf{R}) + \mathbf{W}(\mathbf{R}) \right) \Psi(\mathbf{x}) = E(\mathbf{R})\Psi(\mathbf{x}) \quad (1)$$

with  $\mathbf{R}$  denoting the ionic coordinates and with  $\mathbf{x} = (\mathbf{r}, \mathbf{s})$  denoting the coordinates and the spin for the electrons, respectively. The first and second term are the kinetic energy and coulomb energy of the electrons. The third term represents the contribution due to the movement of the electrons in an external potential ( $v_{\text{ext}}$ ).  $\mathbf{W}$  describes the energy contribution due to the repulsion of the ionic cores.

Since equation 1 relies on  $4N$  coordinates for the electrons, it is more or less computationally intractable to solve this equation for more than very few electrons. Hohenberg and Kohn [1] (see Hohenberg–Kohn theorem in appendix 5.1) showed that the ground state of an  $N$  electron system can be uniquely described (up to an additive constant) by the electron density

$$\rho(\mathbf{r}) = N \int d^3r_2 \dots d^3r_N \Psi^*(\mathbf{r}, \mathbf{r}_2, \dots, \mathbf{r}_N) \Psi(\mathbf{r}, \mathbf{r}_2, \dots, \mathbf{r}_N) = \langle \Psi | \hat{\rho}(\mathbf{r}) | \Psi \rangle \quad (2)$$

or

$$\rho(\mathbf{r}) = \langle \Psi | \hat{\rho}(\mathbf{r}) | \Psi \rangle. \quad (3)$$

With this knowledge the many-body problem with  $4N$  variables is mapped to 4 variables and the electronic ground state total energy is written as follows:

$$E_{HK}[\rho] = F[\rho] + \int d^3\mathbf{r} \rho(\mathbf{r}) v(\mathbf{r}) \quad F[\rho] = \min \langle \psi | \hat{T} + \hat{V}_{ee} | \psi \rangle. \quad (4)$$

Here  $\hat{T}$  describes the kinetic energy and  $\hat{V}_{ee}$  the potential energy due to the electron–electron repulsion of the many-electron system.  $F[\rho]$  is a unique functional of  $\rho$  but there is no concrete expression available for it. In the late 1920’s and early 1930’s Thomas and Fermi [2, 3] suggested an approximation for  $F[\rho]$  which utilizes the electron density of the homogeneous electron gas for the kinetic energy, but they failed to describe bonding in atoms or solids. In 1965 Kohn and Sham [4] suggested a different approach to describe  $F[\rho]$

and hence the total energy:

$$E[\rho(\mathbf{r})] = T_s[\rho(\mathbf{r})] + \int d^3r \rho(\mathbf{r}) \left( \frac{1}{2} v_H + v_{xc}[\rho(\mathbf{r})] + v_{ext}[\rho(\mathbf{r})] \right). \quad (5)$$

The idea in this ansatz is to replace the term for the kinetic energy of the electrons of the interacting many-body system by the kinetic energy of independent electrons  $T_s$  moving in an external potential  $v_{ext}[\rho(\mathbf{r})]$  and to put all remaining many body effects, beyond the coulomb potential of the electrons (Hartree potential)

$$v_H[\rho(\mathbf{r})] = e^2 \int d^3r' \frac{\rho(\mathbf{r}')}{|\mathbf{r} - \mathbf{r}'|} \quad (6)$$

and the external potential, into an exchange and correlation term  $v_{xc}$ . In other words the many electron system with density  $\rho$  is mapped to a single electron system moving in an effective potential which describes the influence of the other electrons at the same density  $\rho$ . The exact ground state energy is obtained by minimizing equation 5 with respect to  $\rho(\mathbf{r})$  leading to the famous Kohn–Sham equations

$$\left( -\frac{\hbar^2}{2m} \nabla^2 + v_{eff}[\rho(\mathbf{r})] \right) \psi_n = \varepsilon_n \psi_n \quad (7)$$

where

$$v_{eff}[\rho(\mathbf{r})] = (v_H[\rho(\mathbf{r})] + v_{xc}[\rho(\mathbf{r})] + v_{ext}[\rho(\mathbf{r})]) \quad (8)$$

is the effective potential. The exchange-correlation potential is defined as

$$v_{xc}(\mathbf{r}) = \frac{\delta E_{xc}[\rho]}{\delta \rho(\mathbf{r})}. \quad (9)$$

The Kohn–Sham formulation is in principle an exact formulation for the ground state electron density and total energy, but there is no concrete expression for the exchange-correlation energy  $E_{xc}$ .

## 1.2 Basis functions

Throughout this work we are representing the (macroscopic) samples with a unit cell and a lattice with periodic boundary conditions which obviously is a good approximation for solids. This means that the unit cell of the crystal is repeated "quasi infinitely" in all 3 directions of space and the wave functions can be described as Bloch functions:

$$\psi_{n\mathbf{k}}(\mathbf{r}) = u_{n\mathbf{k}}(\mathbf{r}) e^{i\mathbf{k}\mathbf{r}}. \quad (10)$$

where  $u_{n\mathbf{k}}$  describes the cell periodic part of the wave function with phase factor  $e^{i\mathbf{k}\mathbf{r}}$ . The Kohn–Sham wave functions  $\psi_{n\mathbf{k}}$  are expanded into a linear combination of some basis functions  $\phi_{\mathbf{K}}^{\mathbf{k}}$ . There are a lot of possible choices for the basis functions as e.g. Gaussian-like functions. An intuitive choice for the basis functions  $\phi_{\mathbf{K}}^{\mathbf{k}}$  are plane waves  $e^{i(\mathbf{k}+\mathbf{K})\mathbf{r}}$  leading to the following expression for  $u_{n\mathbf{k}}$

$$u_{n\mathbf{k}}(\mathbf{r}) = \sum_{\mathbf{K}} c_{n\mathbf{k}}(\mathbf{K}) e^{i\mathbf{K}\mathbf{r}}. \quad (11)$$

and for the wave functions

$$\psi_{n\mathbf{k}} = \sum_{\mathbf{K}} c_{n\mathbf{k}}(\mathbf{K}) \phi_{\mathbf{K}}^{\mathbf{k}} \quad (12)$$

where the wave vector  $\mathbf{k}$  lies in the first Brillouin zone of the reciprocal lattice and the sum runs over reciprocal lattice vectors  $\mathbf{K}$ . The variational coefficients  $c_{n\mathbf{k}}(\mathbf{K})$  are determined by the Rayleigh–Ritz variational principle for each  $\mathbf{k}$  point separately. The total energy is then calculated as an integral over  $\mathbf{k}$  (e.g. by the tetrahedron method [5]).

Since we need an extraordinary large number of plane waves in equation 11 for the description of wave functions showing strong oscillations such as electrons close to the nuclear cores, the description of the wave functions only by plane waves is computationally intractable.

One solution to circumvent this problem is to include only valence electrons within the Kohn–Sham equations and to describe the nuclear region within the pseudopotential (PP) [6, 7] or projector augmented-wave method (PAW) [8, 9]. We are not going to further discuss these methods in this work.

### 1.2.1 APW method

Another way to circumvent the problem of the strong oscillations of the electrons in the vicinity of the nuclei is by the augmented plane wave (APW) method. The fundamental idea of this method is to replace the wave function around atom  $\alpha$  within a given radius  $R_{MT,\alpha}$  (we call it muffin tin radius since it resembles a muffin tin when looked at it perpendicularly from the top) around each atom by atomic like wave functions and to keep the plane waves in the interstitial. This ansatz was originally proposed by Slater [10] in 1937 and has gone through a lot of development since. The basis set in this method is defined as follows:

$$\phi_{\mathbf{K}}^{\mathbf{k}}(\mathbf{r}) = \begin{cases} \frac{1}{\sqrt{\Omega}} e^{i(\mathbf{k}+\mathbf{K})\mathbf{r}} & \mathbf{r} \in I \\ \sum_{\alpha,l,m} A_{lm}^{\alpha,\mathbf{k}+\mathbf{K}} u_l^{\alpha}(\mathbf{r}, E) Y_m^l(\hat{\mathbf{r}}) & \mathbf{r} \in R_{MT,\alpha} \end{cases} \quad (13)$$

where  $\Omega$  is the volume of the unit cell. It should be noted that the coordinates of  $\mathbf{r}$  are given with respect to the atomic centers  $\mathbf{R}_\alpha$ .  $Y_m^l(\hat{\mathbf{r}})$  are spherical harmonics.  $u_l^\alpha(\mathbf{r}, E)$  are solutions of the radial Schrödinger equations for atom  $\alpha$  at the eigenenergy  $E$ .  $A_{lm}^{\alpha, \mathbf{k}+\mathbf{K}}$  is a coefficient that matches the interstitial plane wave at the sphere boundary to the atomic wave functions. It is determined by expanding a plane wave in a Rayleigh expansion with spherical harmonics and Bessel functions of order  $l$   $j_l$  around the center of atom  $\alpha$

$$\frac{1}{\sqrt{\Omega}} e^{i(\mathbf{k}+\mathbf{K})\mathbf{r}} = \frac{4\pi}{\sqrt{\Omega}} e^{i(\mathbf{k}+\mathbf{K})\mathbf{R}_\alpha} \sum_{l,m} i^l j_l(|\mathbf{r}-\mathbf{R}_\alpha||\mathbf{k}+\mathbf{K}|) Y_m^{l,*}(\widehat{\mathbf{k}+\mathbf{K}}) Y_m^l(\widehat{\mathbf{r}-\mathbf{R}_\alpha}) \quad (14)$$

and requiring that  $\mathbf{r}=\mathbf{R}_{MT,\alpha}$  which leads to the final expression for the expansion coefficients

$$A_{lm}^{\alpha, \mathbf{k}+\mathbf{K}} = \frac{4\pi i^l e^{i(\mathbf{k}+\mathbf{K})\mathbf{r}}}{\sqrt{\Omega} u_l^\alpha(\mathbf{R}_{MT,\alpha}, E_l)} j_l(\mathbf{R}_{MT,\alpha}|\mathbf{k}+\mathbf{K}|) Y_m^{l,*}(\widehat{\mathbf{k}+\mathbf{K}}). \quad (15)$$

### 1.2.2 LAPW method

The problem with the basis function around each atom as defined in equation 13 is that the eigenenergies  $E$  in  $u_l^\alpha(\mathbf{r}, E)$  are a priori unknown and have to be determined by finding the roots of the secular equations  $|H - ES|$  which is a very demanding task. One solution to this is to linearize the energy dependence by making a first-order Taylor expansion for  $u_l$  around the trial energy  $E_t$ :

$$u_l^\alpha(\mathbf{r}, E) = u_l^\alpha(\mathbf{r}, E_t) + (E - E_t) \dot{u}_l^\alpha(\mathbf{r}, E_t) + O(E - E_t)^2. \quad (16)$$

When we also consider the energy derivative of the solution of the radial Schrödinger equation  $\dot{u}_l$  in equation 13 we arrive at the linearized augmented plane wave method [11–13] (LAPW) which is defined as follows:

$$\phi_{\mathbf{K}}^{\mathbf{k}}(\mathbf{r}) = \begin{cases} \frac{1}{\sqrt{\Omega}} e^{i(\mathbf{k}+\mathbf{K})\mathbf{r}} & \mathbf{r} \in I \\ \sum_{\alpha, l, m} \left( A_{lm}^{\alpha, \mathbf{k}+\mathbf{K}} u_l^\alpha(\mathbf{r}, E_l) + B_{lm}^{\alpha, \mathbf{k}+\mathbf{K}} \dot{u}_l^\alpha(\mathbf{r}, E_l) \right) Y_m^l(\hat{\mathbf{r}}) & \mathbf{r} \in R_{MT,\alpha} \end{cases}. \quad (17)$$

The matching coefficients  $B_{lm}$  for the  $\dot{u}_l^\alpha$ 's are similarly obtained as the  $A_{lm}$ 's by requiring that not only the wave function but also the first derivative of the plane waves match the atomic like wave function at the sphere boundary.

### 1.2.3 APW+lo method

The drawback of LAPW compared to APW is that by replacing  $u_l$  by  $u_l + \dot{u}_l$  a new matching coefficient  $B_{lm}$  is introduced which unfortunately increases the required basis set size (number of plane waves needed to reach a certain convergence) compared to the one in APW [14]. To deal with this problem we keep the APW basis and augment it with local orbitals (lo) which ensure the variational flexibility of the radial part of the basis functions. So the APW+lo consists of two parts, the usual APW basis, but at fixed energy  $E_l$

$$\phi_{\mathbf{K}}^{\mathbf{k}}(\mathbf{r}) = \begin{cases} \frac{1}{\sqrt{\Omega}} e^{i(\mathbf{k}+\mathbf{K})\mathbf{r}} & \mathbf{r} \in I \\ \sum_{l,m} A_{lm}^{\alpha,\mathbf{k}+\mathbf{K}} u_l^\alpha(\mathbf{r}, E_l) Y_m^l(\hat{\mathbf{r}}) & \mathbf{r} \in R_{MT,\alpha} \end{cases} \quad (18)$$

and lo's

$$\phi_{\alpha,lo}^{lm}(\mathbf{r}) = \begin{cases} 0 & \mathbf{r} \in I \\ \left( A_{lm}^{\alpha,lo} u_l^\alpha(\mathbf{r}, E_l) + B_{lm}^{\alpha,lo} \dot{u}_l^\alpha(\mathbf{r}, E_l) \right) Y_m^l(\hat{\mathbf{r}}) & \mathbf{r} \in R_{MT,\alpha} \end{cases} \quad (19)$$

These additional basis functions look very similar to the ones by APW but they don't depend on  $\mathbf{k}$  and their coefficients  $A_{lm}^{\alpha,lo}$  and  $B_{lm}^{\alpha,lo}$  are determined by the requirement that the lo's are matching to zero at the sphere boundary (plus normalization). The APW+lo basis is similar in size to the APW basis since we are adding only a few lo's to the APW basis.

### 1.2.4 LAPW+LO and APW+lo+LO method

One drawback of the LAPW and APW+lo method is that for a given quantum number  $l$  only one state near the energy  $E_l$  can be described. The problem is that  $u_l^\alpha(\mathbf{r}, E_l)$  is only valid in a small region around  $E_l$  and different states with the same  $l$  but different principal quantum number, such as e.g. semi-core states or conduction bands, are described wrong. To remedy this additional local orbitals [15] (LO's) are added to the basis (LAPW or APW+lo)

$$\phi_{\alpha,n,LO}^{lm}(\mathbf{r}) = \begin{cases} 0 & \mathbf{r} \in I \\ \left( A_{lm}^{\alpha,n,LO} u_l^\alpha(\mathbf{r}, E_l) + B_{lm}^{\alpha,n,LO} \dot{u}_l^\alpha(\mathbf{r}, E_l) + X_{lm}^{\alpha,n,LO} u_l^\alpha(\mathbf{r}, E_{l,n}^{LO}) \right) Y_m^l(\hat{\mathbf{r}}) & \mathbf{r} \in R_{MT,\alpha} \end{cases} \quad (20)$$

Inside the muffin-tin spheres for a given  $l$  the solutions of the radial functions  $u_l^\alpha(\mathbf{r}, E_{l,n}^{LO})$  are added to the basis for the desired principal quantum numbers  $n$  at energies  $E_{l,n}^{LO}$  with coefficient  $X_{lm}^{\alpha,n,LO}$ . The coefficients  $A_{lm}^{\alpha,n,LO}$ ,  $B_{lm}^{\alpha,n,LO}$  and  $X_{lm}^{\alpha,n,LO}$  are determined so that  $\phi_{\alpha,n,LO}^{lm}(\mathbf{r})$  (and the first derivative) vanishes at the sphere boundary.

### 1.3 XC functionals

An exact expression for the exchange-correlation energy  $E_{xc}$  or the exchange-correlation potential  $v_{xc}$  in equation 8 is not known. The earliest approximation for  $E_{xc}$  is the so called local density approximation (LDA) [3, 16]. This approach assumes that at a given electron density  $v_{xc}[\rho]$  can be replaced by the exchange-correlation energy of the homogeneous electron gas  $e_{xc}^{hom}[\rho]$  and the exchange-correlation energy is written as follows

$$E_{xc}^{LDA}[\rho(\mathbf{r})] = \int d^3r \rho(\mathbf{r}) e_{xc}^{hom} |\rho|. \quad (21)$$

Since the exchange-correlation functional in the LDA is replaced only locally at a given density, one should expect that this approach is only valid for systems with slowly varying density. Nevertheless the LDA works for a very large number of solids. An improvement to the LDA is achieved within the generalized gradient approximation (GGA) by not only considering the electron density but also the gradient of the electron density  $\nabla\rho(\mathbf{r})$  in the exchange-correlation functional

$$E_{xc}^{GGA}[\rho(\mathbf{r})] = \int d^3r f(\rho, \nabla\rho). \quad (22)$$

We will use the GGA parametrization by Perdew, Burke and Ernzerhof [17] (PBE), which is the most widely used GGA, throughout this work. PBE and LDA, or other semi-local functionals (SL), have been (and still are) the working horses for decades but nevertheless they have major shortcomings in the computation of solids, e.g. too small band gaps in semiconductors and insulators [18–20], inaccurate lattice constants etc. In the following subsection we will introduce two examples as improvements over SL functionals. Both methods modify the form of the exchange potential either by including the kinetic energy density (meta-GGA) as in section 1.3.1 or by replacing fractions of the SL exchange by (non local) exact exchange (hybrid functional) described in section 1.3.3.



### 1.3.1 TB-mBJ

The optimized effective potential [21,22] (OEP) method applied to the exact exchange functional is considered as giving improved band gaps over LDA in atoms and molecules. Since this method is computationally very expensive Becke and Johnson [23] proposed a simple approximation which leads to similar results as OEP in atoms. The Becke–Johnson (BJ) exchange potential is written as follows

$$V_{x,\sigma}(\mathbf{r}) = V_{x,\sigma}^{\text{Slater}}(\mathbf{r}) + \frac{1}{\pi} \sqrt{\frac{5}{12}} \sqrt{\frac{2\tau_{\sigma}(\mathbf{r})}{\rho_{\sigma}(\mathbf{r})}} \quad (23)$$

where  $\sigma$  denotes the spin for spin polarized systems.  $V_{x,\sigma}^{\text{Slater}}$  is the Slater [24, 25] potential and  $\tau$  is the kinetic energy density

$$\tau_{\sigma} = \frac{1}{2} \sum_i |\nabla \psi_{i\sigma}|^2. \quad (24)$$

This potential reproduces OEP potentials for atoms and molecules but gives little improvement over LDA or PBE for the band gap in solids in many cases.

Tran and Blaha [26] proposed a modification of the Becke–Johnson exchange potential which yields accurate band gaps for a wide range of solids. The Tran–Blaha modified Becke–Johnson (TB-mBJ) potential is written as follows

$$v_{x,\sigma}^{\text{TB-mBJ}}(\mathbf{r}) = cv_{x,\sigma}^{\text{BR}}(\mathbf{r}) + (3c - 2) \frac{1}{\pi} \sqrt{\frac{5}{12}} \sqrt{\frac{2\tau_{\sigma}(\mathbf{r})}{\rho_{\sigma}(\mathbf{r})}}. \quad (25)$$

$v_{x,\sigma}^{\text{BR}}$  denotes the Becke–Russel [27] potential which models the Coulomb potential generated by the exchange hole. The original BJ used the Slater potential instead of the Becke–Russel potential but it was shown that these potentials are very similar for atoms [23]. The crucial part of TB-mBJ is the coefficient  $c$ , which is obtained from

$$c = \alpha + \beta \left( \frac{1}{\Omega} \int_{\Omega} \frac{|\nabla \rho(\mathbf{r})|}{\rho(\mathbf{r})} d^3r \right)^{1/2} \quad (26)$$

where  $\Omega$  is the unit cell volume.  $\alpha$  and  $\beta$  are free parameters which are obtained by minimization of the mean absolute relative error of the band gaps for a given set of solids. We will mainly use the parametrization of Koller et al. [28] throughout this work which is especially parametrized to give good results for wide-gap insulators and semi-conductors. Equation 25 is chosen such that the LDA exchange potential is obtained for a constant density and that for  $c = 1$  the original Becke–Johnson exchange potential is recovered.

### 1.3.2 Hartree–Fock based methods

The Hartree–Fock [29,30] (HF) equation for a many-body system in the DFT formalism is given as

$$\left(-\frac{\hbar^2}{2m}\nabla^2 + \hat{v}_{HF}(\mathbf{r})\right)\psi_n = \varepsilon_n\psi_n \quad (27)$$

where the one-electron HF operator is defined as follows

$$\hat{v}_{HF}(\mathbf{r}) = v_{\text{ext}}(\mathbf{r}) + \int d^3r' \frac{e^2}{|\mathbf{r} - \mathbf{r}'|} \rho(\mathbf{r}') - \int d^3r' \rho_1(\mathbf{r}', \mathbf{r}) \frac{e^2}{|\mathbf{r} - \mathbf{r}'|}. \quad (28)$$

The second and third term in equation 28 are the Coulomb and exchange term, respectively. The exchange term uses the two-electron density which is given as

$$\rho_1(\mathbf{r}', \mathbf{r}) = \sum_{i=1}^N \psi_i^*(\mathbf{r}')\psi_i(\mathbf{r}). \quad (29)$$

The biggest limitation of the HF approximation is that it does not include any correlation. Thus one way to remedy this problem is to start from a HF calculation and then correct for correlation, such as in e.g. Moller-Plesset perturbation theory [31] (MP $n$ , where  $n$  is the order of the correction), multi-configurational self-consistent field [32] (MCSCF) method, configuration interaction [33] (CI) method and coupled cluster [34] (CC) theory. We will not discuss these methods here. The interested reader can find detailed descriptions of these methods in references [35,36].

### 1.3.3 Screened hybrid functionals

The Hartree–Fock exchange energy can be split into three contributions:

$$E_x^{\text{HF}} = E_{x,vv}^{\text{HF}} + E_{x,vc}^{\text{HF}} + E_{x,cc}^{\text{HF}} \quad (30)$$

where  $E_{x,vv}^{\text{HF}}$ ,  $E_{x,vc}^{\text{HF}}$  and  $E_{x,cc}^{\text{HF}}$  describe the valence-valence, valence-core and core-core contributions, respectively. These three contributions are written as follows

$$E_{x,vv}^{\text{HF}} = -\frac{1}{2} \sum_{\sigma} \sum_{n\mathbf{k}, n'\mathbf{k}'} w_{n\mathbf{k}}^{\sigma} w_{n'\mathbf{k}'}^{\sigma} \int_{\Omega} \int_{\Omega} \psi_{n\mathbf{k}}^{\sigma*}(\mathbf{r}) \psi_{n'\mathbf{k}'}^{\sigma}(\mathbf{r}) \times v(|\mathbf{r} - \mathbf{r}'|) \psi_{n'\mathbf{k}'}^{\sigma*}(\mathbf{r}') \psi_{n\mathbf{k}}^{\sigma}(\mathbf{r}') d^3r' d^3r \quad (31)$$

$$E_{x,vc}^{\text{HF}} = - \sum_{\sigma} \sum_{\alpha}^{\text{UC}} \sum_{n_c l_c m_c} \sum_{n\mathbf{k}} w_{n\mathbf{k}}^{\sigma} \int_{S_{\alpha}} \int_{S_{\alpha}} \psi_{n\mathbf{k}}^{\sigma*}(\mathbf{r}) \psi_{n_c l_c m_c}^{\alpha\sigma}(\mathbf{r}) \times v(|\mathbf{r} - \mathbf{r}'|) \psi_{n_c l_c m_c}^{\alpha\sigma*}(\mathbf{r}') \psi_{n\mathbf{k}}^{\sigma}(\mathbf{r}') d^3r' d^3r \quad (32)$$

$$\begin{aligned}
E_{x,cc}^{\text{HF}} = & -\frac{1}{2} \sum_{\sigma} \sum_{\alpha}^{\text{UC}} \sum_{n_c l_c m_c} \sum_{n'_c l'_c m'_c} \int_{S_{\alpha}} \int_{S_{\alpha}} \psi_{n'_c l'_c m'_c}^{\alpha\sigma*}(\mathbf{r}) \psi_{n_c l_c m_c}^{\alpha\sigma*}(\mathbf{r}) \\
& \times v(|\mathbf{r} - \mathbf{r}'|) \psi_{n_c l_c m_c}^{\alpha\sigma*}(\mathbf{r}') \psi_{n'_c l'_c m'_c}^{\alpha\sigma*}(\mathbf{r}') d^3 r' d^3 r.
\end{aligned} \tag{33}$$

In these equations  $\sigma$  represents the spin,  $\Omega$  the crystal volume and  $\alpha$  runs over all atoms in the whole unit cell (UC) with corresponding atomic sphere radius  $S_{\alpha}$ .  $w_{n\mathbf{k}}^{\sigma}$  is the product of the  $k$  point weight and the occupation number of state  $n$ .  $v$  represents usually the unscreened coulomb potential

$$v = \frac{1}{|\mathbf{r} - \mathbf{r}'|}. \tag{34}$$

Since in solids the  $k$  point convergence of the long range (LR) part of the exchange energy can be quite slowly, screened potentials can be used instead of the bare coulomb potential to assure faster convergence with the same accuracy. One example for a screened potential is the Yukawa [37] screened potential

$$v = \frac{e^{-\lambda|\mathbf{r}-\mathbf{r}'|}}{|\mathbf{r} - \mathbf{r}'|} \tag{35}$$

where  $\lambda$  is a screening parameter.

The fundamental idea of screened hybrid methods is that a certain fraction  $\alpha$  of the short-range (SR) SL exchange energy  $E_x^{\text{SL}}$  is replaced by (non-local) Hartree–Fock (HF) exchange energy  $E_x^{\text{HF}}$ , but the correlation is kept purely SL:

$$E_{xc}^{\text{SL}} = E_{xc}^{\text{SL}} + \alpha(E_x^{\text{SR-HF}} - E_x^{\text{SR-SL}}). \tag{36}$$

The success of this method is more or less ascribed to an error cancellation of HF and the underlying SL exchange. For example the band gap is in many cases on one hand underestimated by SL functionals, which is known as the band gap problem, and on the other hand overestimated by HF, but a certain combination of both methods can give good agreement with experiment. The most commonly used screened hybrid functional for solids is the HSE [38–40] functional which uses the error function for the long-range screening and  $\alpha = 0.25$  of unscreened  $v$  (also known as PBE0 [41, 42]). In the remainder of this work we are going to use the Yukawa screened potential instead of the error function but with the same  $\alpha$  as PBE0 and hence denote this method as YS-PBE0.

## 1.4 Linear response theory

### 1.4.1 Linear response function

The response function [43]  $\chi(\mathbf{r}, \mathbf{r}', t - t')$  describes the change of the density  $\delta\rho(\mathbf{r}, t)$  of an  $N$  electron system with respect to the change of the external potential  $\delta v_{\text{ext}}(\mathbf{r}', t')$  due to a small external perturbation (e.g. light)

$$\chi(\mathbf{r}, \mathbf{r}', t - t') = \frac{\delta\rho(\mathbf{r}, t)}{\delta v_{\text{ext}}(\mathbf{r}', t')}. \quad (37)$$

By requiring that the change in the density is the same the response function in the Kohn-Sham formalism is written in a similar way

$$\chi^{\text{KS}}(\mathbf{r}, \mathbf{r}', t - t') = \frac{\delta\rho(\mathbf{r}, t)}{\delta v_{\text{eff}}(\mathbf{r}', t')}. \quad (38)$$

where  $v_{\text{eff}}$  describes the effective potential as described in equation 8. Combining this two equations and going to frequency space leads to a relation for the response function which has the form of the Dyson equation [44]

$$\begin{aligned} \chi(\mathbf{r}, \mathbf{r}', \omega) &= \chi^{\text{KS}}(\mathbf{r}, \mathbf{r}', \omega) + \int d^3r_1 d^3r_2 \chi^{\text{KS}}(\mathbf{r}, \mathbf{r}_1, \omega) \\ &\times \left( \frac{e^2}{|\mathbf{r}_1 - \mathbf{r}_2|} + f_{\text{xc}}(\mathbf{r}_1, \mathbf{r}_2, \omega) \right) \chi(\mathbf{r}_2, \mathbf{r}', \omega) \end{aligned} \quad (39)$$

where  $f_{\text{xc}}$  is the exchange-correlation kernel which is defined in real time-space as the derivative of the time-dependent exchange-correlation potential with respect to the time-dependent density. The most common approximation for  $f_{\text{xc}}$  is the random phase approximation [45–47] (RPA) with  $f_{\text{xc}} = 0$ . An explicit expression for the Kohn–Sham response function derived by Adler and Wiser [48, 49] or alternatively by Pines and Nozieres [50] is given as follows

$$\begin{aligned} \chi^{\text{KS}}(\mathbf{r}, \mathbf{r}', \omega) &= - \sum_n \sum_m 2f_n(1 - f_m) \\ &\times \left( \frac{\psi_m^*(\mathbf{r}')\psi_n(\mathbf{r}')\psi_n^*(\mathbf{r})\psi_m(\mathbf{r})}{\varepsilon_m - \varepsilon_n - \omega - i\eta} + \frac{\psi_n^*(\mathbf{r}')\psi_m(\mathbf{r}')\psi_m^*(\mathbf{r})\psi_n(\mathbf{r})}{\varepsilon_m - \varepsilon_n + \omega + i\eta} \right) \end{aligned} \quad (40)$$

where  $n$  and  $m$  run over all bands and  $f_n$  and  $f_m$  are 1 and 0 for occupied and unoccupied states. Since Equation 40 is invariant in real space due to a shift by a lattice vector  $\chi(\mathbf{r}, \mathbf{r}', \omega) = \chi(\mathbf{r} + \mathbf{R}, \mathbf{r}' + \mathbf{R}, \omega)$ , the response function in reciprocal space  $\chi(\mathbf{q}, \mathbf{q}', \omega)$  is only non zero when  $\mathbf{q}$  and  $\mathbf{q}'$  differ by a reciprocal lattice vector  $G$ . Using Bloch’s theorem the reciprocal space

indices  $(\mathbf{q}, \mathbf{q}')$  are reduced to  $\mathbf{q}$  and a sum over all  $\mathbf{k}$  points, where both are lying in the first Brillouin zone. The Kohn-Sham response function in reciprocal space is then expressed as

$$\chi_{\mathbf{G}, \mathbf{G}'}^{\text{KS}}(\mathbf{q}, \omega) = -\frac{1}{\Omega} \sum_{nm\mathbf{k}} 2(f_{m\mathbf{k}+\mathbf{q}} - f_{n\mathbf{k}}) \frac{M_{m,n}^{\mathbf{G}}(\mathbf{k}, \mathbf{q}) M_{n,m}^{\mathbf{G}'}(\mathbf{k}, \mathbf{q})}{\varepsilon_{m\mathbf{k}+\mathbf{q}} - \varepsilon_{n\mathbf{k}} - \omega - i\eta} \quad (41)$$

where the matrix elements

$$M_{m,n}^{\mathbf{G}}(\mathbf{k}, \mathbf{q}) = \langle \psi_{m\mathbf{k}+\mathbf{q}} | e^{i(\mathbf{q}+\mathbf{G})\mathbf{r}} | \psi_{n\mathbf{k}} \rangle = \int_{\Omega} d^3r \psi_{m\mathbf{k}+\mathbf{q}}^*(\mathbf{r}) e^{i(\mathbf{q}+\mathbf{G})\mathbf{r}} \psi_{n\mathbf{k}}(\mathbf{r}) \quad (42)$$

and

$$M_{n,m}^{\mathbf{G}'}(\mathbf{k}, \mathbf{q}) = \langle \psi_{n\mathbf{k}} | e^{-i(\mathbf{q}+\mathbf{G}')\mathbf{r}'} | \psi_{m\mathbf{k}+\mathbf{q}} \rangle = \int_{\Omega} d^3r \psi_{n\mathbf{k}}^*(\mathbf{r}) e^{-i(\mathbf{q}+\mathbf{G}')\mathbf{r}} \psi_{m\mathbf{k}+\mathbf{q}}(\mathbf{r}) \quad (43)$$

are integrated over the whole unit cell with volume  $\Omega$ . The expressions for the matrix elements within the LAPW method are given in appendix 5.2.

### 1.4.2 Dielectric function

A general description of the electric field  $E$  inside a material with respect to an external field  $E_{\text{ext}}$  is given as

$$E = \epsilon^{-1} E_{\text{ext}} \quad (44)$$

where  $\epsilon$  is the dielectric function.

The dielectric function is defined both on the microscopic and macroscopic level and the corresponding equations are given as follows

$$e(\mathbf{r}, \omega) = \int d^3r' \epsilon_{\text{mic}}^{-1}(\mathbf{r}, \mathbf{r}', \omega) E_{\text{ext}}(\mathbf{r}', \omega) \quad (45)$$

$$E(\mathbf{r}, \omega) = \int d^3r' \epsilon_{\text{mac}}^{-1}(\mathbf{r} - \mathbf{r}', \omega) E_{\text{ext}}(\mathbf{r}', \omega) \quad (46)$$

The microscopic total electric field  $e(\mathbf{r}, \omega)$  shows large oscillations and the microscopic dielectric function  $\epsilon_{\text{mic}}^{-1}(\mathbf{r}, \mathbf{r}', \omega)$  depends on  $\mathbf{r}$  and  $\mathbf{r}'$  explicitly. For the total macroscopic function these large oscillations are more or less averaged out and the macroscopic dielectric function  $\epsilon_{\text{mac}}^{-1}(\mathbf{r} - \mathbf{r}', \omega)$  depends only on the difference of  $\mathbf{r}$  and  $\mathbf{r}'$ . Analogously to reference [51] we will derive a connection between the microscopic and macroscopic quantities.

The macroscopic and microscopic total electric fields are coupled by

$$E(\mathbf{R}, \omega) = \frac{1}{\Omega} \int_{\Omega} d^3r e(\mathbf{r}, \omega) \quad (47)$$

where the integration is carried out over the unit cell with volume  $\Omega$ . We note that  $E_{\mathbf{R},\omega}$  depends on the lattice vector  $R$ . By Fourier transforming the right hand side of equation 47 we arrive to the following equation

$$E(\mathbf{R}, \omega) = \sum_{\mathbf{G}} \int_{\text{BZ}} \frac{d^3\mathbf{q}}{(2\pi)^3} e(\mathbf{q} + \mathbf{G}, \omega) \frac{1}{\Omega} \int_{\Omega} d^3r e^{i(\mathbf{q} + \mathbf{G})\mathbf{r}} \quad (48)$$

where the first integration is carried out in the first Brillouin zone. Since we are mainly interested in external fields with a wavelength much larger than the atomic distances (e.g. visible light),  $\mathbf{q} \ll \mathbf{G}$  and  $e^{i\mathbf{q}\mathbf{r}}$  can be moved in front of the integral over the unit cell volume. The sum and the integration over  $\mathbf{G}$  is then averaged out and equation 48 can be approximated as

$$E(\mathbf{R}, \omega) = \sum_{\mathbf{G}} \int_{\text{BZ}} \frac{d^3\mathbf{q}}{(2\pi)^3} e(\mathbf{q} + \mathbf{G}, \omega) \frac{1}{\Omega} e^{i\mathbf{q}\mathbf{r}} \int_{\Omega} d^3r e^{i\mathbf{G}\mathbf{r}} = \int_{\text{BZ}} \frac{d^3\mathbf{q}}{(2\pi)^3} e^{i\mathbf{q}\mathbf{r}} e(\mathbf{q}, \omega). \quad (49)$$

The Fourier transform of  $E(\mathbf{R}, \omega)$  is given as follows

$$E(\mathbf{R}, \omega) = \sum_{\mathbf{G}} \int_{\text{BZ}} \frac{d^3\mathbf{q}}{(2\pi)^3} e^{i(\mathbf{q} + \mathbf{G})\mathbf{r}} E(\mathbf{q}, \omega). \quad (50)$$

This looks very similar to equation 49 and by comparing the two equations the following relationship is established between the macroscopic and microscopic total electric field

$$E(\mathbf{q} + \mathbf{G}, \omega) = e(\mathbf{q}, \omega) \delta_{\mathbf{G},0}. \quad (51)$$

Since

$$E(\mathbf{q}, \omega) = \epsilon_{\text{mac}}^{-1}(\mathbf{q}, \omega) E_{\text{ext}}(\mathbf{q}, \omega) \quad (52)$$

the following relationship is given for  $\mathbf{G} = 0$

$$E(\mathbf{q}, \omega) = e(\mathbf{q}, \omega) = \sum_{\mathbf{G}'} \epsilon_{\text{mic},0\mathbf{G}'}^{-1}(\mathbf{q}, \omega) \delta_{\mathbf{G}',0} E_{\text{ext}}(\mathbf{q}, \omega) = \epsilon_{\text{mic},00}^{-1} E_{\text{ext}}(\mathbf{q}, \omega). \quad (53)$$

By comparing equations 52 and 53 the connection between the macroscopic and microscopic dielectric constant is given as follows

$$\epsilon_{\text{mac}}(\mathbf{q}, \omega) = (\epsilon_{\text{mic},00}^{-1}(\mathbf{q}, \omega))^{-1}. \quad (54)$$

Since the calculation of the inverse of  $\epsilon_{\text{mic},00}$  with respect to  $\mathbf{G}, \mathbf{G}'$  is often very costly, it is common to approximate the macroscopic dielectric function by the head(first element) of the microscopic dielectric function

$$\epsilon_{\text{mac}}(\mathbf{q}, \omega) = \epsilon_{\text{mic},00}(\mathbf{q}, \omega). \quad (55)$$

This assumption is known as "neglect of local fields" (NLF) and is in principle only valid for materials where there are no rapid oscillations due to strongly varying external fields like e.g. for the homogeneous electron gas.

### 1.4.3 Calculation of the dielectric function

For a homogeneous material a longitudinal electric field, which is parallel to the wave vector  $\mathbf{q}$ , induces only a longitudinal response of the system and a transverse electric field induces only a transversal response. For homogeneous materials the response to a longitudinal electric field results in both a transversal and a longitudinal current. The same is valid for a transverse electric field. We are mainly interested in the response of the system to an external transversal wave, e.g. light. In references [52, 53] it has been shown that for  $\mathbf{q} \rightarrow 0$  the transversal and longitudinal dielectric functions become the same. Therefore we will only discuss the longitudinal dielectric function. The longitudinal microscopic dielectric function (see derivation in reference [51]) is given as follows

$$\epsilon_{\text{mic},\mathbf{G}\mathbf{G}'}(\mathbf{q}, \omega) = \delta_{\mathbf{G},\mathbf{G}'} - v_{\mathbf{G},\mathbf{G}'}(\mathbf{q})P_{\mathbf{G},\mathbf{G}'}(\mathbf{q}, \omega) \quad (56)$$

where

$$v_{\mathbf{G},\mathbf{G}'}(\mathbf{q}) = \frac{4\pi e^2}{|\mathbf{q} + \mathbf{G}||\mathbf{q} + \mathbf{G}'|} \quad (57)$$

is the bare Coulomb potential and

$$P_{\mathbf{G},\mathbf{G}'}(\mathbf{q}, \omega) = \frac{\delta\rho(\mathbf{q} + \mathbf{G}, \omega)}{\delta v_{\text{tot}}(\mathbf{q} + \mathbf{G}, \omega)} \quad (58)$$

is the screened response function which describes the response of the density to the total potential. Since there is no exact expression known for  $P_{\mathbf{G},\mathbf{G}'}(\mathbf{q}, \omega)$  the most common approximation is to replace  $P_{\mathbf{G},\mathbf{G}'}(\mathbf{q}, \omega)$  by the Kohn-Sham response function  $\chi_{\mathbf{G},\mathbf{G}'}^{\text{KS}}(\mathbf{q}, \omega)$  as defined in equation 41 which is equivalent to the RPA

$$\epsilon_{\text{mic},\mathbf{G}\mathbf{G}'}^{\text{KS}}(\mathbf{q}, \omega) = \epsilon_{\text{mic},\mathbf{G}\mathbf{G}'}^{\text{RPA}}(\mathbf{q}, \omega) = \delta_{\mathbf{G},\mathbf{G}'} - v_{\mathbf{G},\mathbf{G}'}(\mathbf{q})\chi_{\mathbf{G},\mathbf{G}'}^{\text{KS}}(\mathbf{q}, \omega). \quad (59)$$

The head ( $\mathbf{G}, \mathbf{G}' = 0$ ) and wings ( $\mathbf{G} = 0$ ) of the resulting matrix are singular if  $\mathbf{G} + \mathbf{q} = 0$  and  $\mathbf{G}' + \mathbf{q} = 0$ . The singularities are treated within  $\mathbf{k} \cdot \mathbf{p}$  perturbation theory (see below).

In the case of the macroscopic dielectric function we are interested in the long-wavelength limit which means vanishing  $\mathbf{q}$  in reciprocal space

$$\epsilon_{\text{mac}}^{\text{KS}}(\mathbf{q}, \omega) = \lim_{\mathbf{q} \rightarrow 0} \epsilon_{\text{mic},00}(\mathbf{q}, \omega) = 1 - \frac{4\pi e^2}{\mathbf{q}^2} \chi_{0,0}^{\text{KS}}(\mathbf{q}, \omega). \quad (60)$$

For vanishing  $\mathbf{q}$  and  $\mathbf{G}$ , using  $\mathbf{k} \cdot \mathbf{p}$  perturbation theory, the matrix element  $M_{m,n}^0(\mathbf{k}, \mathbf{q})$  in equation 42 is approximated as

$$M_{m,n}^0(\mathbf{k}, 0) = \delta_{m,n} + (1 - \delta_{m,n}) \frac{\langle \psi_{n\mathbf{k}} | \hat{\mathbf{p}} | \psi_{m\mathbf{k}} \rangle \mathbf{q}}{\epsilon_n(\mathbf{k}) - \epsilon_m(\mathbf{k})}. \quad (61)$$

where  $\hat{\mathbf{p}}$  denotes the momentum operator. The matrix element  $M_{n,m}^0(\mathbf{k}, \mathbf{q})$  is derived analogously. Using the long-wavelength matrix elements in equation 60 finally leads to following expression

$$\epsilon_{\text{mac}}^{\text{KS}}(\mathbf{q} \rightarrow 0, \omega) = 1 - \frac{4\pi e^2}{\Omega} \sum_{nm\mathbf{k}} \frac{\langle \psi_{n\mathbf{k}} | \hat{\mathbf{p}} | \psi_{m\mathbf{k}} \rangle \langle \psi_{m\mathbf{k}} | \hat{\mathbf{p}} | \psi_{n\mathbf{k}} \rangle}{(\epsilon_m(\mathbf{k}) - \epsilon_n(\mathbf{k}) - \omega)(\epsilon_m(\mathbf{k}) - \epsilon_n(\mathbf{k}))^2}. \quad (62)$$

It should be noted that the Coulomb singularity from equation 60 is successfully removed in equation 62. Using the identity

$$\text{Im} \frac{1}{\epsilon_m(\mathbf{k}) - \epsilon_n(\mathbf{k}) - \omega - i\delta} = -i\pi\delta(\epsilon_m(\mathbf{k}) - \epsilon_n(\mathbf{k}) - \omega) \quad (63)$$

the imaginary part of the macroscopic dielectric function  $\text{Im}\epsilon_{\text{mac}}^{\text{KS}}$ , which is directly proportional to the absorption spectrum, is written as follows

$$\text{Im}\epsilon_{\text{mac}}^{\text{KS}}(\mathbf{q} \rightarrow 0, \omega) = \frac{16\pi^2}{\Omega\omega^2} \sum_{nm\mathbf{k}} \langle \psi_{n\mathbf{k}} | \hat{\mathbf{p}} | \psi_{m\mathbf{k}} \rangle \langle \psi_{m\mathbf{k}} | \hat{\mathbf{p}} | \psi_{n\mathbf{k}} \rangle \delta(\epsilon_m(\mathbf{k}) - \epsilon_n(\mathbf{k}) - \omega). \quad (64)$$

The macroscopic dielectric function is a  $3 \times 3$  tensor on account of the momentum matrix elements.

## 1.5 Adiabatic connection fluctuation dissipation theorem

In this chapter we will introduce the adiabatic connection fluctuation dissipation theorem [54–56] (ACDFT), which gives us a method to calculate the correlation energy of a system by the knowledge of the response of the system to an external perturbation. This method relies on two theorems, namely the adiabatic connection theorem and the fluctuation dissipation theorem that are needed for the derivation of the formulas for the correlation energy.

### 1.5.1 Adiabatic connection

We define the many-body Hamiltonian of our interacting system as

$$\hat{H}(\lambda) = \hat{T} + \hat{V}(\lambda) + \lambda\hat{V}_{ee} \quad (65)$$

with

$$\hat{V}_{ee} = \sum_{i<j} \frac{e^2}{|\mathbf{r}_i - \mathbf{r}_j|} \quad (66)$$

where the coupling constant  $\lambda$  allows us to determine the strength of the electron-electron interaction of the many-body system. We restrict ourselves



to systems where the ground state wave-function is non-degenerate and  $\hat{V}(\lambda)$  is determined such that for each  $\lambda$  we get the same ground-state density as for the fully interacting system.

For  $\lambda = 0$  we get the Kohn–Sham system with the Hamiltonian  $\hat{H}(0)$  and wave function  $\psi(0)$

$$E_{\lambda=0} = \langle \psi(0) | \hat{H}(0) | \psi(0) \rangle = \langle \psi(0) | \hat{T} + \hat{V}(0) | \psi(0) \rangle = T_s + E_H + E_{ext} + E_{xc}. \quad (67)$$

For  $\lambda = 1$ ,  $\hat{H}(1)$  is the Hamiltonian of the fully interacting system

$$E_{\lambda=1} = \langle \psi(1) | \hat{H}(1) | \psi(1) \rangle = \langle \psi(1) | \hat{T} + \hat{V}_{ee} | \psi(1) \rangle + E_{ext}. \quad (68)$$

By combining equations 67 and 68 we arrive to the following equation

$$E_{\lambda=1} = E_{\lambda=0} + \int_0^1 \frac{dE_\lambda}{d\lambda} d\lambda. \quad (69)$$

Using the Hellmann–Feynman theorem the integrand of the coupling constant integral is rewritten as

$$\frac{dE_\lambda}{d\lambda} = \langle \psi_\lambda | \frac{\partial \hat{H}(\lambda)}{\partial \lambda} | \psi_\lambda \rangle = \langle \psi_\lambda | \hat{V}_{ee} | \psi_\lambda \rangle \quad (70)$$

and the total energy at full interaction is written as

$$E_{\lambda=1} = E_{\lambda=0} + \int_0^1 \langle \psi_\lambda | \hat{V}_{ee} | \psi_\lambda \rangle d\lambda. \quad (71)$$

This is the adiabatic connection formula which connects the total energy of the Kohn–Sham system to the total energy of the fully interacting system.

### 1.5.2 Fluctuation-dissipation theorem

The fluctuation-dissipation theorem [57] in general states that the response of a system to a small external perturbation is the same as its response to a spontaneous fluctuation. Applying it to DFT, the fluctuation is a fluctuation of the electron density and the perturbation is a small change in the external potential. The response of the system is then described by the linear response function  $\chi$  as introduced in section 1.4.1.

A detailed derivation of the fluctuation-dissipation theorem is given in references [58] and [59]. In the following we will only show how to get an expression for the correlation energy following closely the references above.

The exchange-correlation energy within the fluctuation-dissipation theorem is expressed as

$$E_{xc} = -\frac{e^2}{2} \int_0^1 d\lambda \int d^3r d^3r' \frac{1}{|\mathbf{r} - \mathbf{r}'|} \left( \rho(\mathbf{r})\delta(\mathbf{r} - \mathbf{r}') + \frac{1}{\pi} \int_0^\infty d\omega \chi^\lambda(\mathbf{r}, \mathbf{r}', i\omega) \right) \quad (72)$$

where  $\chi^\lambda$  is the response function at imaginary frequencies  $i\omega$  of a system where the electron-electron interaction is scaled via the coupling constant  $\lambda$  (see chapter 1.5.1). Considering the non-interacting case  $\lambda = 0$  the integration over  $\lambda$  can be omitted and  $\chi^\lambda$  becomes the response function of the Kohn–Sham system  $\chi^\lambda = \chi^{\text{KS}}$

$$E_{xc}^{\text{KS}} = -\frac{e^2}{2} \int d^3r d^3r' \frac{1}{|\mathbf{r} - \mathbf{r}'|} \left( \rho(\mathbf{r})\delta(\mathbf{r} - \mathbf{r}') + \frac{1}{\pi} \int_0^\infty d\omega \chi^{\text{KS}}(\mathbf{r}, \mathbf{r}', i\omega) \right). \quad (73)$$

After explicitly writing the expression for  $\chi^{\text{KS}}(\mathbf{r}, \mathbf{r}', i\omega)$  and after further simplifications the second integrand in equation 73 can be reformulated as

$$\begin{aligned} & -\frac{e^2}{2} \int d^3r d^3r' \frac{1}{|\mathbf{r} - \mathbf{r}'|} \frac{1}{\pi} \int_0^\infty d\omega \chi^{\text{KS}}(\mathbf{r}, \mathbf{r}', i\omega) \\ &= \frac{e^2}{2} \sum_n^{\text{occ}} \sum_m^{\text{empty}} 2 \int d^3r d^3r' \frac{\psi_m^*(\mathbf{r}')\psi_n(\mathbf{r}')\psi_n^*(\mathbf{r})\psi_m(\mathbf{r})}{|\mathbf{r} - \mathbf{r}'|} \int_0^\infty d\omega \frac{2\omega_{nm}}{\omega_{nm}^2 + \omega} \quad (74) \\ &= \frac{e^2}{2} \sum_n^{\text{occ}} \sum_m^{\text{empty}} 2 \int d^3r d^3r' \frac{\psi_m^*(\mathbf{r}')\psi_n(\mathbf{r}')\psi_n^*(\mathbf{r})\psi_m(\mathbf{r})}{|\mathbf{r} - \mathbf{r}'|} \end{aligned}$$

where indices  $n$  and  $m$  run over occupied and empty states, respectively. The first integrand in equation 73 is rewritten as

$$-\frac{e^2}{2} \int d^3r d^3r' \frac{\rho(\mathbf{r})\delta(\mathbf{r} - \mathbf{r}')}{|\mathbf{r} - \mathbf{r}'|} = -\frac{e^2}{2} \sum_n^{\text{occ}} \sum_m^{\text{all}} 2 \int d^3r d^3r' \frac{\psi_m^*(\mathbf{r}')\psi_n(\mathbf{r}')\psi_n^*(\mathbf{r})\psi_m(\mathbf{r})}{|\mathbf{r} - \mathbf{r}'|} \quad (75)$$

where the following relations have been used

$$\delta(\mathbf{r} - \mathbf{r}') = \sum_m^{\text{all}} \psi_m^*(\mathbf{r}')\psi_m(\mathbf{r}) \quad \rho(\mathbf{r}) = \sum_n^{\text{occ}} 2\psi_n^*(\mathbf{r})\psi_n(\mathbf{r}). \quad (76)$$

It should be noted that  $m$  runs over all bands. Inserting equations 74 and 75 into equation 73 leads to an expression for the Kohn–Sham exchange energy

$$E_x^{\text{KS}} = -\frac{e^2}{2} \sum_n^{\text{occ}} \sum_m^{\text{occ}} 2 \int d^3r d^3r' \frac{\psi_m^*(\mathbf{r}') \psi_n(\mathbf{r}') \psi_n^*(\mathbf{r}) \psi_m(\mathbf{r})}{|\mathbf{r} - \mathbf{r}'|}. \quad (77)$$

Combining equations 72, 73 and 77 the correlation energy within the ACFDT in real space is written as

$$E_c = - \int_0^1 d\lambda \int d^3r d^3r' \frac{e^2}{|\mathbf{r} - \mathbf{r}'|} \int_0^\infty (\chi^\lambda(\mathbf{r}, \mathbf{r}', i\omega) - \chi^{\text{KS}}(\mathbf{r}, \mathbf{r}', i\omega)). \quad (78)$$

and in reciprocal space as

$$E_c = - \int_0^1 d\lambda \int_0^\infty \frac{d\omega}{2\pi} \sum_{\mathbf{q}} \sum_{\mathbf{G}} v_{\mathbf{G}, \mathbf{G}'}(\mathbf{q}) (\chi_{\mathbf{G}, \mathbf{G}'}^\lambda(\mathbf{q}, i\omega) - \chi_{\mathbf{G}, \mathbf{G}'}^{\text{KS}}(\mathbf{q}, i\omega)) \quad (79)$$

where the bare Coulomb interaction is given as

$$v_{\mathbf{G}, \mathbf{G}'}(\mathbf{q}) = \frac{4\pi e^2}{|\mathbf{q} + \mathbf{G}|^2} \delta_{\mathbf{G}, \mathbf{G}'}. \quad (80)$$

### 1.5.3 Total energies within the RPA

The correlation energy from equation 79 is in principle exact as long as the response function of the interacting system  $\chi^\lambda$  is known. The response function within the RPA is related to the response function of the Kohn–Sham system via the Dyson equation

$$\chi_{\mathbf{G}, \mathbf{G}'}^{\lambda, \text{RPA}}(\mathbf{q}, i\omega) = \sum_{\mathbf{G}''} (1 - \lambda \chi_{\mathbf{G}, \mathbf{G}''}^{\text{KS}}(\mathbf{q}, i\omega) v_{\mathbf{G}, \mathbf{G}''}(\mathbf{q}))^{-1} \chi_{\mathbf{G}'', \mathbf{G}'}^{\text{KS}}(\mathbf{q}, i\omega). \quad (81)$$

By defining the trace [60]

$$\text{Tr}\{v\chi^{\lambda, \text{RPA}}\} = \sum_{\mathbf{q}} \sum_{\mathbf{G}, \mathbf{G}'} v_{\mathbf{G}, \mathbf{G}'} \chi_{\mathbf{G}', \mathbf{G}}^{\lambda, \text{RPA}} \quad (82)$$

and using the relationship [60]

$$\text{Tr}\{v\chi^{\lambda, \text{RPA}}\} = -\frac{\partial}{\partial \lambda} \text{Tr}\{\ln[1 - \lambda \chi^{\text{KS}} v]\} \quad (83)$$

the  $\lambda$  integration in equation 79 is avoided and the RPA correlation energy is given as follows

$$\begin{aligned}
E_c^{\text{RPA}} &= \int_0^\infty \frac{d\omega}{2\pi} \text{Tr}\{\ln[1 - \chi^{\text{KS}}v] + v\chi^{\text{KS}}\} \\
&= \int_0^\infty \frac{d\omega}{2\pi} \sum_{\mathbf{q}} \sum_{\mathbf{G}, \mathbf{G}'} \{\ln[1 - \chi_{\mathbf{G}, \mathbf{G}'}^{\text{KS}}(\mathbf{q}, \omega)v_{\mathbf{G}, \mathbf{G}'}(\mathbf{q})] + v_{\mathbf{G}, \mathbf{G}'}(\mathbf{q})\chi_{\mathbf{G}, \mathbf{G}'}^{\text{KS}}(\mathbf{q}, \omega)\}.
\end{aligned} \tag{84}$$

The trace of the logarithm of the matrix  $1 - \chi^{\text{KS}}v$  is easily calculated using the following relationship [61, 62]

$$\text{Tr}\{\ln[A]\} = \ln[\det\{A\}]. \tag{85}$$

The frequency integration is usually carried out using a Gauss-Legendre integration scheme (see appendix 5.3).

Finally the total energy within the ACFDT using the RPA is given as the sum of the Hartree–Fock energy evaluated at the Kohn–Sham wave functions plus the correlation energy as given in equation 84

$$E_{\text{tot}} = E_{\text{HF}}[\psi^{\text{KS}}] + E_c^{\text{RPA}}[\chi^{\text{KS}}]. \tag{86}$$

## 1.6 GWA

### 1.6.1 Green’s function

Before we discuss the GW approximation [63, 64] (GWA) we have to define the one-body Green’s function  $G(\mathbf{x}, \mathbf{x}', t, t')$  of an interacting system which is the fundamental quantity needed in perturbation theory

$$G(\mathbf{x}, \mathbf{x}', t, t') = -i\langle\psi|\mathbf{T}[\hat{\psi}(\mathbf{x}, t)\hat{\psi}^+(\mathbf{x}', t')]| \psi\rangle \tag{87}$$

where  $\mathbf{x}$  describes the spatial and spin coordinates  $\mathbf{x} = (\mathbf{r}, s)$ .  $\mathbf{T}$  is the time-ordering operator and  $\hat{\psi}(\mathbf{x}, t)$ ,  $\hat{\psi}^+(\mathbf{x}', t')$  are annihilation and creation operators in the Heisenberg picture for the Hamiltonian of the interacting system  $\hat{H}$  in second quantization [65]

$$\begin{aligned}
\hat{H} &= \int dx \hat{\psi}^+(\mathbf{x}, t)h_0\hat{\psi}(\mathbf{x}, t) \\
&\quad + \frac{1}{2} \int dx dx' \frac{1}{|\mathbf{r} - \mathbf{r}'|} \hat{\psi}^+(\mathbf{x}, t)\hat{\psi}^+(\mathbf{x}', t')h_0\hat{\psi}(\mathbf{x}', t')h_0\hat{\psi}(\mathbf{x}, t).
\end{aligned} \tag{88}$$

The Green’s function describes the probability of finding an electron at  $\mathbf{x}$  when another electron is added to the system at  $\mathbf{x}'$ . In other words one can calculate the energies needed to add or remove an electron from the system.

## 1.7 Quasi-particle equation

The Green's function for a non-interacting system is in frequency space defined as

$$G_0(\mathbf{x}, \mathbf{x}', \omega) = (\omega - H_0(\mathbf{x}))^{-1} \quad (89)$$

where

$$H_0(\mathbf{x}) = -\frac{1}{2}\nabla^2 + v(\mathbf{x}). \quad (90)$$

The relation between the interacting Green's function and the non-interacting Green's function is given as follows

$$G = G_0 + G_0 \Sigma_{xc} G. \quad (91)$$

where all many-body effects describing exchange and correlation are included within the exchange-correlation self-energy operator  $\Sigma_{xc}$ . Equation 91 is known as the Dyson equation [66] for the Green's function.

The single-particle excitation energies of a many-body system are given by the poles of the Green's function of the interacting system. Since the electron removal or addition is screened by the other electrons we are referring to quasi-particles instead of electrons. The quasi-particle wave functions  $\psi_{n\mathbf{k}}(\mathbf{x}, \omega)$  and quasi-particle eigenenergies  $\varepsilon_{n\mathbf{k}}(\omega)$  are obtained as solutions to the following equation

$$H_0(\mathbf{x})\psi_{n\mathbf{k}}(\mathbf{x}, \omega) + \int dx' \Sigma_{xc}(\mathbf{x}, \mathbf{x}', \omega)\psi_{n\mathbf{k}}(\mathbf{x}', \omega) = \varepsilon_{n\mathbf{k}}(\omega)\psi_{n\mathbf{k}}(\mathbf{x}, \omega). \quad (92)$$

Equation 92 is usually replaced by the quasi-particle equation

$$H_0(\mathbf{x})\psi_{n\mathbf{k}}(\mathbf{x}) + \int dx' \Sigma_{xc}(\mathbf{x}, \mathbf{x}', \varepsilon_{n\mathbf{k}})\psi_{n\mathbf{k}}(\mathbf{x}') = \varepsilon_{n\mathbf{k}}\psi_{n\mathbf{k}}(\mathbf{x}). \quad (93)$$

where the quasi-particle energies are at the poles of the corresponding Green's function  $G(\mathbf{x}, \mathbf{x}', \omega)$ .

### 1.7.1 Hedin's equations

The self-energy operator  $\Sigma_{xc}$  itself is a very complex quantity. In 1965 Hedin [67] established a formalism for the calculation of  $\Sigma_{xc}$  by relating it to the dynamically screened Coulomb interaction

$$W = \epsilon^{-1}v \quad (94)$$

where  $\epsilon$  is the dielectric function and  $v$  is the bare coulomb potential. Since the derivation of Hedin's equations is quite lengthy we will refer the reader to

references [67, 68] for a detailed derivation. The final expressions for Hedin's equations are given as follows

$$P(12) = -i \int d(34)G(13)G(41^+)\Gamma(342) \quad (95)$$

$$W(12) = v(12) + \int d(34)W(13)P(34)v(42) \quad (96)$$

$$\Sigma(12) = i \int d(34)G(14^+)W(13)\Gamma(432) \quad (97)$$

$$\Gamma(123) = \delta(12)\delta(13) + \int d(4567)\frac{\partial\Sigma(12)}{\partial G(45)}G(46)G(75)\Gamma(673) \quad (98)$$

$$G(12) = G_0(12) + \int d(34)G_0(13)\Sigma(34)G(42) \quad (99)$$

where the numbers in parenthesis denote the spatial and spin coordinates and the corresponding time ( $n = \mathbf{x}_n, t_n$ ).  $P$  is the irreducible polarizability or screened response function (see chapter 1.4.3) and  $\Gamma$  is the so called vertex function. These equations can be solved self-consistently starting with an initial Green's function  $G_0$  and following the cycle given in figure 1.

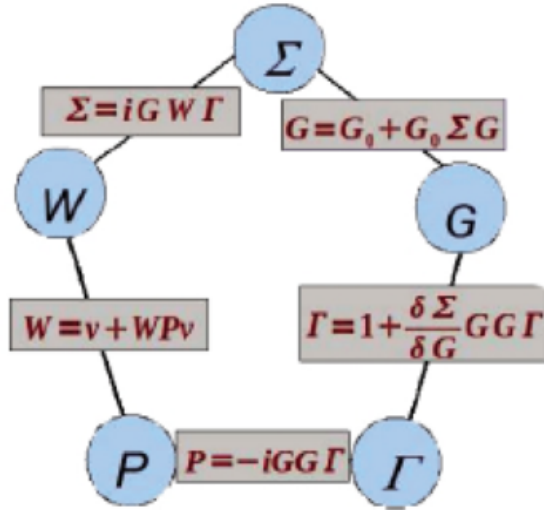


Figure 1: Schematic representation of Hedin's equations taken from reference [69].

### 1.7.2 GW approximation

Hedin's equations are in principle exact but highly complicated and impossible to solve exactly even for small systems. The most common approximation

is the GW approximation (GWA) which is given by the zero-order approximation for the vertex function

$$\Gamma(123) = \delta(12)\delta(13). \quad (100)$$

Consequently the self-energy operator becomes the product of a Green's function and the screened Coulomb interaction

$$\Sigma(12) = iG(12^+)W(21) \quad (101)$$

hence the name "GW" approximation. Since the vertex function in the GWA consists only of two delta functions the irreducible polarizability becomes the product of two Greens' functions

$$P(12) = -iG(12)G(21^+) \quad (102)$$

which is equal to the RPA.

As mentioned above the GWA is in principle calculated self-consistently, but since the Kohn–Sham wave functions are often good zeroth-order approximations to the quasi-particle wave functions, the quasi-particle energies  $\varepsilon_{nk}^{\text{QP}}$  are calculated as first-order corrections to the Kohn–Sham eigenvalues  $\varepsilon_{nk}^{\text{KS}}$ , which is known as  $G_0W_0$  method. The quasi-particle energies are then given as follows

$$\varepsilon_{nk}^{\text{QP}} = \varepsilon_{nk}^{\text{KS}} + Z_{nk}(\varepsilon_{nk}^{\text{KS}}) \langle \psi_{nk}^{\text{KS}} | \Sigma_{xc}(\varepsilon_{nk}^{\text{KS}}) - V_{xc}^{\text{KS}} | \psi_{nk}^{\text{KS}} \rangle \quad (103)$$

with the renormalization factor

$$Z_{nk}(\varepsilon_{nk}^{\text{KS}}) = \left( 1 - \text{Re} \left[ \langle \psi_{nk}^{\text{KS}} | \left( \frac{\partial \Sigma_{xc}(\omega)}{\partial \omega} \right)_{\omega=\varepsilon_{nk}^{\text{KS}}} | \psi_{nk}^{\text{KS}} \rangle \right] \right)^{-1}. \quad (104)$$

The Green's functions for the fully interacting system are replaced by the non-interacting Green's functions  $G_0$  from the Kohn–Sham calculations

$$G_0(\mathbf{r}, \mathbf{r}', \omega) = \sum_{nk} \frac{\psi_{nk}^{\text{KS}}(\mathbf{r}) \psi_{nk}^{\text{KS}*}(\mathbf{r}')}{\omega - \varepsilon_{nk}^{\text{KS}} - i\eta \text{sgn}(\varepsilon_F - \varepsilon_{nk}^{\text{KS}})} \quad (105)$$

where  $\eta$  is a small positive number and  $\varepsilon_F$  is the Fermi energy.  $W_0(\mathbf{r}, \mathbf{r}', \omega)$  is given as follows

$$W_0(\mathbf{r}, \mathbf{r}', \omega) = \int \varepsilon^{-1}(\mathbf{r}, \mathbf{r}'', \omega) v(\mathbf{r}, \mathbf{r}') d\mathbf{r}'' \quad (106)$$

where the dielectric function is obtained using equation 59. The self-energy operator is usually decomposed into two terms for convenience

$$\Sigma(\mathbf{r}, \mathbf{r}', \omega) = \Sigma^x(\mathbf{r}, \mathbf{r}') + \Sigma^c(\mathbf{r}, \mathbf{r}', \omega) \quad (107)$$

The exchange term  $\Sigma^x$  is given by the Hartree–Fock potential

$$\Sigma^x(\mathbf{r}, \mathbf{r}') = i \int G_0(\mathbf{r}, \mathbf{r}', \omega') v(\mathbf{r}, \mathbf{r}') d\omega' = - \sum_{n\mathbf{k}} f_{n\mathbf{k}} \psi_{n\mathbf{k}}(\mathbf{r}) v(\mathbf{r}, \mathbf{r}') \psi_{n\mathbf{k}}^*(\mathbf{r}') \quad (108)$$

where  $f_{n\mathbf{k}}$  denotes the occupation number of the state  $n\mathbf{k}$ . The correlation term  $\Sigma^c$  is given as

$$\Sigma^c(\mathbf{r}, \mathbf{r}', \omega) = i \int G_0(\mathbf{r}, \mathbf{r}', \omega + \omega') (W_0(\mathbf{r}, \mathbf{r}', \omega') - v(\mathbf{r}, \mathbf{r}')) d\omega'. \quad (109)$$

In many cases it has been proven that the quasi-particle energies can be further improved by introducing partial self-consistency where only the eigenvalues  $\varepsilon_{n\mathbf{k}}$  in equation 105 are replaced by the newly obtained quasi-particle energies but the dynamically screened Coulomb interaction  $W$  is kept the same [70]. This method is known as  $\text{GW}_0$  or energy-only GW method.

It should be noted that fully self-consistent calculations of the GW are available [71–75], but since the calculation  $W$  is very costly, only the  $\text{GW}_0$  is used throughout this work.

## 1.8 Electron-hole interactions

In the previous chapter we discussed excitations where an electron is added to ( $N \rightarrow N + 1$ ) or removed from ( $N \rightarrow N - 1$ ) the system, which are important for photo-electron emission and inverse photo-emission spectroscopy. In this chapter we discuss electron-hole excitations where the total number of electrons is not changed ( $|N, 0\rangle \rightarrow |N, S\rangle$ ) as e.g. in absorption spectroscopy.

### 1.8.1 Bethe–Salpeter equation

The electron-hole interactions are described by the two-particle Green's function and its equation of motion which is also known as Bethe–Salpeter equation [76] (BSE). The derivation of the BSE is lengthy and the reader is referred to references [77–79] for a complete description. The BSE for the correlation function  $L(12, 1'2')$  is given as

$$L(1, 1', 2, 2') = L_0(1, 1', 2, 2') + \int d(3, 3', 4, 4') L_0(1, 1', 3, 3') K(3, 3', 4, 4') L(4, 4', 2, 2') \quad (110)$$



where

$$L_0(1, 1', 2, 2') = G_0(1, 2')G_0(2, 1') \quad (111)$$

describes free electron-hole pairs. The numbers in parenthesis comprises spatial, spin and time variables ( $i = \mathbf{r}_i, s_i, t_i$ ).  $K(3, 3', 4, 4')$  is the so called electron-hole interaction kernel which is an effective two particle interaction given as the functional derivative of the self-energy energy operator plus Hartree potential  $V_H$  with respect to the single particle Green's function

$$K(3, 3', 4, 4') = \frac{\delta[V_H(4)\delta_{4,4'} + \Sigma_{xc}(4, 4')]}{\delta G(3, 3')}. \quad (112)$$

In the so called screened interaction approximation the self-energy operator in equation 112 is approximated in the GWA. By additionally assuming that the derivative of the dynamically screened interaction  $W$  with respect to  $G$  is negligible the electron-hole interaction kernel is written as

$$\begin{aligned} K(3, 3', 4, 4') &= -i\delta_{3,3'}\delta_{4,4'}v_{3,4} + i\delta_{3,4}\delta_{3',4'}W(3, 3') \\ &= K^x(3, 3', 4, 4') + K^d(3, 3', 4, 4'). \end{aligned} \quad (113)$$

where  $K^x$  and  $K^d$  are the so-called exchange and direct term, respectively. The direct term describes the attractive electron-hole interactions and is responsible for the formation of bound electron-hole states as e.g. excitons, whereas the exchange term controls the splitting between states (e.g., splitting between singlet and triplet states).

When equation 110 is Fourier transformed to frequency space only the difference of two time variables is important due to the homogeneity in the absence of external fields and the number of frequency indices is reduces to one  $L(\mathbf{x}_1, \mathbf{x}'_1, \mathbf{x}_2, \mathbf{x}'_2, \omega)$ , where  $\mathbf{x}_i = \mathbf{r}_i, s_i$ . The correlation function is then written in frequency space as follows

$$\begin{aligned} L(\mathbf{x}_1, \mathbf{x}'_1, \mathbf{x}_2, \mathbf{x}'_2, \omega) &= i \sum_S \left( \frac{\Xi_S(\mathbf{x}_1, \mathbf{x}'_1)\Xi_S^*(\mathbf{x}'_2, \mathbf{x}_2)}{\omega - E_{eh}^S} \right. \\ &\quad \left. - \frac{\Xi_S(\mathbf{x}_2, \mathbf{x}'_2)\Xi_S^*(\mathbf{x}'_1, \mathbf{x}_1)}{\omega + E_{eh}^S} \right) \end{aligned} \quad (114)$$

where the index  $S$  denotes electron-hole excitations with the corresponding excitation energies  $E_{eh}^S$  and electron-hole amplitudes

$$\Xi(\mathbf{x}_i, \mathbf{x}'_i) = -\langle \psi^0 | \hat{\psi}^+(\mathbf{x}'_i)\hat{\psi}(\mathbf{x}_i) | \psi^S \rangle. \quad (115)$$

By expressing equation 115 as combinations of occupied and empty bands

$$\Xi(\mathbf{x}_i, \mathbf{x}'_i) = \sum_v^{\text{occ}} \sum_c^{\text{empty}} A_{vc}^S \psi_c(\mathbf{x})\psi_v^*(\mathbf{x}') + B_{vc}^S \psi_v(\mathbf{x})\psi_c^*(\mathbf{x}') \quad (116)$$

the BSE can be reformulated into the following eigenvalue equations

$$\begin{aligned}
(\varepsilon_c - \varepsilon_v)A_{vc}^S + \sum_{v'c'} K_{vc,v'c'}^{AA}(E_{\text{eh}}^S)A_{v'c'}^S \\
+ \sum_{v'c'} K_{vc,v'c'}^{AB}(E_{\text{eh}}^S)B_{v'c'}^S = E_{\text{eh}}^S A_{vc}^S
\end{aligned} \tag{117}$$

and

$$\begin{aligned}
(\varepsilon_c - \varepsilon_v)B_{vc}^S + \sum_{v'c'} K_{vc,v'c'}^{BB}(E_{\text{eh}}^S)B_{v'c'}^S \\
+ \sum_{v'c'} K_{vc,v'c'}^{BA}(E_{\text{eh}}^S)A_{v'c'}^S = -E_{\text{eh}}^S B_{vc}^S.
\end{aligned} \tag{118}$$

It was shown that the contribution of the off diagonal matrix elements  $K^{AB}$  and  $K^{BA}$  are almost zero in Si [80–83]. By assuming the same for other materials we will make the approximation  $K^{AB}, K^{BA} = 0$ . The solutions for the coupling coefficients  $A_{v'c'}^S$  and  $B_{v'c'}^S$  lead then to the same excitation energies but with a negative sign in the case of  $B_{v'c'}^S$ . Knowing this it is sufficient to solve only the equation for  $A_{v'c'}^S$

$$(\varepsilon_c - \varepsilon_v)A_{vc}^S + \sum_{v'c'} K_{vc,v'c'}^{AA} E_{\text{eh}}^S A_{v'c'}^S = E_{\text{eh}}^S A_{vc}^S \tag{119}$$

which is equivalent to the Tamm–Dancoff approximation [65, 84]. The exchange and direct term are given as

$$\langle vc | K_{vc,v'c'}^{AA,x} | v'c' \rangle = \int dx dx' \psi_c^*(\mathbf{x}) \psi_v(\mathbf{x}) v(\mathbf{r}, \mathbf{r}') \psi_{c'}(\mathbf{x}') \psi_{v'}^*(\mathbf{x}') \tag{120}$$

and

$$\begin{aligned}
\langle vc | K_{vc,v'c'}^{AA,d}(E_{\text{eh}}^S) | v'c' \rangle \\
= i \int dx dx' \psi_c^*(\mathbf{x}) \psi_{c'}(\mathbf{x}) \psi_v(\mathbf{x}') \psi_{v'}^*(\mathbf{x}') \int d\omega W(\mathbf{r}, \mathbf{r}', \omega) \\
\times \left[ \frac{1}{E_{\text{eh}}^S - \omega - (E_{c'}^{\text{QP}} - E_v^{\text{QP}})} + \frac{1}{E_{\text{eh}}^S + \omega - (E_c^{\text{QP}} - E_v^{\text{QP}})} \right],
\end{aligned} \tag{121}$$

respectively. It should be noted that the exchange term contains the bare Coulomb interaction  $v$  and the direct term uses the screened Coulomb interaction  $W$  as given in equation 106.

It is common to approximate equation 121 by

$$\langle vc | K_{vc,v'c'}^{AA,d}(E_{\text{eh}}^S) | v'c' \rangle = - \int dx dx' \psi_c^*(\mathbf{x}) \psi_{c'}(\mathbf{x}) \psi_v(\mathbf{x}') \psi_{v'}^*(\mathbf{x}') W(\mathbf{r}, \mathbf{r}', \omega = 0) \tag{122}$$

where the dynamical properties of  $W$  are fully ignored. We will use this approximation throughout this work.

### 1.8.2 Optical spectrum within the BSE

The macroscopic dielectric function in the independent particle picture is given as (see equation 64)

$$\text{Im}\epsilon_{\text{mac}}^{\text{KS}}(\mathbf{q} \rightarrow 0, \omega) = \frac{16\pi^2}{\Omega\omega^2} \sum_{v\mathbf{c}\mathbf{k}} \langle \psi_{v\mathbf{k}} | \hat{\mathbf{p}} | \psi_{c\mathbf{k}} \rangle \langle \psi_{v\mathbf{k}} | \hat{\mathbf{p}} | \psi_{c\mathbf{k}} \rangle \delta(\varepsilon c(\mathbf{k}) - \varepsilon v(\mathbf{k}) - \omega). \quad (123)$$

where  $v$  and  $c$  run over valence and conduction bands, respectively. The excitations are given as vertical transitions between independent electron and hole states. The main effect of the BSE on the macroscopic dielectric function is the coupling of different electron-hole configurations for each excitation channel  $S$  via the coupling coefficient  $A_{vc}^S$

$$\langle \psi^0 | \hat{\mathbf{p}} | \psi^S \rangle = \sum_n \sum_m A_{vc}^S \langle \psi_{v\mathbf{k}} | \hat{\mathbf{p}} | \psi_{c\mathbf{k}} \rangle. \quad (124)$$

The imaginary part of the macroscopic dielectric function using the BSE is consequently written as

$$\begin{aligned} \text{Im}\epsilon_{\text{mac}}^{\text{KS}}(\mathbf{q} \rightarrow 0, \omega) \\ = \frac{16\pi^2}{\Omega\omega^2} \sum_{v\mathbf{c}\mathbf{k}, S} A_{vc}^S \langle \psi_{v\mathbf{k}} | \hat{\mathbf{p}} | \psi_{c\mathbf{k}} \rangle \langle \psi_{v\mathbf{k}} | \hat{\mathbf{p}} | \psi_{c\mathbf{k}} \rangle \delta(\varepsilon c(\mathbf{k}) - \varepsilon v(\mathbf{k}) - \omega). \end{aligned} \quad (125)$$

In contrast to equation 123, where all local field effects are neglected, equation 125 includes local field effects due to the exchange term in the electron-hole excitations [53]. These effects can in many cases cause a significant change of the dielectric function.

## 1.9 Computational details

All DFT calculations throughout this work (if not stated otherwise) were performed using the full-potential LAPW code WIEN2k [85]. The main parameters, e.g. atomic radii, Brillouin zone sampling ( $k$  mesh) and the energy cutoff parameter  $RK_{max}$ , which is the product of the largest reciprocal vector and the smallest atomic radius, are specified in each subsection. All GW calculations were performed with the FHI-GAP code [86] which has a direct interface to WIEN2k. This code is currently under development by Hong Jiang and is freely obtainable from his personal webpage <sup>1</sup>.

---

<sup>1</sup><http://www.chem.pku.edu.cn/jianghgroup/>

## 2 The $F$ center in LiF

Wide gap insulators featuring color centers are considered in a growing number of optical applications [87], such as tunable solid state lasers [88], and have been investigated extensively [89–96] since the 1950s. Many different defects can be hosted in these materials, which are introduced by exposure of the crystal to high energy photons, charged particles, or neutrons. The most simple color center in the rock-salt structure (or the "prototype") is the so called  $F$  center, where an electron is trapped at a vacant anion site. The single electron in its ground state is almost spherically localized in the vacancy with an s-like wave function. The first excited state corresponds to a p-like wave function, which results in an  $s \rightarrow p$  transition and would be naively described by a "particle in a box".

In this chapter we will investigate the  $F$  center in lithium fluoride, which is a prototypical wide-band gap insulator with the largest known band gap [97] of 14.2 eV. Many of the results in this chapter are taken from reference [98] and will not be cited separately.

### 2.1 Review of experimental work

The  $F$  center (together with other color centers) in LiF has been investigated in some older works since the early 1960s [99–103] and recently [104–107]. All measurements obtained a 1 to 1.5 eV broad single peak in the absorption spectrum of the  $F$  center. Dawson and Pooley [105], Schwartz et al. [106] and Baldacchini et al. [107] observed the maximum of the absorption peak at 5.08 eV ( $T \approx 5$  K), at 4.98 eV (room temperature) and at 5.07 eV (room temperature) by optical absorption spectroscopy, respectively.

### 2.2 Review of theoretical work

Several first-principles theoretical investigations for  $F$  centers in LiF have been published in the last few decades but none of them have results which are in close agreement with experiment. These calculations are either based on DFT [108, 109] treating the extended system using periodic boundary conditions or on quantum-chemical [109–112] methods explicitly treating a cluster. Previous DFT calculations were based on the LDA suffering from the well known underestimation of the band gap for insulators [18–20] and the nonphysical de-localization of localized states. Another problem in previous calculations is the use of the independent-particle approximation (IPA) within which the electron-hole interaction is not accounted for in the determi-

nation of the excitation energies of the  $F$  center. Previous quantum-chemical calculations were performed on the Hartree-Fock level neglecting correlation effects from the outset. Moreover, limited cluster and basis-set sizes restrict the accuracy of these calculations.

In the past few years, a few advanced periodic super-cell calculations of defects have been performed with the methods of *ab-initio* many-body perturbation theory such as GWA and BSE for other materials such as  $\text{CaF}_2$  (Ref. [113]),  $\text{SiC}$  (Ref. [114]),  $\text{BN}$  (Ref. [115]),  $\text{MgO}$  (Ref. [116]), and diamond (Ref. [117]). However, to our knowledge, all of these calculations lack a comparison to quantum-chemistry calculations of comparable sophistication.

### 2.3 Modeling the $F$ center

In order to describe an isolated  $F$  center properly we have to use supercells to make the influence of vacancies in neighbouring unit cells on each other as small as possible. The Bravais matrix of the supercell  $A_s$  (following the formalism in reference [118]) is given as

$$A_s = A \cdot S \quad (126)$$

where  $A$  is the initial Bravais matrix,  $S$  is the transformation matrix, which is either a diagonal matrix describing a primitive supercell or a non-diagonal matrix describing, e.g. face-centered or body-centered supercells. The resulting supercell is defined as a  $m_x \times m_y \times m_z$  supercell, where  $m_x, m_y, m_z \in \mathbb{N}$ , with atomic positions in crystallographic coordinates

$$a_{i;c_x,c_y,c_z}^S = S^{-1} \cdot \left( a_i + \begin{pmatrix} c_x \\ c_y \\ c_z \end{pmatrix} \right) \quad \begin{array}{l} c_x = 0, 1, \dots, m_x - 1 \\ c_y = 0, 1, \dots, m_y - 1 \\ c_z = 0, 1, \dots, m_z - 1 \end{array} \quad (127)$$

$$i = 1, 2, \dots, n$$

where  $a$  denotes the atomic positions of the conventional unit cell.

Figure 2 shows the two most important supercells for pristine  $\text{LiF}$ , namely the primitive  $2 \times 2 \times 2$  supercell with 64 and the body-centered cubic  $2 \times 2 \times 2$  supercell with 32 atoms, used throughout this work (additionally there is also a face-centered cubic  $2 \times 2 \times 2$  supercell which is not shown in figure 2). The  $F$  center unit cells are obtained by taking the respective supercells and removing a single fluorine atom resulting in  $\text{Li}_x\text{F}_{x-1}$ . The unit cells for the  $F$ -center model structures considered throughout this work are given in table 1.

Table 1: Stoichiometry and symmetry of the  $F$ -center model structures used throughout this work.

Stoichiometry	Space Group	Space Group Number
$\text{Li}_8\text{F}_7$	$Fm\bar{3}m$	225
$\text{Li}_{16}\text{F}_{15}$	$Im\bar{3}m$	229
$\text{Li}_{32}\text{F}_{31}$	$Pm\bar{3}m$	221
$\text{Li}_{64}\text{F}_{63}$	$Fm\bar{3}m$	225

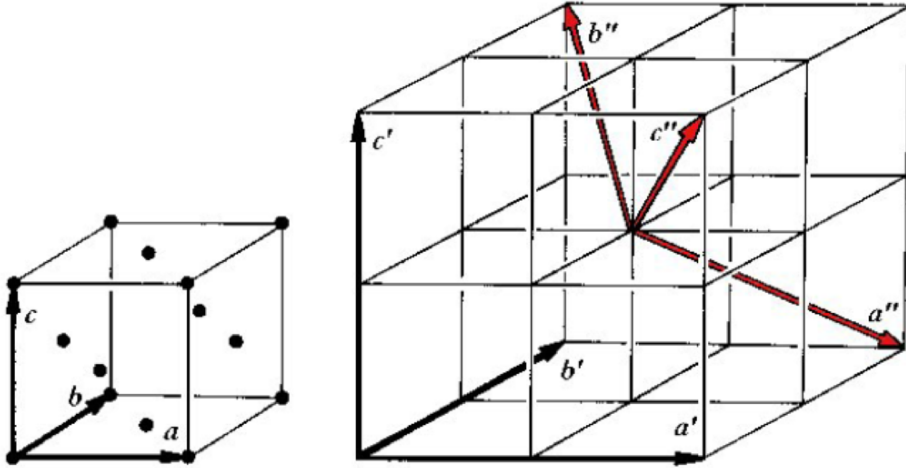


Figure 2: Conventional fcc unit cell and the  $2 \times 2 \times 2$  supercell obtained from the conventional fcc unit cell for LiF.  $a, b, c$ : Lattice vectors of the conventional fcc unit cell.  $a', b', c'$ : Lattice vectors of the primitive  $2 \times 2 \times 2$  - supercell with 64 atoms.  $a'', b'', c''$ : Lattice vectors of the rhombohedral  $2 \times 2 \times 2$  supercell with 32 atoms. Only Li atoms are shown for the conventional fcc unit cell.

## 2.4 Pristine LiF

Before we discuss the  $F$  center in LiF, we briefly review the results obtained for pristine LiF. We used atomic radii of 1.57 and 2.02 for Li and F, respectively, and an energy cutoff parameter  $RK_{max}$  of 7. For all calculations we used the experimental lattice constant of 4.03 Å [97].  $k$ -mesh sizes of  $21 \times 21 \times 21$  for PBE, TB-mBJ and  $10 \times 10 \times 10$  for YS-PBE0,  $\text{GW}_0$  and all BSE calculations were used, respectively.  $Q = 1.0$ , barcevtol=0.0, emingw=-

6 Ha,  $\text{emaxgw}=6.0$  Ha and 16 frequency points within the frequency integration have been used in the GW calculations (for details on these parameters see appendix 5.5.1 and reference [86]).  $6 \text{ Bohr}^{-1}$  and a value of 5 were used for the largest reciprocal vector  $G_{max}$  in the plane wave expansion of the matrix elements within the calculation of the microscopic dielectric function and  $lm_{max}$ , which the largest quantum number of the  $l$  and  $m$  combinations used in the Rayleigh expansion of the plane waves and the wave functions within the muffin-tin spheres (see equations 149 and 150), within the BSE calculations, respectively. 10 Ryd has been used for the cutoff of the conduction bands in the calculation of the microscopic dielectric function, which is used in the screening of the direct term. Due to the very strong localization of the  $F$  center it is sufficient to only consider the s-like valence band and the first three p-like conduction bands of the  $F$  center in the BSE Hamiltonian. A cutoff of 10 Ryd for the largest conduction band was used in the calculation of the microscopic dielectric matrix within the GW and BSE calculations. The calculated band gaps of LiF using different calculational methods are given in figure 3. As expected PBE and HF strongly underestimate and overestimate the band gap by several eV, respectively. Since the YS-PBE0 potential

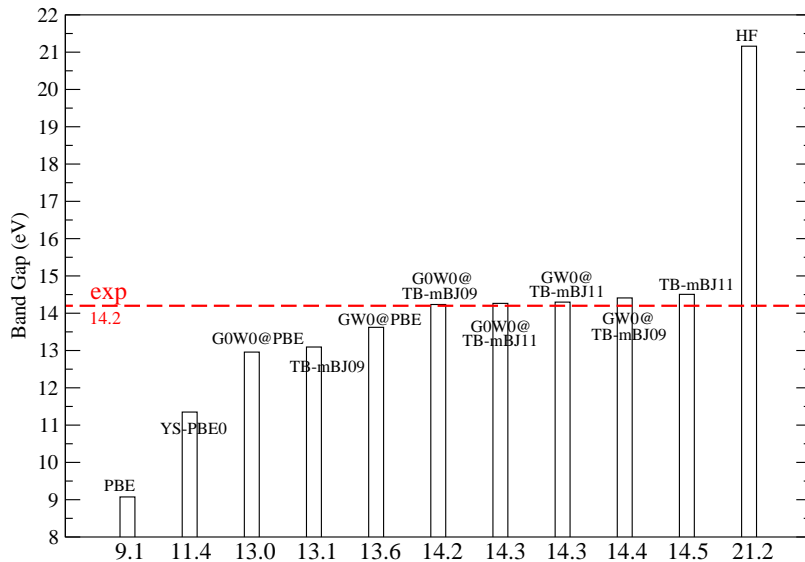


Figure 3: Band gaps for pristine LiF obtained with different calculational methods. Red dotted line: Experimental band gap from reference [97].

uses 25 percent of exact exchange (or HF exchange), it gives, due to an error cancellation of PBE and HF, slightly improved band gaps compared to PBE, but is still strongly underestimating the experimental gap. Both GW and TB-mBJ give results which are in very good agreement with the experiment. We used two different parametrizations for TB-mBJ labelled according to the year they were published (TB-mBJ09 [26] and TB-mBJ11 [28]). The calculated band gaps using these methods with respect to the experimental gaps for many alkali halides are given in figure 4. TB-mBJ09 is parametrized for a

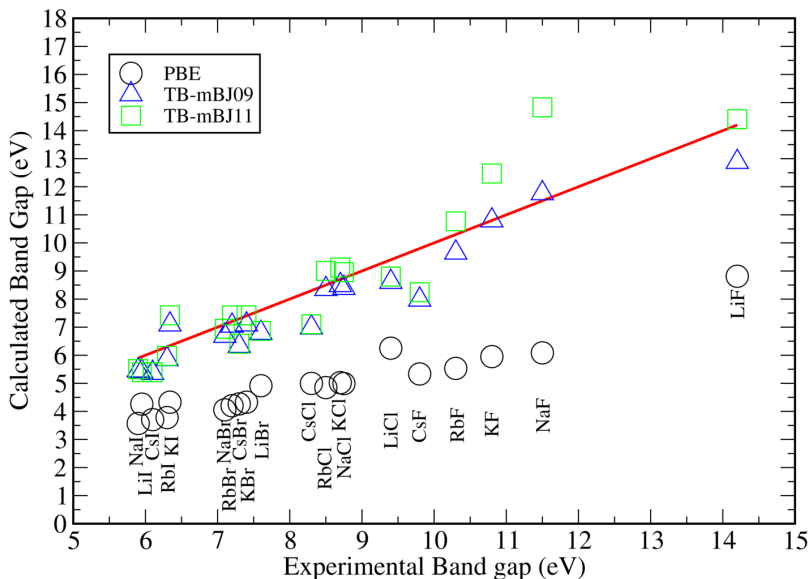


Figure 4: Calculated band gaps vs. experimental gaps for all alkali halides. All calculations were performed using the experimental lattice constants from reference [119].

large number of compounds with strongly varying band gaps. Since the band gap of LiF is more or less an extremum on the list of considered compounds, a broad range parametrization is not accurate enough to give accurate agreement with experiment. The parameters of TB-mBJ11 are mainly obtained for high band gap insulators, hence the excellent agreement with experiment. In the remainder of this work, we will omit the discussion of TB-mBJ09 and refer to TB-mBJ11 as TB-mBJ. Since both the  $G_0W_0$  and the  $GW_0$  corrections are applied perturbatively, the resulting band gaps strongly depend



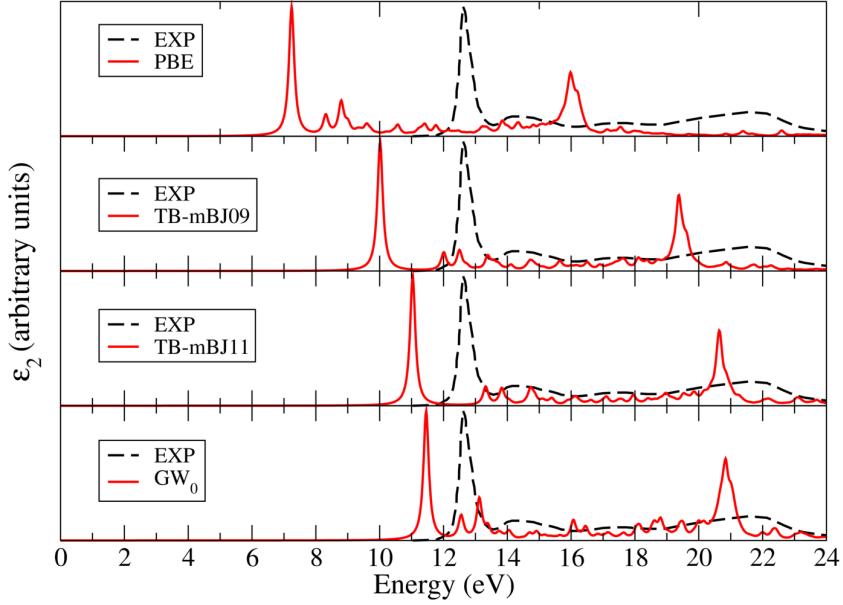


Figure 5: Imaginary part of the macroscopic dielectric function ( $\epsilon_2$ ) of pristine LiF. The experimental absorption spectrum is taken from reference [97].

on the underlying wave functions. Applying these corrections to TB-mBJ leaves the band gap more or less unchanged. This would naively indicate that TB-mBJ describes the wave function of LiF quite well. However if we include electron-hole interactions via BSE calculations and take a look at the imaginary part of the macroscopic dielectric function  $\epsilon_2$ , which is directly proportional to the absorption energy, as given in figure 5 we see that all methods fail to describe the position of the main peak (the excitonic effect of approximately 3 eV for GW and TB-mBJ seems to be too large and shifts the strong first peak too much down in energy). But if we shift the position of the main peak to the one by the experiment (see figure 6) we see that the structure of the absorption spectrum is reproduced quite well for all methods.

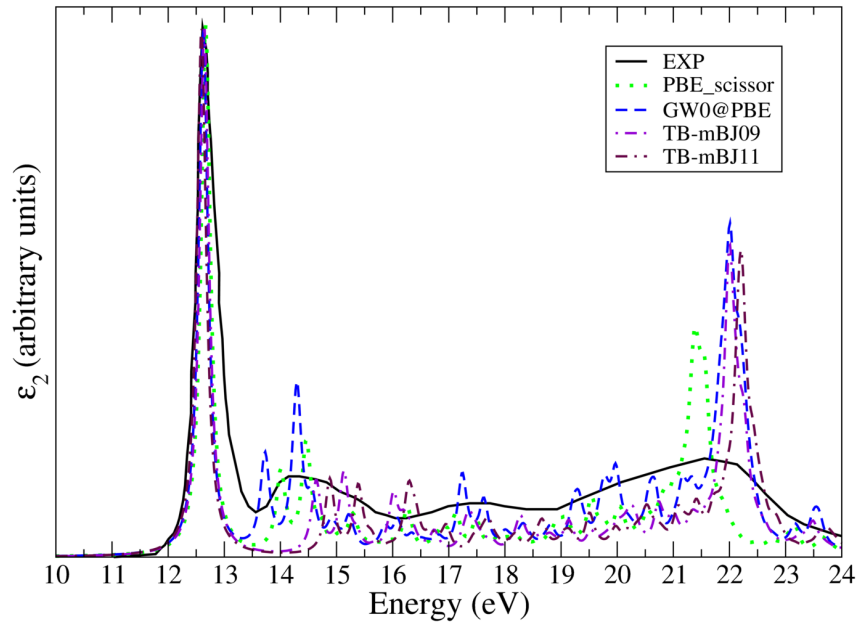


Figure 6: Imaginary part of the macroscopic dielectric function ( $\epsilon_2$ ) of pristine LiF. The position of the main peak in the calculated spectra is shifted to the experimental position.

## 2.5 $F$ -center relaxations and formation energies

The supercells for  $\text{Li}_x\text{F}_{x-1}$  were constructed from the conventional unit cells using the experimental lattice constant of 4.03 Å [97]. All degrees of freedom within the space group of each structure were considered in the structural relaxations. All structure relaxations were calculated using the PBE functional.

The relaxation energy  $\Delta E_{rel}$  is defined as the difference of the total energy of the relaxed structure  $E_r(\text{Li}_x\text{F}_{x-1})$  and the total energy of the unrelaxed structure  $E_u(\text{Li}_x\text{F}_{x-1})$

$$\Delta E_{rel} = E_r(\text{Li}_x\text{F}_{x-1}) - E_u(\text{Li}_x\text{F}_{x-1}). \quad (128)$$

The  $F$ -center formation energy  $\Delta E_{react}$  for the reaction



is given as

$$\Delta E_{react} = E(\text{F}) + E(\text{Li}_x\text{F}_{x-1}) - E(\text{Li}_x\text{F}_x) \quad (130)$$

where  $E(\text{Li}_x\text{F}_x)$  is the total energy of the supercell of pristine lithium fluoride. The total energy of the single fluorine atom  $E(\text{F})$  was calculated by putting a fluorine atom in the center of an empty lattice with a lattice constant that is large enough to minimize the interaction between neighbouring unit cells. A lattice constant of 10.175 Å and a single  $k$  point was sufficient for the calculations. The calculated relaxations of the nearest-neighbour lithium and fluorine atoms in for  $\text{Li}_{32}\text{F}_{31}$  in the [100] plane are plotted in figure 7. It is evident that the relaxations of the next neighbour F and the outer Li atoms (labelled with the numbers 2 and 3 in figure 7) are more or less negligible and the main contribution to the relaxation energy comes from the nearest neighbour Li atoms (the second largest contribution is from a slight inward relaxation of the second nearest neighbour Li atoms in the [110] plane which is not shown in figure 7). But all these relaxations are negligible compared to the size of lattice constant (less than 0.05 Å for the nearest neighbour Li atoms). The relaxation energies and vacancy formation energies with respect to the number of atoms in the unit cell are given in table 2. The relaxation and vacancy energies (second and fifth column in table 2, respectively) are already converged for  $\text{Li}_{16}\text{F}_{15}$  and suggest that this unit cell size is big enough to model an  $F$  center. Although these numbers don't give direct information on how vacancies in neighbouring unit cells are influencing each other, we will show in the next chapter that the influence on the band structure of neighbouring vacancies is almost negligible in  $\text{Li}_{16}\text{F}_{15}$ . Therefore we use  $\text{Li}_{16}\text{F}_{15}$  as the starting point for the more time consuming calculations within this work.

Table 2: Lattice relaxation parameters and relaxation energies as function of unit cell (UC) size.  $E_r$ : relaxation energies,  $d_{Li}, d_F$ : relaxation distances away from the vacancy of nearest-neighbour lithium and fluorine atoms,  $E_{react}$ : removal energies for a single fluorine atom without structural relaxations. All energies in eV, distances in Å.

UC	$E_r$	$d_{Li}$	$d_F$	$E_{react}$
$Li_8F_7$	-0.010	0.02	0.00	8.209
$Li_{16}F_{15}$	-0.014	0.04	0.01	8.208
$Li_{32}F_{31}$	-0.015	0.04	0.01	8.213
$Li_{64}F_{63}$	-0.014	0.04	0.01	8.221

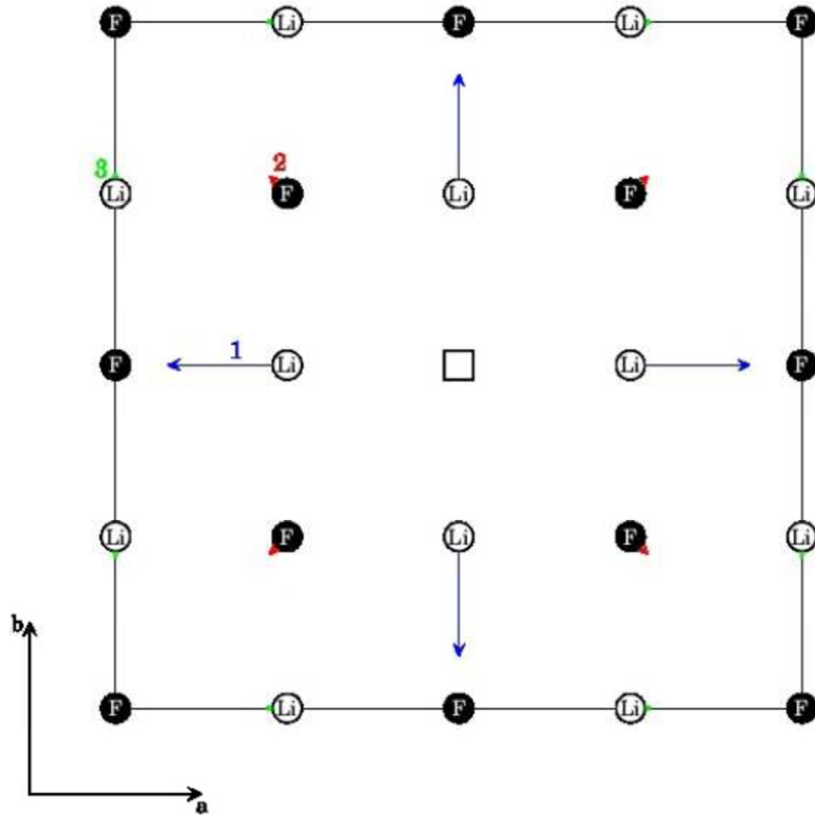


Figure 7: Structural relaxations for  $Li_{32}F_{31}$  in the  $[100]$  plane. Arrows indicate the relative extent of relaxation. 1: Next neighbour Li. 2: Next neighbour F. 3: Second next neighbour Li.

## 2.6 Electronic (band) structure of the $F$ -center

All results presented in this chapter were calculated using the  $\text{Li}_{16}\text{F}_{15}$  and  $\text{Li}_{32}\text{F}_{31}$  cells. For all band structures in this chapter the zero value of the energy axis is shifted to the fermi energy. An  $RK_{max}$  of 7 and a  $k$  mesh of  $3 \times 3 \times 3$  and  $6 \times 6 \times 6$  for  $\text{Li}_{16}\text{F}_{15}$  and  $\text{Li}_{32}\text{F}_{31}$ , respectively, have been used in the calculations. The following parameters have been used for the GW calculations:  $Q = 0.4$ ,  $\text{barcevtol}=0.6$ ,  $\text{emingw}=-3$  Ryd,  $\text{emaxgw}=5.0$  Ryd and 16 frequency points for the frequency integration (for details on these parameters see appendix 5.5.1 and reference [86]).

The band structure of  $\text{Li}_{16}\text{F}_{15}$  for both spins is given in figure 8. The zero point of the ordinate is arbitrarily set to the highest occupied band of pristine lithium fluoride. As expected, PBE strongly underestimates the experimental band-gap (by approximately 5 eV). The occupied valence band (or spin-up band) of the  $F$ -center electron is located in the band gap of lithium fluoride at 5.8 eV in figure 8. The corresponding (unoccupied) band for the other spin (spin-down band) is located slightly above this band (at 7.5 eV). Since the spectroscopic transition rules (see "Fermi's golden rule" [120]) forbid spin flips in excitation processes we are going to omit the discussion of spin-down bands in the remainder of this work.

Not only the band gap (see chapter 2.4 for pristine lithium fluoride) but also the position, dispersion and form of the  $F$ -center bands depends strongly on the underlying calculational method. Figure 9 shows the band gaps for calculations involving PBE, YS-PBE0, TB-mBJ and  $\text{GW}_0$ . At first glance we can see that only TB-mBJ and  $\text{GW}_0$  yield experimental band gaps in good quality. Since the  $F$ -center electron is localized within the vacancy it can be "naively" described by a particle in a box with an s-like character in the ground state, given as a single flat band within the band gap, and with a p-like character in the first excited state, appearing as 3 (degenerate) bands. All methods position the valence band of the  $F$  center inside the gap but at different energies. Since the measurement of the experimental band structure via inverse photoemission spectroscopy for large gap insulators such as lithium fluoride is not available, we cannot say definitely where the exact position of this band is. The  $F$ -center valence band shows very little dispersion for all methods, whereby TB-mBJ has the smallest dispersion. The big difference for the various calculational methods lies in the appearance of the first  $F$ -center conduction bands with p-like character at the lower edge of the conduction bands of pristine lithium fluoride, which are only clearly visible for TB-mBJ. These bands are slightly more energetically delocalized than the valence band, since bands with p-like characteristics are generally more diffuse than s-like bands. The spacial localization and also the s and

p-like characteristics of the  $F$ -center valence and first conduction bands is clearly visible from a contour plot for the wave functions shown in figure 10. By performing a calculation where an empty sphere (with a radius that is equal to the one of fluorine) is put into the vacancy, given in figure 11, we can see that the valence and conduction states are purely of s and p character, respectively. Going back to the band structures in the case of PBE and YS-PBE0 the first conduction bands of the  $F$  center are shifted up compared to TB-mBJ and completely dispersed into the conduction bands of pristine lithium fluoride. By applying  $\text{GW}_0$  on PBE the dispersion of the  $F$ -center bands is reduced (visible as a 3 fold degenerate state at the  $\Gamma$  point inside the conduction bands at 15 eV in figure 9), but since  $\text{GW}_0@PBE$  is a perturbative method and strongly depends on the underlying Kohn–Sham orbitals, it is still not able to correct for all of the delocalization of the bands and to shift the first  $F$ -center conduction bands inside the band gap. In reference [92] it is predicted that the  $F$ -center conduction bands should appear inside the band gap of pristine lithium fluoride, but it lacks any experimental measurements to concretely support this prediction. We also believe that a self-consistent GW calculation (including an update of the wave functions) can give the accurate position of the p-band relative to the conduction-band edge.

A comparison of the band structure for  $\text{Li}_{16}\text{F}_{15}$  and  $\text{Li}_{32}\text{F}_{31}$  using TB-mBJ given in figure 12, shows that the influence of vacancies in neighbouring unit cells on the valence band is only marginally stronger for  $\text{Li}_{16}\text{F}_{15}$ . However, the conduction bands of the  $F$ -center are more delocalized and there is a visible change when going from  $\text{Li}_{16}\text{F}_{15}$  to  $\text{Li}_{32}\text{F}_{31}$ . Nevertheless for the calculation of optical spectra, inclusion of the strong electron-hole interaction upon excitation from the s to the p state turns out to be more important than the exact position and dispersion of the p-bands (see in the following chapter).

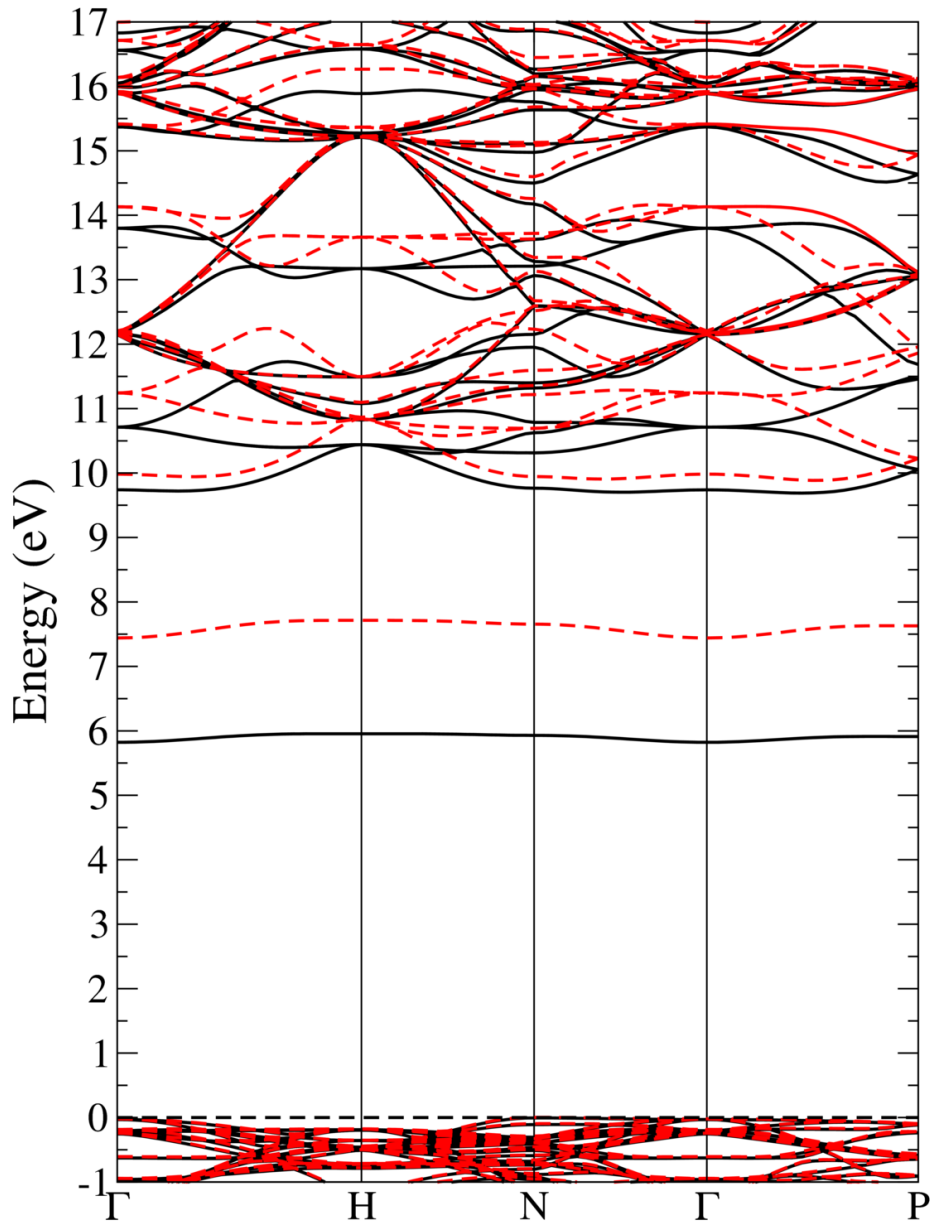


Figure 8: PBE band structure using the  $\text{Li}_{16}\text{F}_{15}$  cell. Black lines: Spin-up bands. Red (dotted) lines: Spin-down bands.

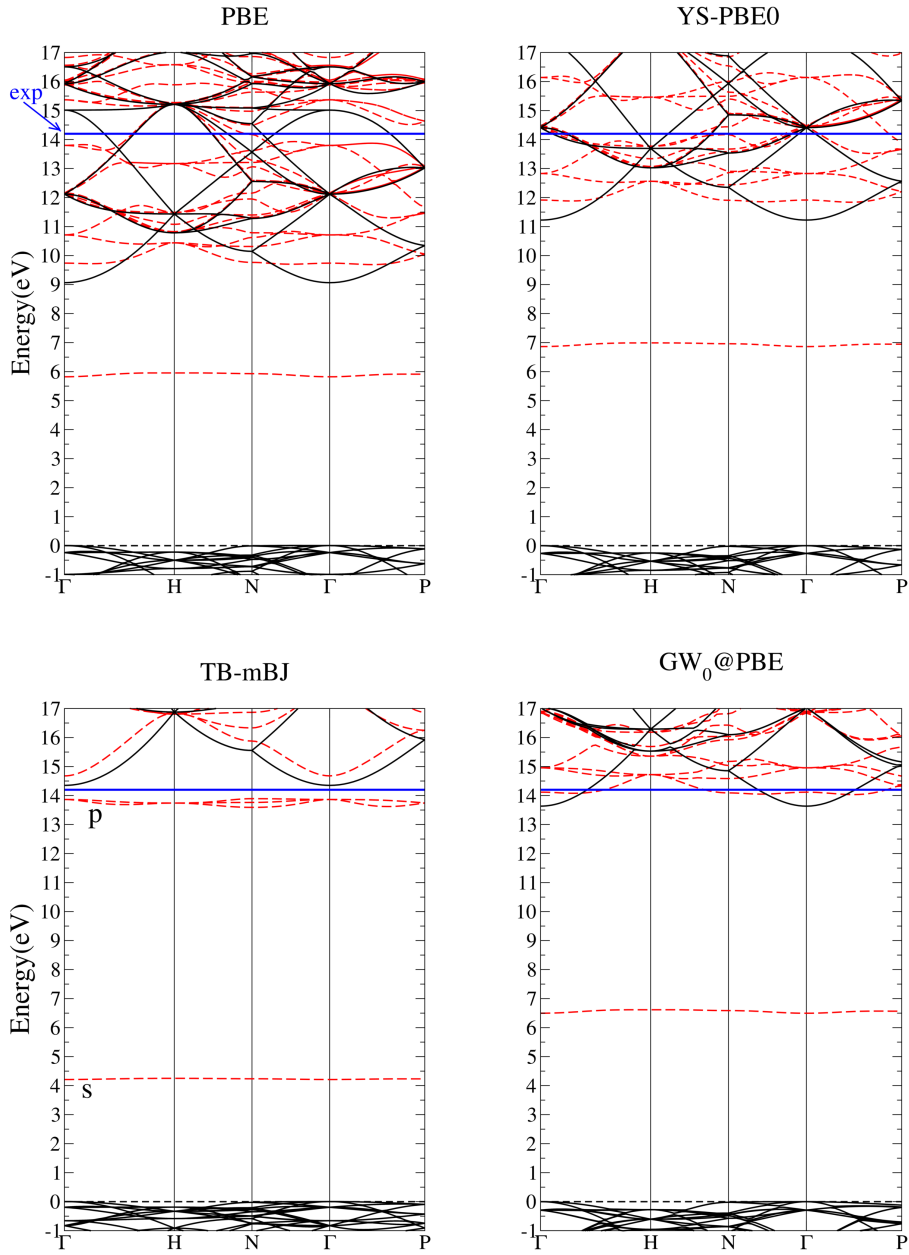


Figure 9: Band structures obtained from PBE, YS-PBE0, TB-mBJ, and  $\text{GW}_0@PBE$  calculations. The black lines (full) show the band structure for perfectly crystalline lithium fluoride with  $\text{Li}_{16}\text{F}_{16}$  chosen as the unit cell. The red lines (dashed) show the highest occupied valence band and the conduction bands for the  $F$ -center structure (only spin-up) from calculations where  $\text{Li}_{16}\text{F}_{15}$  was chosen as the unit cell. The blue line shows the experimental band gap of 14.2 eV (taken from reference [97]).



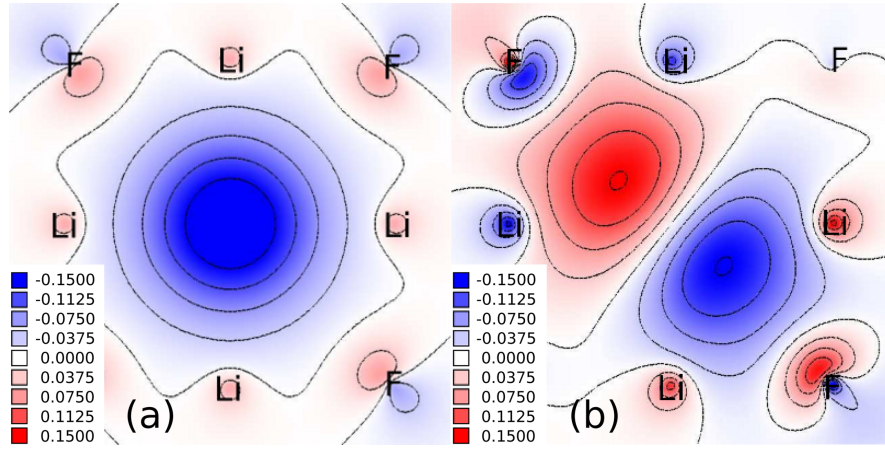


Figure 10: Wave function contour plot within the [100] plane at the  $\Gamma$  point for the  $F$ -center bands in the  $\text{Li}_{32}\text{F}_{31}$  supercell (only spin-up) using TB-mBJ: a) occupied s-orbital, b) one of the three degenerate unoccupied p-orbitals.

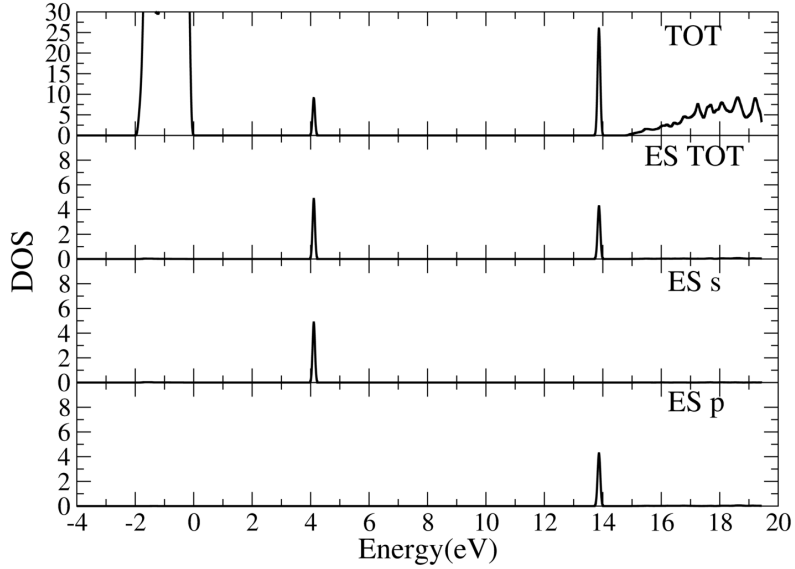


Figure 11: Density of states (DOS) calculated for  $\text{Li}_{32}\text{F}_{31}$  calculated with an empty sphere (with a radius equal to that of fluorine) at the position of the vacancy. The zero point is set to the Fermi level of pristine lithium fluoride. TOT: Total DOS. ES TOT: Total DOS within the empty sphere. ES s, ES p: Partial DOS with s and p-like character within the empty sphere. The units are in (number of states)/eV/unit cell.

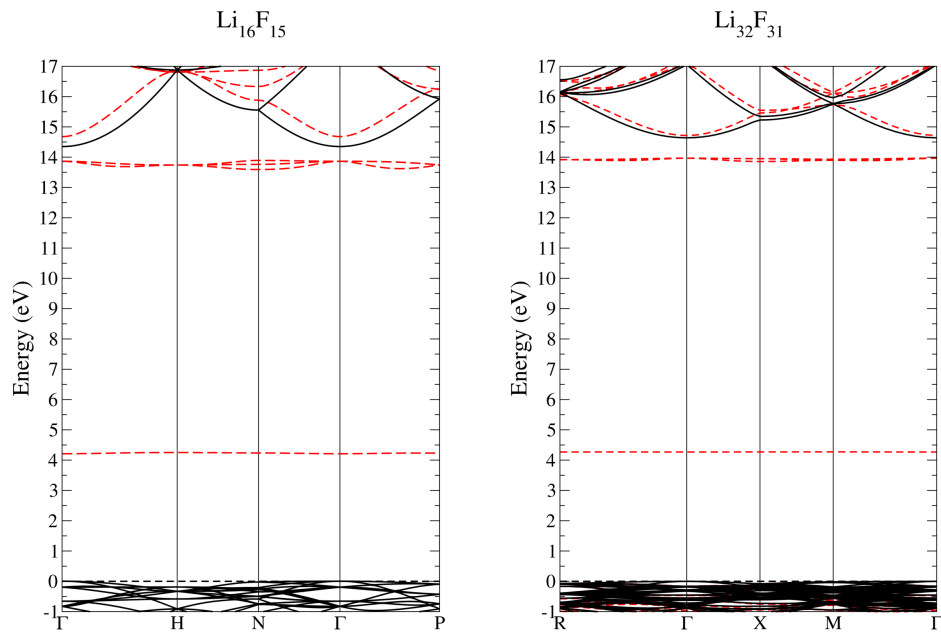


Figure 12: Band structures obtained from TB-mBJ calculations using the  $\text{Li}_{16}\text{F}_{15}$  and  $\text{Li}_{32}\text{F}_{31}$  unit cells. The black lines (full) show the band structure for perfectly crystalline lithium fluoride with  $\text{Li}_{16}\text{F}_{16}$  and  $\text{Li}_{32}\text{F}_{32}$  chosen as the unit cells. The red lines (dashed) show the highest occupied valence band and the conduction bands for the  $F$ -center structure (only spin-up).

## 2.7 Absorption spectra of the $F$ -center

In the independent-particle approximation (IPA), the position of the  $F$ -center absorption peak would be given by the energy difference between the s and the p-band. The resulting absorption spectra (which are proportional to the imaginary parts of the macroscopic dielectric function) are shown in the upper part of figure 13. These results suggest that the absorption maxima of PBE and YS-PBE0 are at 4.5 and 5.5 eV, respectively, close to the experimental absorption maximum of  $\sim 5$  eV while TB-mBJ and  $\text{GW}_0\text{@PBE}$  overestimate it by several eV. We emphasize that using the PBE or YS-PBE0 exchange-correlation potential in the IPA seems to reproduce the absorption maxima in many cases quite well, however, it describes the wrong physics. The agreement with experiment must be considered as accidental as was recently also shown for the  $F$  center [121] in  $\text{MgF}_2$ . The IPA neglects the strong Coulomb attraction between the hole in the s state and the electron in the p state. These excitonic effects, which are taken into account by solving the Bethe–Salpeter equation, significantly change the structure and position of the absorption peaks. This effect depends on the degree of localization of the valence and conduction states and is expected to be large in cases where those states are strongly localized, for instance layered compounds [122] or excitation from core levels [123]. The absorption spectrum including the BSE is shown in the lower part of Fig. 13 for various underlying single-particle approximations. The following parameters have been used in the BSE calculations: A  $k$  mesh of  $6 \times 6 \times 6$ ,  $RK_{max} = 7$ ,  $G_{max} = 2 \text{ Bohr}^{-1}$  for the largest reciprocal vector in the plane wave expansion of the matrix elements within the calculation of the microscopic dielectric function and  $lm_{max} = 2.0$ , which is the largest quantum number of the  $l$  and  $m$  combinations used in the Rayleigh expansion of the plane waves and the wave functions within the muffin-tin spheres (see equations 149 and 150). 10 Ryd has been used for the cutoff of the conduction bands within calculation of the microscopic dielectric matrix, which is used in the screening of the direct term. Due to the very strong localization of the  $F$  center it is sufficient to only consider the s-like valence band and the first three p-like conduction bands of the  $F$  center in the BSE Hamiltonian. Addition of more bands will not change the absorption spectrum significantly. Compared to the measured spectrum, the PBE and YS-PBE0 spectra clearly underestimate the position of the absorption peak by about 2.5 eV. This is due to the strong underestimation of the band gap and thus also of the s $\rightarrow$ p transition energy. The  $\text{GW}_0\text{@PBE}$  spectrum is blue-shifted with respect to the PBE spectrum by about 3 eV and thus matches the experimental spectrum quite well. In the independent-particle approximation, the main absorption peak would be at about 8.0 eV.

Table 3: Convergence of the excitation energies (in eV) with respect to the  $k$ -mesh size calculated for  $\text{Li}_{16}\text{F}_{15}$  using different methods.

$k$ mesh	PBE	YS-PBE0	GW@PBE	TB-mBJ
$3 \times 3 \times 3$	2.38	2.37	5.46	5.54
$4 \times 4 \times 4$	2.38	2.38	5.54	5.12
$5 \times 5 \times 5$	2.38	2.38	5.53	5.04
$6 \times 6 \times 6$	2.38	2.38	5.52	5.00

The down-shift to about 5.5 eV is thus due to the very strong electron-hole attraction between the s and p states which are both localized and thus very close to each other. The TB-mBJ calculations yield an independent-particle transition energy even 1.5 eV higher than for  $\text{GW}_0\text{@PBE}$ . At the same time, screening is weaker and thus the electron-hole attraction is stronger such that the resulting absorption peak is close to the experiment and to the one of  $\text{GW}_0\text{@PBE}$ . The spectrum obtained from TB-mBJ shows a single peak due to transitions between the discrete s and p states as also present in experiment. All other calculations show a large peak together with several weak absorption features appearing as tails at higher energies. This additional side structure is related to the hybridization of the p states of the  $F$  center with the conduction bands of the pristine material. We expect this fine structure to change (or disappear entirely) upon a fully self-consistent GW-calculation that would also change and likely reduce the hybridization of the defect states with the conduction band states. The absorption maximum from TB-mBJ and the absorption maximum of the first peak from  $\text{GW}_0\text{@PBE}$  lie both within 0.5 eV of the experiment.

Noteworthy is that the excitation energies obtained by the different methods converge differently with respect to the  $k$ -mesh size. It can be seen from table 3 that for a  $k$  mesh of  $3 \times 3 \times 3$  a convergence is already obtained for PBE while TB-mBJ exhibits a change of 0.5 eV when going from  $3 \times 3 \times 3$  to  $6 \times 6 \times 6$   $k$  points. This can be ascribed to the strong spatial and energetical localization of the potential for TB-mBJ, since a strongly localized quantity in real space is strongly delocalized in reciprocal space and hence it needs a large  $k$  mesh to describe it properly.

The coupling of electronic and nuclear degrees of freedom may lead to a red shift of the absorption line of the  $F$  center with respect to its Franck-Condon value. The contributions to this shift are extracted by analyzing the energy surfaces along configuration coordinates of calculations involving an embedded cluster. The corresponding quantum chemistry calculations were

carried out by Paul Tiwald<sup>2</sup> using the MOLCAS 7.8 program package [124]. For computational details see appendix 5.4.

By variation of the electronic potential surface along an effective coordinate (Fig. 14), the relaxation energy of the excited state  $E_{relax}$  is extracted as an upper bound for the shift  $\Delta E_{e-ph}$  of the absorption energy, i.e., the difference between the Franck-Condon line (“vertical” excitation) and the zero phonon line (“non-vertical” excitation resulting in lowest possible absorption energy) is extracted. The zero-phonon line corresponds to the excitation from the minimum of the ground state to the minimum of the excited state energy (see

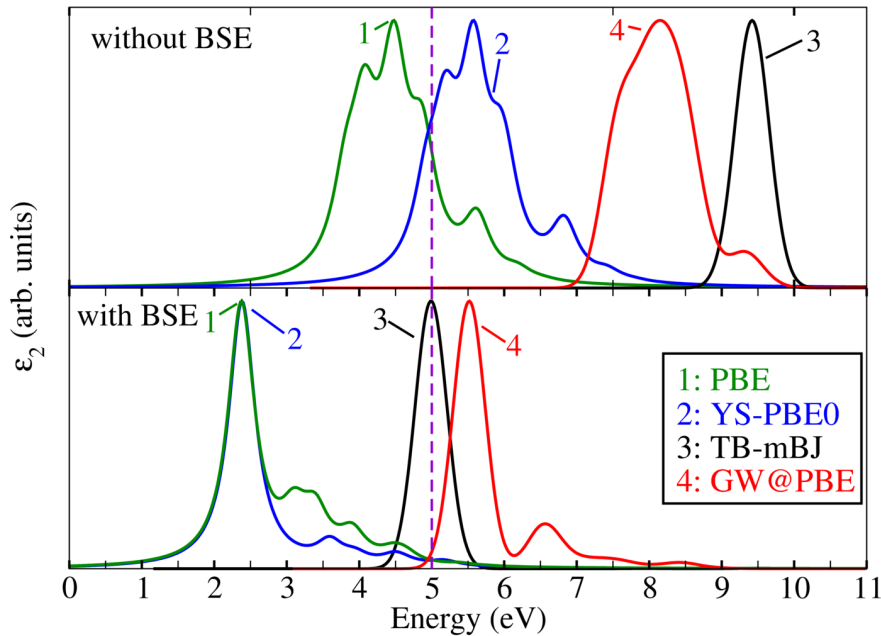


Figure 13: Imaginary part of the dielectric function ( $\epsilon_2$ ) scaled to equal peak height. Top: In the independent-particle approximation (neglecting electron-hole interactions). Bottom: Results with electron-hole interactions taken into account by solving the Bethe–Salpeter equation.  $\text{Li}_{16}\text{F}_{15}$  was chosen as the unit cell. The dashed line indicates the peak position of experimental absorption spectra.

<sup>2</sup>Paul Tiwald, Institute for Theoretical Physics, Vienna University of Technology, Wiedner Hauptstraße 8-10, A-1040 Vienna, Austria

below) within the multidimensional space used in the geometry relaxations. The difference between zero-phonon line and Franck-Condon line amounts to  $E_{relax} \sim 0.5$  eV. This is regarded as an upper bound  $E_{relax} = \Delta E_{e-ph}^{max}$  to the contribution of electron-phonon coupling to the red-shift of the absorption line. The real shift will be generally much lower. Another estimate can be obtained by calculating the overlap of the nuclear wave functions in the ground and excited states for the different n-phonon lines.

Alternatively, within a polaron model the correction to an electronic energy level is given by the polaron self-energy induced by virtual excitations of electrons to the conduction bands and their interaction with longitudinal optical phonons. Accordingly, differences between the polaron self-energies for the electronic ground and excited state of the color center contributes to the shift of the absorption line with respect to its Franck-Condon value. Since in alkali halides electron-phonon coupling is large Feynman's strong-coupling limit for the polaron self-energy [125] (in a.u.eV)  $E_{polaron} = -(0.106\alpha^2 + 2.83)\omega$  can be applied, where  $\alpha$  is the Fröhlich coupling constant [126] and  $\omega$  is the longitudinal optical phonon frequency. The shift of the absorption line is then estimated as  $\Delta E_{e-ph}^{(Q_j)} = -(0.106\alpha^2 + 2.83)\Delta\omega_{Q_j}$  through the largest difference in vibration frequencies  $\Delta\omega_{Q_j}$  of the local normal modes  $Q_j$  involving the six neighboring  $\text{Li}^+$  ions between ground and excited state of the color center. The frequencies were obtained from parabolic fits to configuration coordinate curves. A dominant contribution of  $\Delta\omega_{Q_2} \approx 0.015$  eV is found, where  $Q_2$  corresponds to the stretch vibration shown in Fig. 15. Using the Fröhlich coupling constant of pristine LiF ( $\alpha = 5.25$ ) yields  $\Delta E_{e-ph} = 0.09$  eV.

In Figure 16 a comparison between the experimental absorption spectrum [105] at  $T \approx 5$  K and absorption spectra obtained by the quantum-chemistry and the solid-state physics approaches (DFT) are presented. The experimental spectrum is represented by a Gaussian distribution with parameters for peak position  $E_p = 5.08$  eV and full width at half maximum FWHM=0.61 eV. This peak position is a blue shift relative to the experimental spectrum at room temperature [105] by  $\Delta E_T \approx 0.14$  eV. All theoretical spectra include the calculated zero-temperature line width of 0.27 eV (see appendix 5.4.1) and are shifted towards lower energies by  $\Delta E_{e-ph} = 0.09$  eV due to the influence of electron-phonon coupling. Overall, the calculated absorption spectra with peaks at 5.22 eV (CASPT2(ROHF)), 5.42 eV (GW@PBE + BSE) and 4.9 eV (TB-mBJ + BSE) show good agreement with the experimental data for the  $F$ -center absorption spectrum of LiF.

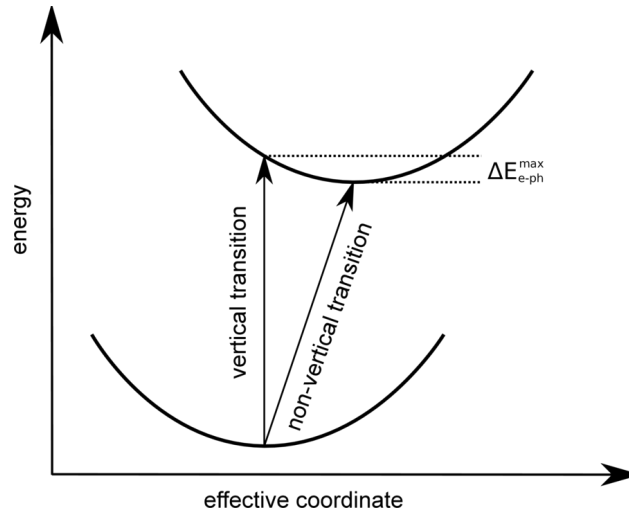


Figure 14: Schematic picture of the electronic potential energy surfaces of ground and excited state of the  $F$  center as a function of an effective coordinate. Arrows indicate the vertical (Franck-Condon like) transition and the non-vertical transition to the minimum of the excited state potential energy surface. The difference  $\Delta E_{e-ph}^{max}$  in energy between these two excitations is an upper bound for the red shift of the absorption line due to electron-phonon interactions.

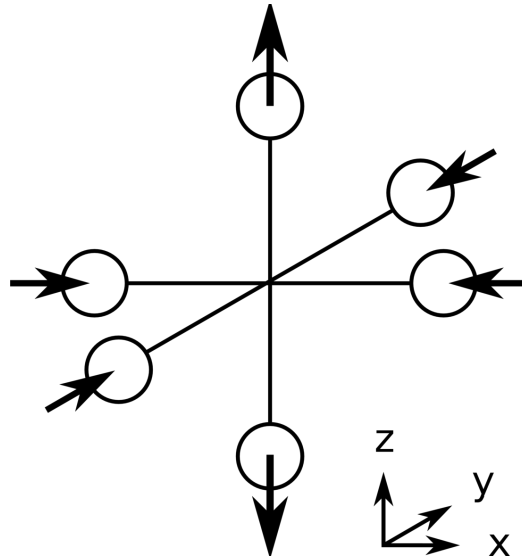


Figure 15: Schematic picture of the stretch vibration of the six  $\text{Li}^+$  ions neighbouring the vacancy responsible for the dominant contribution  $\Delta\omega_{Q_2} \approx 0.015$  eV.

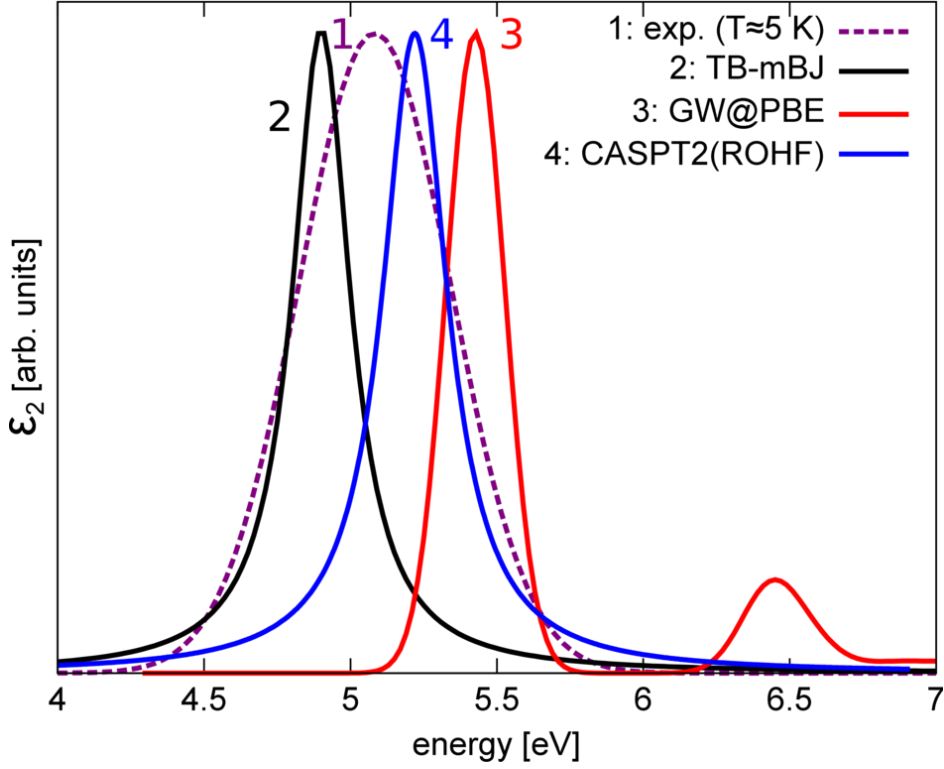


Figure 16: Experimental [105] (dashed line) and calculated (solid lines) absorption spectra of the  $F$  center in LiF. The experimental spectrum is measured at  $T \approx 5$  K and is depicted as a Gaussian function with a peak position of  $E_p = 5.08$  eV and a full width at half maximum of  $\text{FWHM} = 0.61$  eV. Spectra calculated from (post) DFT methods (TB-mBJ + BSE and  $\text{GW}_0$ @PBE + BSE) are determined within a  $\text{Li}_{16}\text{F}_{15}$  unit cell. The quantum chemistry result is obtained from an CASPT2(ROHF) (CASPT2 with a single ROHF determinant) calculation in the converged basis set limit of an  $\text{Li}_{62}\text{F}_{62}$  embedded cluster. All theoretical curves are plotted with a calculated line width at zero temperature of 0.27 eV (see appendix 5.4.1) and contain a red shifted due to electron phonon-coupling of  $\Delta E_{e-ph} = 0.09$  eV.



## 2.8 Summary and conclusions

The  $F$  center is a single electron trapped at a vacant anion site leading to strong energetical and spatial localization of the electron and to so-called "excitons", which are bound electron-hole pairs. This part of the thesis focuses on a quantitative and physically sound description of the structural and electronic properties of the  $F$  center in LiF using state of the art DFT and post-DFT methods (many-body perturbation theory methods). LiF was chosen as the host because it has the largest known band gap of 14.2 eV among the alkali halides and has so the most distinct spatial and energetical localization of the  $F$ -center electron.

The  $F$  center was simulated by using supercells, where a single fluorine is removed from the cell, as the unit cells. For the structural properties the Li32F31 unit cell proved to be large enough and PBE was used for the treatment of the exchange and correlation of the electron. In the structural relaxations the next neighbour Li and F tend to relax away from the  $F$  center but the magnitude of relaxations is more or less negligible.

For the electronic properties the Li16F15 was used. Different calculational schemes have been employed for the exchange and correlation of the electrons: PBE, TB-mBJ, YS-PBE0 (hybrid-DFT functional) and  $\text{GW}_0$ . PBE and YS-PBE0 both underestimate the band gap strongly (approximately 3 to 5 eV) and more importantly describe the wrong physics in the absorption process of the  $F$  center. The TB-mBJ and the  $\text{GW}_0$  both performed equally good describing the band gap and the band structure of the  $F$  center. The error of the calculated band gaps of 14.5 and 13.6 eV for TB-mBJ and  $\text{GW}_0$ , respectively, is within less than 5 percent to the experimental band gap of 14.2 eV.

Since DFT and  $\text{GW}_0$  doesn't include electron-hole interactions the excitonic correction were included by solving the Bethe-Salpeter equations of motion for electron-hole pairs. The corrections turn out to be crucial in the calculation of band gaps and the neglect of these errors can lead to errors of 50 to 100 percent in the absorption energies and to a completely wrong structure of the absorption spectrum. Additionally the spectrum can be further improved by including electron-phonon interactions which. The absorption peak maxima of 4.9 and 5.42 eV for TB-mBJ and  $\text{GW}_0$  (including corrections due to electron-hole and electron-phonon interactions), respectively, are in very close agreement to the experimental peak maximum of 5.08 eV.

This part of the thesis was done in cooperation with Paul Tiwald<sup>3</sup> who calculated the properties of the  $F$  center using embedded clusters and quantum

---

<sup>3</sup>Paul Tiwald, Institute for Theoretical Physics, Vienna University of Technology, Wiedner Hauptstraße 8-10, A-1040 Vienna, Austria

chemistry methods. Not only the wave functions but also the absorption spectrum with a peak maximum of 5.22 eV using CASPT(ROHF) and a  $\text{Li}_{62}\text{F}_{62}$  cluster are in excellent agreement to our and the experimental results.

### 3 Mollwo-Ivey relation in alkali halides

Mollwo [127] and Ivey [128] studied the relations between the lattice constant and the absorption energy of different alkali halides with rock-salt structure. In a first attempt Mollwo estimated the scaling of the absorption energy with respect to the anion-cation distance  $a$  as  $\approx 1/a^2$ . Later Ivey improved this relation by introducing a proportionality constant  $C$  and the so-called Mollwo-Ivey exponent  $n$ . The absorption energy  $E_{\text{abs}}$  is then given within the Mollwo-Ivey relation as follows

$$E_{\text{abs}} = Ca^{-n}. \quad (131)$$

By applying this relation to a large number of experimental results for the  $F$  center absorption energies of many alkali halides with rock salt structure [105, 129] the parameters of the Mollwo-Ivey relation were determined as  $C = 17.3 \pm 2.8$  eV and  $n = 1.81 \pm 0.10$ .

#### 3.1 Review of theoretical work

Some of the early work that contained somewhat oversimplified models such as a nearly-free electron model by Fröhlich [130] and a rigid box model by Stöckmann [131, 132] yield exactly a  $\approx 1/a^2$  behaviour. More sophisticated works are based on a defect electron in a point ion lattice [92]. Using such a model Wood [133] predicts a Mollwo–Ivey exponent of  $n \approx 1.8$  in close agreement with experiment by splitting the absorption energy into a potential and kinetic contribution scaling with  $1 = a$  and  $1 = a^2$ , respectively. Small deviations from the Mollwo–Ivey law are explained by so-called ion-size effects, i.e. the influence of the electronic structure of the ions surrounding the F-center electron. The probably most elegant explanation is given by Malghani and Smith [129, 134] who connect via the Vinti sum rule [135], exactly true only for single-electron systems, different moments of the energy dependent absorption coefficient with the extent of the wave function, i.e.,  $\langle \Psi_s | r^2 | \Psi_s \rangle$ , where  $\langle \Psi_s |$  denotes the ground state wave function of the defect electron. By treating the defect states separately from that of the pristine material, i.e. assuming only two states are involved in the absorption process ( $s \rightarrow p$  transition), one obtains

$$E_{\text{abs}} \approx \frac{3\hbar^2}{2m_e} \frac{1}{\langle s | r^2 | s \rangle}, \quad (132)$$

with  $m_e$  being the mass of the electron. This behavior is due to a potential well, where with increasing box size the spatial extent of the wave function

increases while the level spacing and hence the absorption energy decrease. However, Smith and coworkers [129,134] as well as all studies based on point-ion models set out from, according to the results in this work, incorrect assumptions and draw incomplete conclusions. They assume the spatial extent of the defect wave function to be a continuously increasing function of the lattice parameter essentially independent of the chemical elements building up the crystal. More importantly, they conclude that the Madelung potential is almost solely responsible for forming the potential well the defect electron is bound to and that the so-called ion-size effects play only a minor role. With ion-size effects Smith and co-workers refer to exchange effects, i.e. the Pauli repulsion between the defect electron and the host-crystal ions.

### 3.2 Computational methods

The model defect structures for the other alkali-halides were constructed as described for lithium fluoride in chapter 2.3.  $M_{16}X_{15}$  (where  $M = \text{Li, Na, K}$  and  $X = \text{F, Cl, Br}$ ) was used as the unit cell in all calculations. The structure relaxations were performed using PBE. The electronic properties (band structures and absorption energies) were calculated with the TB-mBJ potential. An energy parameter of  $RK_{max} = 7$  was used with atomic radii of 1.57, 2.04, 2.5 Bohr for Li, Na, K and 2.02, 2.5, 2.6 for F, Cl, Br, respectively. A  $k$ -mesh sampling of  $6 \times 6 \times 6$  for the real materials and  $3 \times 3 \times 3$  for stretched lithium fluoride was chosen, respectively. The electron-hole interactions were calculated analogously to chapter 2. The results for the quantum chemistry calculations for the other alkali halides were obtained analogously to lithium fluoride (see appendix 5.4). All quantum chemistry calculations were carried out by Paul Tiwald <sup>4</sup>.

### 3.3 Madelung and exchange-correlation potential

Many authors in the past identified the Madelung potential as the physical reason underlying the Mollwo–Ivey relation. In fig. 17 (a) the Madelung potential in lithium fluoride at the vacancy site, i.e. the origin, within the [001] crystal plane is plotted. In a large area around the vacancy the Madelung potential is almost flat, varying only slowly. Along the direction towards the nearest-neighbor ions, [100] and [010], it decays monotonically without any barrier that could prevent the defect electron from being attracted by the Coulomb potential of the positive point charges. Since the second-nearest

---

<sup>4</sup>Paul Tiwald, Institute for Theoretical Physics, Vienna University of Technology, Wiedner Hauptstraße 8-10, A-1040 Vienna, Austria

neighbor point ion has a negative charge the Madelung potential is increasing along the  $[110]$  direction. In fig. 17 (b) the effective Kohn–Sham (KS) potential in LiF obtained from periodic DFT calculations is plotted. The result is quite different from the Madelung potential and features an attractive potential well. Its depth (and also the thickness of its walls) depends on the crystal direction and varies between 17 and 25 eV. Qualitatively, the effective KS-potential resembles the model potential used by Buchenauer and Fitchen [136] in their analysis of F-center absorption energies under high pressure. A more detailed picture of the effective KS potential and its com-

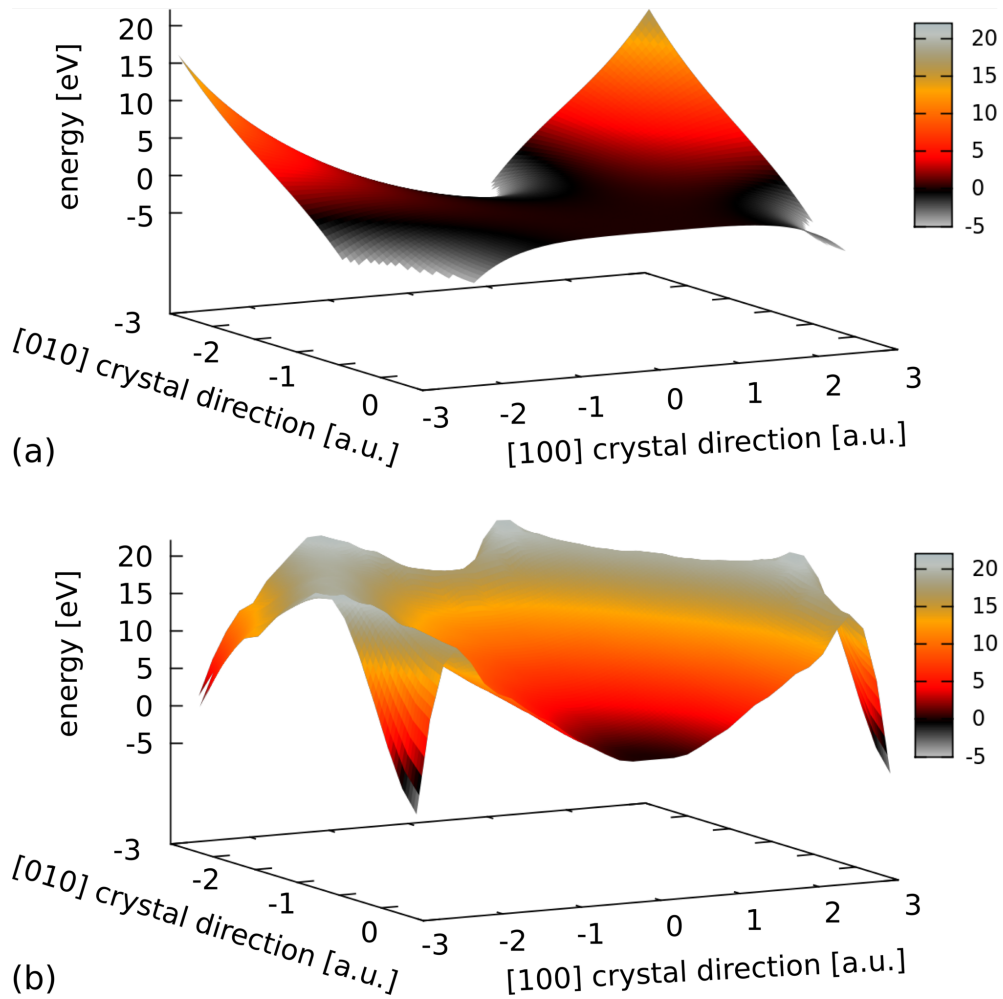


Figure 17: Two-dimensional cut through (a) the Madelung potential and (b) the effective Kohn–Sham potential (obtained from DFT calculations) at the F-center vacancy site, located at the origin, within the  $[001]$  crystal plane.

ponents in LiF is shown in fig. 18. With a green dashed line we plot a cut along the  $[111]$  crystal direction of the Hartree potential, consisting of the electrostatic contributions of the nuclei and the self-consistent electron density. Again the color center is located at the origin. In the defect region it shows purely repulsive character making the formation of a localized color-center electron impossible. It is the exchange-correlation potential (dotted blue line) that is responsible for the formation of an attractive potential well in the total effective Kohn–Sham potential (solid red line). We spot exchange as the dominant mechanism for the well formation since we also observe bound, i.e. well localized, defects in our Hartree–Fock calculations (see below) which, per definition, only account for exchange.

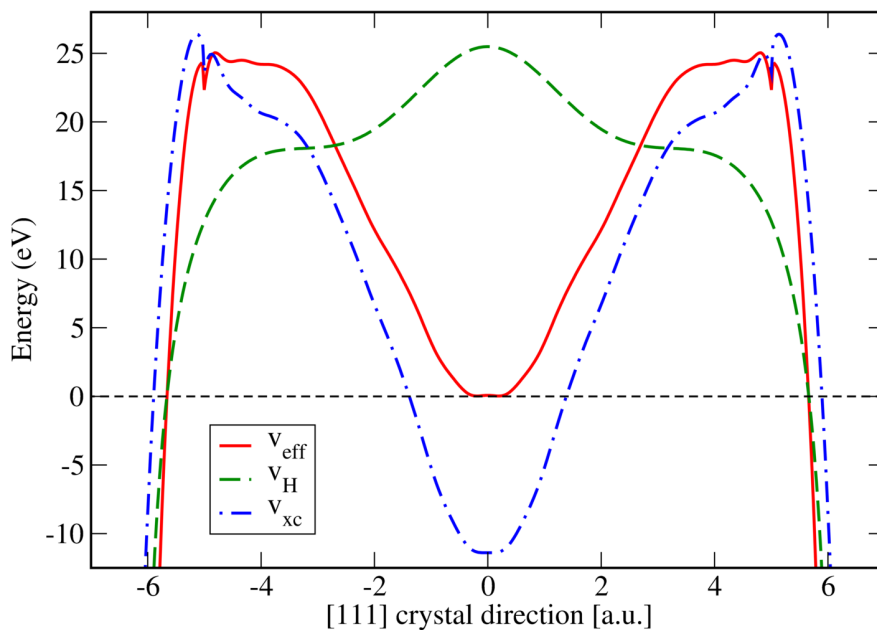


Figure 18: Cut through the effective Kohn–Sham potential (red solid line) in the F-center defect region of an LiF crystal. The red line is the effective Kohn–Sham potential. Green (dashed) and blue (dotted) lines are the Hartree and the exchange-correlation potential, respectively. All potentials obtained from a DFT calculation.

### 3.4 Square well potential model

The effective Kohn–Sham potential in fig. 17 (b) resembles a spherical well potential. Like a square well potential (or naively a "particle in a box"-like model), it leads to an exact inverse square dependence of the F-center absorption energy on its characteristic length scale, the radius of the spherical well, and a linear increase of the spatial extent of the wave function. Such kind of growth is simulated by what is called in the following as stretched LiF. It means the absorption energy of the F-center in (unrelaxed) lithium fluoride at an arbitrary lattice constant or, to be more precise, at the lattice constants of other alkali-halide crystals, is calculated. This approach has the advantage that of “turning off”, or “freezing”, the ion-size effects on the absorption energy and the Mollwo–Ivey relation since for all lattice parameters the same ion species are used. The F-center absorption energies for stretched LiF are shown in fig. 19. We find smoothly varying curves which, at least for larger lattice constants, almost perfectly match the experiment. The calculated Mollwo–Ivey exponents are  $n_{QC} = 2.04$  and  $n_{DFT+BSE} = 1.91$  obtained from quantum chemistry and (post-)DFT calculations, respectively, almost perfectly matching the value 2 predicted by the spherical potential well. In the fitting procedure of the quantum chemistry results the data point of LiF at its natural lattice constant is left out due to the convergence behavior of stretched LiF. Quantum chemistry results for LiF at a lattice constant of already NaF seem to be essentially converged with respect to basis set and cluster size for the cc-pvtz basis set and a  $\text{Li}_{38}\text{F}_{18}$  cluster. This is not the case for real LiF. When adding the converged value [98] for unrelaxed LiF, indicated by the green diamond, it almost perfectly lies on the Mollwo–Ivey line with  $n_{QC} = 2.04$ . As a measure for the spatial extent of the defect wave function in the ground state  $|s\rangle$  the position of its first radial node along the [100] direction  $r_0$  is used and, like Malghani and Smith [129], the root-mean square (rms) radius  $\langle s|r^2|s\rangle^{1/2}$ . The radial node  $r_0$  serves as a directional measure towards the nearest neighbor cation while the rms radius is a spherically integrated measure. Both quantities are extracted from ROHF defect orbitals of the F-center in lithium fluoride for different lattice constants and are depicted in figure 20 together with cuts through the  $|s\rangle$  ROHF wave function along the [100] direction, the latter cut off at  $r_0$  for clarity.  $r_0$  and the rms-radii of the F-center ground state wave function in stretched LiF increase perfectly linear with the lattice distance. A linear increase of the rms radii was also found by Malghani and Smith [129] by applying the Vinti sum rule to experimental absorption spectra. Of course, their analysis was done for the F-center in real materials, not on stretched LiF. They concluded that ion-size effects have only a negligible influence on the spatial extent of

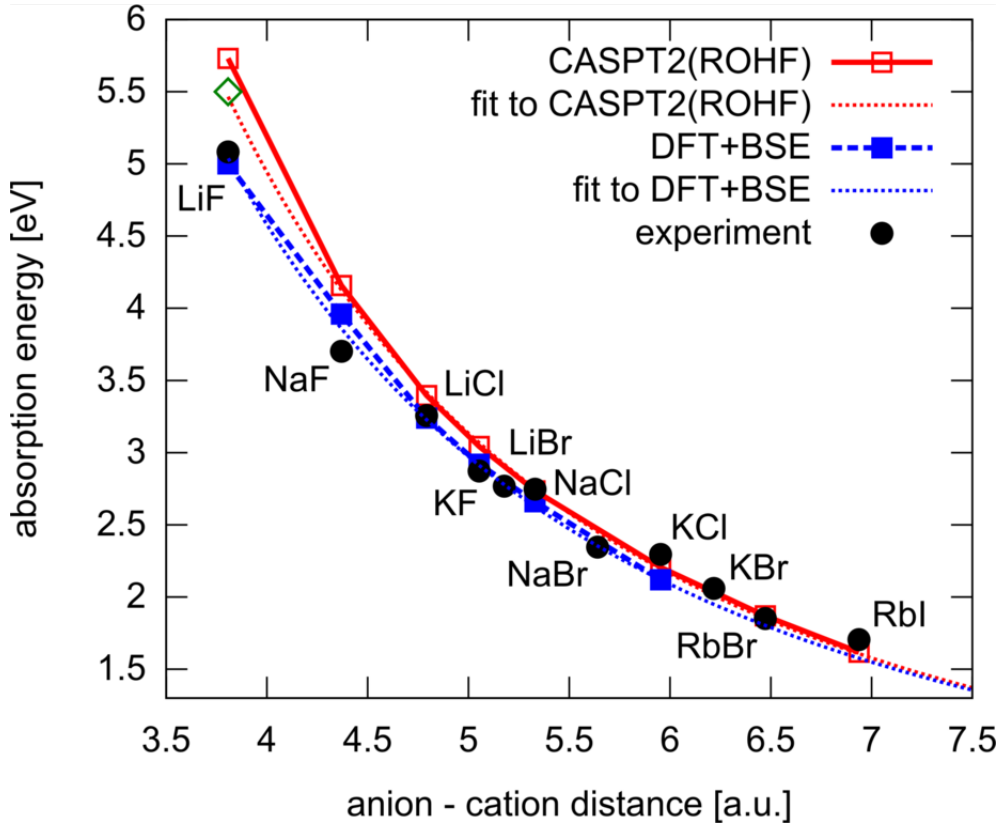


Figure 19: F-center absorption energies of “stretched” LiF as a function of the anion-cation distance. The solid red line shows quantum chemistry results, the dashed blue line are results from DFT+BSE calculations. The green cross is the converged absorption energy of unrelaxed LiF. Dotted red and blue lines are fits of equation 131 to quantum chemistry and DFT results, respectively. Fits yield a Mollwo–Ivey exponents of  $n_{QC} = 2.04$  and  $n_{DFT} = 1.91$ . Black dots are experimental data.

$|s\rangle$  otherwise the rms values would show a stronger dependence on the ionic species. If this conclusion by Malghani and Smith is true then the spatial extent of the ground state F-center wave function in real materials should show a similar behaviour as the one in stretched LiF shown in figure 20.



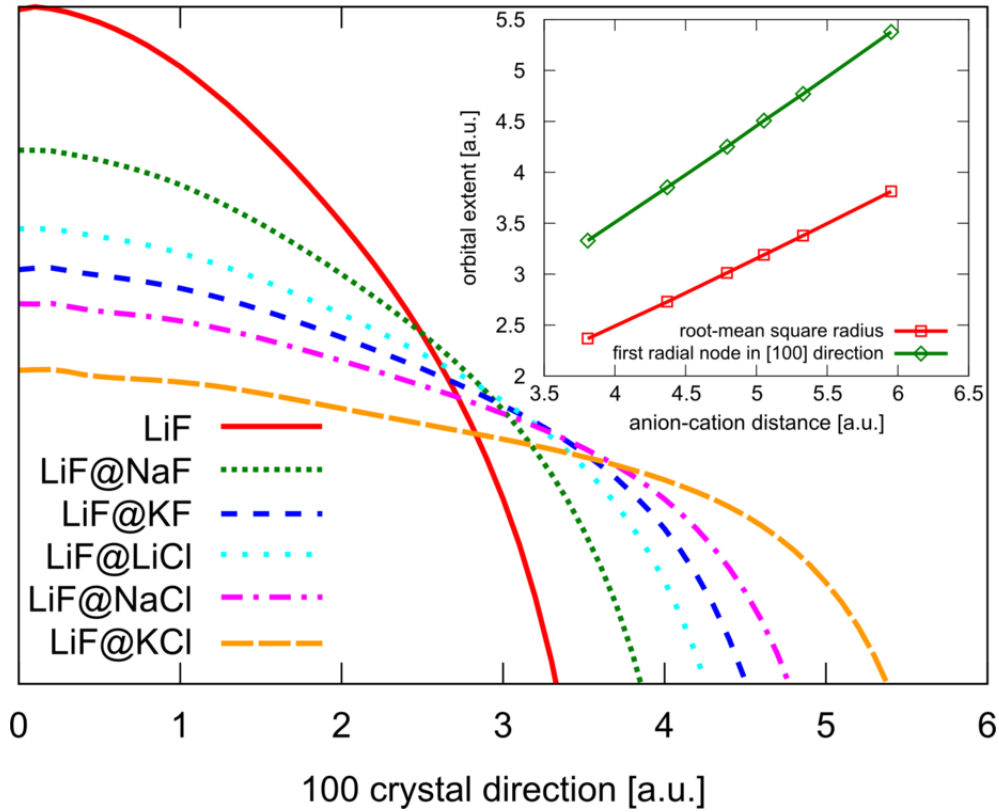


Figure 20: Cut through the ROHF orbital  $|s\rangle$  of the F-center electron in its ground state in “stretched” LiF crystals with lattice constants corresponding to LiF, NaF, KF, LiCl, NaCl, and KCl. For clarity the wave functions are plotted only up to their first radial node. The inset shows the position of the first radial node and the root-mean square radius of  $|s\rangle$  as a function of anion-cation distance.

### 3.5 Ion-size effects

Figure 21 shows the effective Kohn–Sham potential wells the defect electron is bound to for the first three alkali fluorides and chlorides. Please note that they are individually shifted in energy for clarity. The KS potentials clearly separates into two groups with respect to the anion species. Within the group of fluoride (solid lines) and chloride crystals (dashed lines), respectively, all potential wells, independent of the lattice parameter, have a similar depth and similar slope of the walls. This separation also becomes manifest in the Kohn-Sham energies of the s-type defect orbitals indicated by the horizontal lines in the potential wells in figure 21. The obviously non-continuous change of the depth and the slopes of the KS potential wells suggests that the idea of continuously increasing defect wave functions by Malghani and Smith [129] is incomplete. A similar result in the spatial extent of the F-center ground state ROHF orbital obtained in the quantum chemistry calculations is found. The first radial node in the [100] direction  $r_0$ , the rms radii  $\langle s|r^2|s\rangle^{1/2}$  as well as cuts through the s-type defect orbitals are plotted in fig. 22 for the F-center in the different alkali halides. For clarity we cut off the orbitals after their first radial node. Depending on the lattice constant 75 to 90% of the electron are localized within a sphere around the defect with a radius  $r_0$ . The defect orbitals clearly split into two groups according to the anion species, too since the radial nodes for a given anion species almost coincide. We find for fluorides a radial node at  $r_0^F \approx 3.4$  Bohr and for chlorides  $r_0^{Cl} \approx 4.3$  Bohr. In our paper [98] on the F-center in LiF we determine a value for the displacement of the Li cations due to relaxation which is a little below 0.1. Since this displacement is rather small compared to the difference of the radial nodes the separation of fluoride and chloride defect orbitals will not be lifted by relaxing the crystal structure around the defect. In reference [98] we also show a negligible difference between HF defect orbitals and orbitals derived from methods taking into account correlation. Therefore, also correlation effects do not lift the separation. The rms radii follow a similar trend showing a clear difference for fluorides and chlorides. For both anionic species they linearly increase as a function of lattice distance, however, with a different slope and a clear offset between them. Both slopes are smaller than the one for stretched LiF.

A comparison of  $r_0$  and the rms-radii of the ROHF F-center ground-state wave functions in stretched lithium fluoride and in real materials show a strong dependence of the wave function’s spatial extent on the ionic species, i.e., a strong dependence on the ion sizes. The offset between fluorides and chlorides as well as reduced growth of the rms radii in real materials compared to the ones in stretched lithium fluoride suggest that larger ions tend to

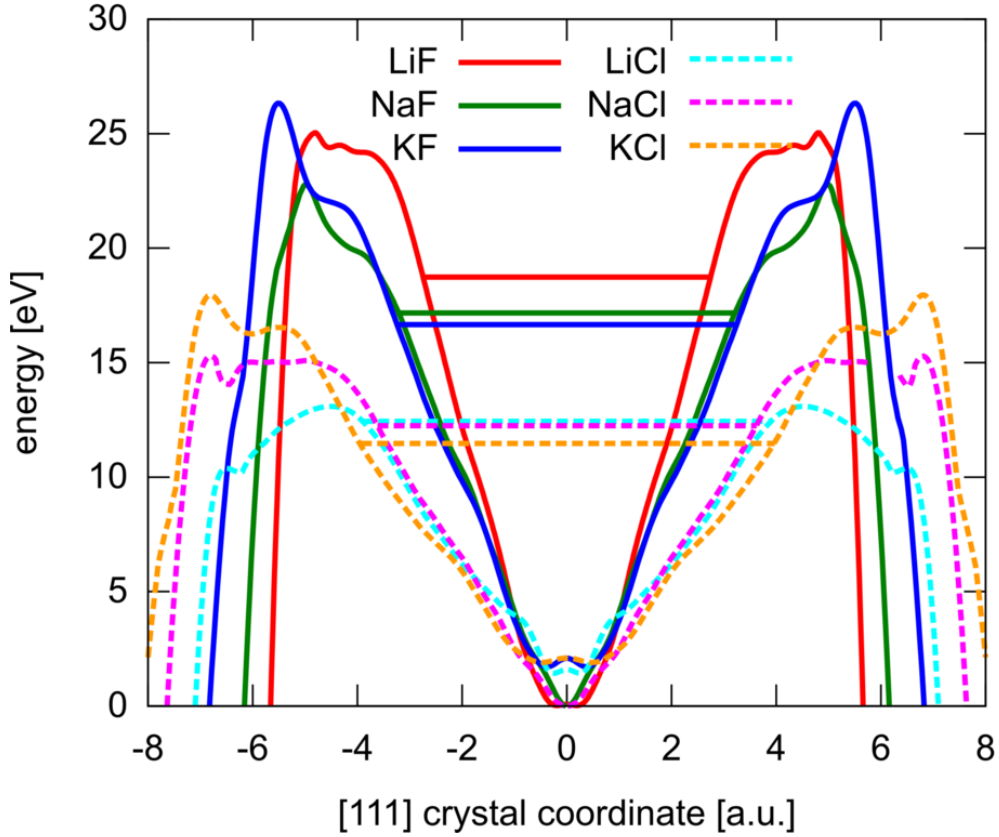


Figure 21: Cut through the effective Kohn–Sham potentials in the F-center defect region in fluoride crystals (solid lines) and chlorides (dashed lines). Horizontal bars are the Kohn–Sham single particle energies of the corresponding ground state, i.e., s-type defect orbitals.

compress the ground-state wave function. A qualitatively similar result was found by Gourary and Adrian [137] who added effects of exchange to their point-ion model. On the ab-initio level ion-size effects can be made visible by comparing the density of the F-center electron  $\rho_{MX}$  of crystals  $MX$  with a fixed lattice constant but different cation and anion species  $M$ ,  $X$ , respectively. Figure 23 shows the differences (a)  $\rho_{NaF} - \rho_{LiF}$  and (b)  $\rho_{LiCl} - \rho_{LiF}$  in a crystal lattice with an anion-cation distance of 5.95 Bohr. Replacing the Li cation by a Na cation (fig. 23 (a)) compresses the defect electron in the vacancy and clearly the compression is induced by the change of the cation size since it solely occurs along the [100] and the [010] crystal direction, the x- and y-axis in figure 23 (a), respectively. The direction of the compression changes when the F anion is replaced by a Cl anion (fig. 23 (b)). It occurs along the [110] and [1 - 10] crystal axis, the two diagonals in figure 23 (b)

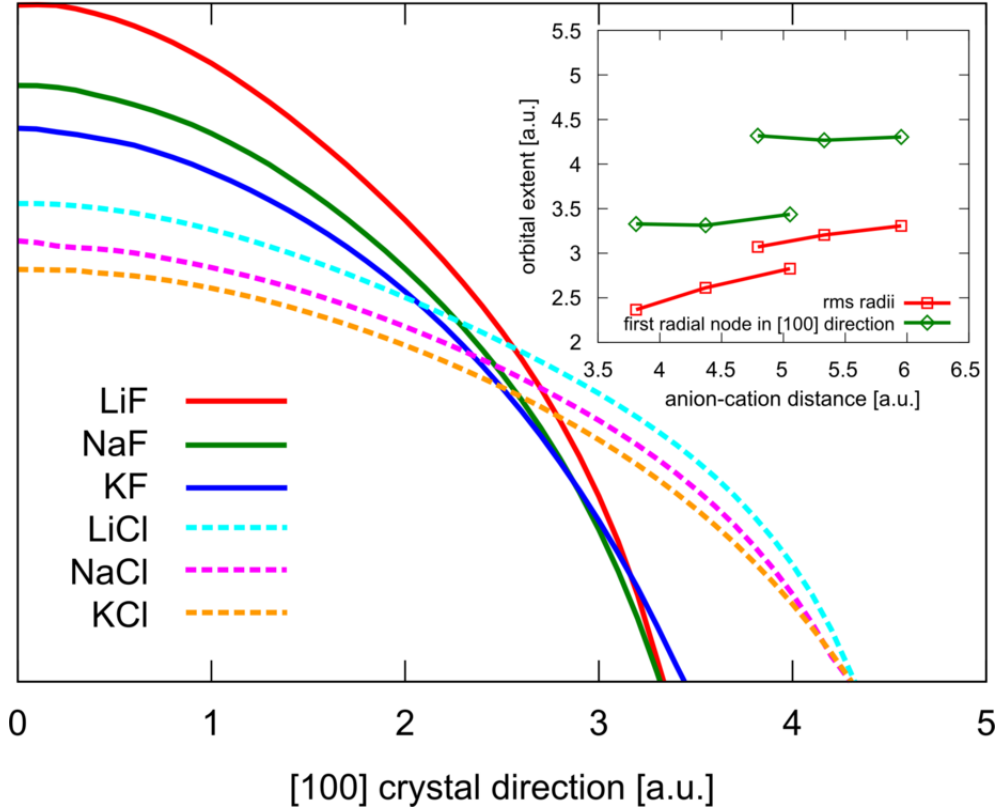


Figure 22: Cut through the ROHF orbital  $|s\rangle$  of the F-center electron in its ground state in various alkali-halide crystals. For clarity the wave functions are plotted only up to their first radial node. The inset shows the position of the first radial node and the root-mean square radius of  $|s\rangle$  as a function of anion-cation distance.

and, additionally, it is weaker than for the exchange of cations. These findings are in contradiction to the results of Smith and Inokuti [138]. They used defect wave functions  $|s\rangle$  from point ion models and studied ion-size effects by orthogonalization of  $|s\rangle$  to the neighboring ion cores. For NaCl and RbF, crystals with a similar lattice constant, they determined the extent, the root-mean square radius, of the F-center in RbF to be larger than the one in NaCl and concluded that F-centers with larger cation neighbors are greater than those with smaller neighbors. In a lattice with an anion-cation distance of 5.95 Bohr we find rms radii of 4.14, 4.18, 4.04 and 4.04 Bohr for  $|s\rangle$  in LiF, LiCl, NaF, and NaCl, respectively, i.e. smaller radii for the F-centers with the larger nearest-neighbor cation and almost equal radii for F-centers with the same nearest neighbor.

The constant value of  $r_0$  for a given anion species can be explained in terms of

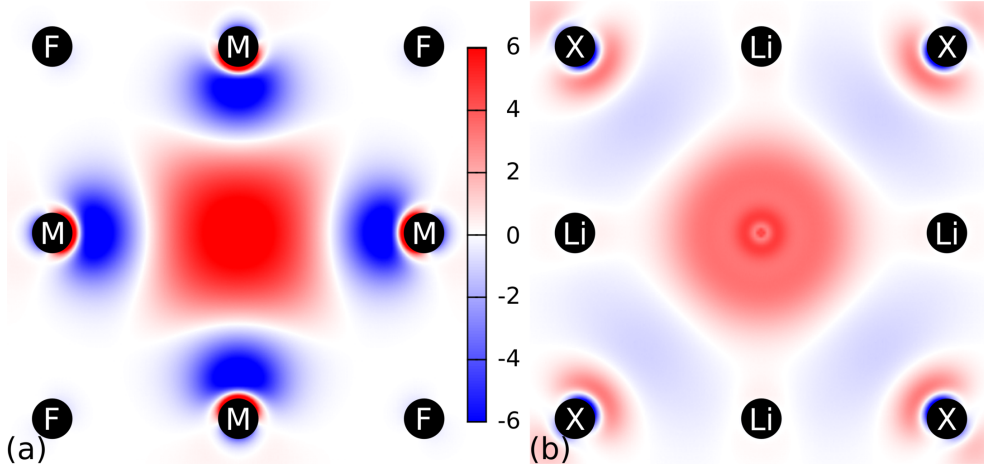


Figure 23: Defect-electron density differences in  $10^{-4}/\text{Bohr}^3$  for the F-center in (a) NaF and LiF ( $\rho_{\text{NaF}} - \rho_{\text{LiF}}$ ) and (b) in LiCl and LiF ( $\rho_{\text{LiCl}} - \rho_{\text{LiF}}$ ) for a constant anion-cation distance of 5.95 Bohr. Replacing Li and F ions with the larger Na and Cl ions, respectively, compresses the defect-electron density in the anion vacancy.

the well-known model of effective ionic radii in crystals [139]. It sets constant radii for anions and cations in, e.g., alkali-halide crystals independent of the crystal composition. Adding up the effective radii  $r_M$  and  $r_X$  of the cation M and the anion X, respectively, gives then a good approximation for the anion-cation distance  $a_{MX}$  of the crystal  $MX$ . According to this thought the F-center electron should have the same spatial extent within all the fluorides and within all chlorides which is in qualitative agreement with figure 22. Using the effective ionic radii model, we find even quantitative agreement when we estimate the correction to  $r_0$  in stretched LiF when, instead of Li, the real cation is used. The second column in table 4 lists values of  $r_0$  in stretched LiF at a lattice constant equal to the one of the crystal Y indicated in the first column. If Li in stretched LiF (with the lattice constant of the MY crystal) is exchanged by M,  $r_0$  should shrink by the difference  $r_M - r_{\text{Li}}$ , where  $r_M$  and  $r_{\text{Li}}$  are the effective ionic radii of M and Li, respectively. The effective radii  $r_R$  are listed in column three in table 4 and the corrected values for the radial node  $r_0 - (r_R - r_{\text{Li}})$  are shown in column four. After applying the correction to  $r_0$  of stretched LiF all the radial nodes of the fluorides coincide as well as the ones of the chlorides at exactly the value found in real materials in fig. 22. This perfect match qualifies the effective-radii model for estimating the extent of the defect electron wave function and it suggests the following conclusions. Along the [100] direction the extent of the ground state defect

Table 4: Correction of the radial node of the defect wave function of stretched LiF due to the effective size of real, i.e., larger cation neighbors. The second column lists the position of the first radial node along the [100] crystal direction of the ground-state defect wave function in stretched LiF  $r_0^{LiF@MX}$  with the lattice constant of the material  $MX$ . The third column shows the effective cation radii [139]  $r_M$  and the fourth column gives the corrected position of the radial node  $r_0^{LiF@MX} - \Delta r_M = r_0^{LiF@MX} - (r_M - r_{Li})$ . All distances are given in Bohr.

Crystal $MX$	$r_0^{LiF@MX}$	$r_M$	$r_0^{LiF@MX} - (r_M - r_{Li})$
LiF	3.33	1.70	3.33
NaF	3.85	2.19	3.36
KF	4.51	2.87	3.34
LiCl	4.25	1.70	4.25
NaCl	4.77	2.19	4.28
KCl	5.38	2.87	4.21

wave function in real materials is constant for a constant anionic species because the increase of the vacancy due to growing anion-cation distance when going, e.g., from LiF to NaF is completely compensated for by the increase of the cation size. When exchanging the anion at constant cation, going from, e.g., LiF to LiCl, the defect-wave function increases along the [100] direction exactly by twice the difference in anion radii between  $Cl^-$  and  $F^-$ . This is reflected in our results by the difference of the  $r_0$  values between fluorides and chlorides which is 0.9 Bohr and almost perfectly matches the difference in anion-cation distance between crystals with the same cation but different anions  $F^-$  and  $Cl^-$ . Along the [110] and [111] crystal axis, the directions towards the second-nearest neighbor anion and the third-nearest neighbor cation, the situation is different. In both directions the increasing ion size can not completely compensate for the increasing lattice parameter since the distance between the defect electron and the second and third-nearest neighbors scale with  $\sqrt{2}a_{MX}$  and  $\sqrt{3}a_{MX}$  along the [110] and [111] direction, respectively.

### 3.6 Absorption energies in alkali halides

The analysis of the defect densities differences in fig. 23 and the behaviour of the radial nodes  $r_0$  of the defect electron wave functions clearly show the tendency of larger ions to compress the defect electron within the vacancy region. Since alkali-halide crystals with larger lattice constants obviously feature larger ions than crystals with a smaller lattice constant the compression by the larger ions inhibits a continuous growth of the extent of the defect wave function with the anion-cation distance. Since via equation 132

$$E_{abs} \approx \frac{3\hbar^2}{2m_e} \frac{1}{\langle s|r^2|s \rangle}, \quad (133)$$

the absorption energies are indirectly proportional to the mean-square radius of the F-center ground-state wave function we expect for the Mollwo–Ivey relation an exponent below 2 and this is indeed what is found in experiment and in our calculations.

Figure 24 shows the experimental absorption energies of the F-center in several materials (black circles) together with the energies obtained from embedded quantum-chemistry cluster calculations (solid red line and green diamonds) and from DFT calculations (dashed blue line). The Mollwo–Ivey relation with parameters  $C = 17.3$  eV and  $n = 1.81$  taken from section 3 is indicated by the dotted pink line. In general we find good agreement with experimental values. The offset between experiment and the quantum chemistry results (solid red line) can be understood in terms of incomplete convergence with respect to cluster and basis-set size due to the large computational effort for crystals containing elements larger than lithium and fluoride. In the case of LiF we find in reference [98] a reduction of the absorption energy by  $\sim 0.5$  eV by using geometry optimization, larger cluster sizes and an extrapolation to the converged basis set limit. Fully converged (ROHF)-CASPT2 results are indicated by green open diamonds and show that the reduction of the absorption energy due to complete convergence and a relaxed lattice structure lies in the range of  $\sim 10\%$ . Since all data points obtained by quantum chemistry are treated on the same level of convergence we expect to get reasonable results for trends such as the Mollwo–Ivey relation. The issue of convergence is, at least for the basis set size, absent in the DFT calculations which partly explains the better agreement with experimental results.

We extract the Mollwo–Ivey parameter  $n$  by fitting our data with  $C/a^n$  and obtain  $n_{QC} = 1.70 \pm 0.12$  and  $n_{DFT} = 1.79 \pm 0.13$  from Quantum Chemistry and post-DFT data, respectively. These values are quite close to experiment,  $n_{exp} = 1.81 \pm 0.10$  and lie clearly below 2. In the most recent

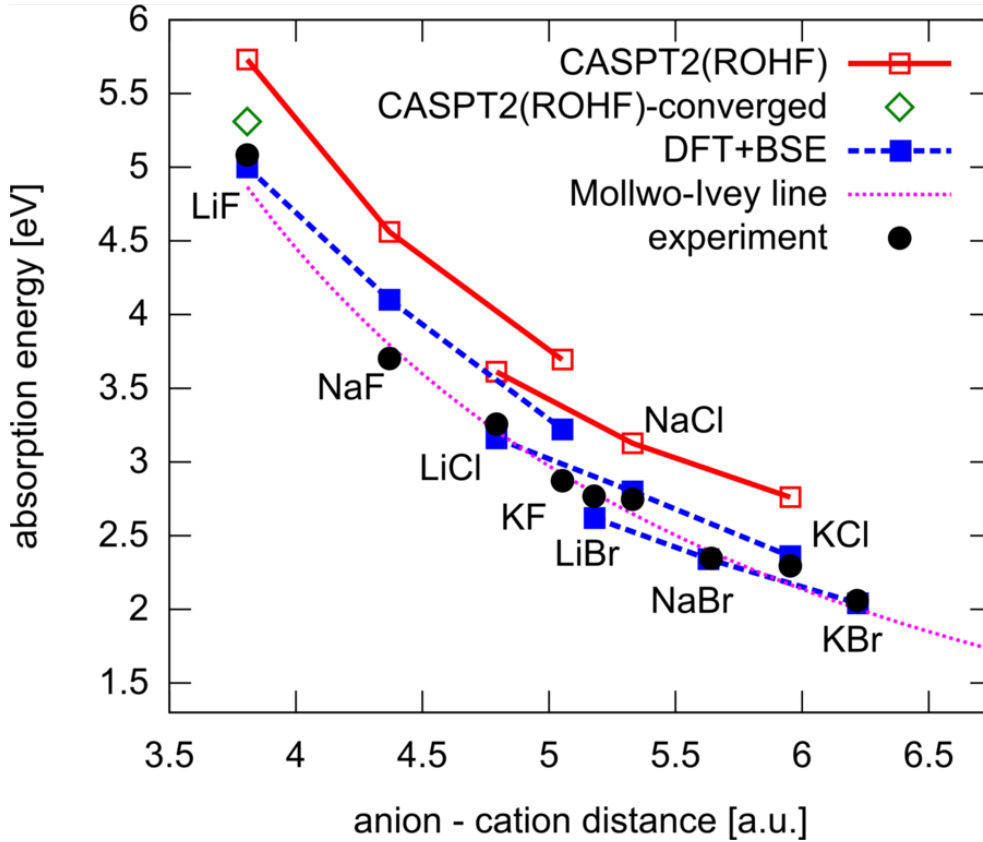


Figure 24: F-center absorption energies of various alkali-halide crystals as a function of the anion-cation distance. Red solid line and green crosses are quantum chemistry results, the dashed blue line are results from DFT calculations, the pink dotted line is the Mollwo–Ivey relation with parameters  $C = 17.3$  eV and  $n = 1.81$  taken from section 3 and the black dots are experimental data<sup>89</sup>.

literature [129, 133, 136, 140] analyzing the physical root of the Mollwo–Ivey exponent there seems to be a consensus on the role of the ion-size effects making them responsible only for deviations from the Mollwo–Ivey relation scaling with  $1/a^{1.81}$ . Based on our ab-initio analysis, however, ion-size effects seem to be the dominant reason why an experimental Mollwo–Ivey exponent below 2 is found. If not for ion size effects, as realized in the ab-initio calculations of stretched LiF, we find a Mollwo–Ivey exponent of  $\sim 2$  like in a three-dimensional potential well ("particle in a box"-like behavior).

In figure 24 the F-center absorption energies for crystals with the same anionic species are connected by straight lines. Following these lines from left to right corresponds to increasing the lattice constant due to larger cations



(nearest-neighbor of the defect electron) while keeping the size of the anions (second-nearest neighbor) constant. Fitting the data separately for every anion with a Mollwo–Ivey type relation leads to an exponent clearly below the global experimental or theoretical value for the Mollwo–Ivey exponent. This reduced decrease can be understood qualitatively in terms of ion-size effects again via the effective ion-radii model.  $F$ -center defect wave functions in, e.g., fluorides have an almost constant extent along directions  $([100],[010],[001])$  pointing towards the six nearest neighbor cations. Along the  $[111]$  direction, the direction towards the third-nearest neighbor cation, the wave functions' extent is not constant but its growth is also, to some extent, compensated for by the increasing cation size. Only along the  $[110]$  direction, towards the second-nearest neighbor  $F^-$  ion, the growth of the wave function is not hindered by increasing ion sizes. In sum this leads to a somewhat flatter decrease of the absorption energies with the anion-cation distance since the smallest constriction due to the nearest neighbors does not increase for a constant anion species. Changing from, e.g., fluorides to chlorides sets a new, larger value for the smallest constriction leading to the offset between the lines connecting the absorption energies of fluoride and chloride crystals. The choice of how to connect the data points is, of course, arbitrary and can be changed by connecting the ab-initio  $F$ -center absorption energies with lines belonging to crystals with the same cation. From left to right these lines correspond to increasing lattice constants due to larger anions (second-nearest neighbor) while the size of the cations (nearest-neighbor) is kept constant. A fit to these line sections results in an exponent larger than the global experimental and theoretical Mollwo–Ivey exponent. When the cation species is kept constant a steeper decrease is found because the narrowest constriction of the vacancy due to the nearest-neighbor cations increases continuously as well as the  $[111]$  direction towards the third-nearest neighbors. Only along the  $[110]$  direction increasing anion sizes partly dampen the growth of the defect wave function. The Mollwo–Ivey relation, however, is a fit to all experimental absorption energies irrespective of anion and cation species resulting in a “mean” Mollwo–Ivey exponent of 1.81.

Smakula [133,141] followed a similar route fitting separate Mollwo–Ivey relations to the experimental  $F$ -center absorption energies of crystals with constant cations resulting in more accurate fits. However, such an analysis of our data and a comparison of ion-specific exponents to experiment is not really meaningful, since the experimental data show only a very small dependence on the ionic species. Only the absorption energies in chloride crystals seem to systematically lie above the Mollwo–Ivey line and decay with a somewhat smaller exponent. This discrepancy may have its roots in the relatively large error bar of the experimental data due to the large full width at half

maximum of the F-center absorption lines [105] ranging from 0.16 eV up to 0.61 eV in lithium fluoride. Furthermore, in our calculations we do not include electron-phonon interactions which induce a lowering of the absorption energies. We estimate this downward shift [98] in lithium fluoride to be of the order of 0.1 eV. Since electron-phonon interactions also depend on the size, i.e. the mass of the crystal ions they should diminish the offset between the F-center absorption energies of crystals containing a different anionic species.

### 3.7 Summary and conclusions

In this section we present an ab-initio study of the Mollwo–Ivey relations for  $F$  centers in alkali-halide crystals based on DFT (and post-DFT, many-body perturbation theory methods) and quantum chemistry (post-HF) methods. This part of the work was done in cooperation with Paul Tiwald<sup>5</sup>. The quantum chemistry calculations were all performed by Paul Tiwald. Both the DFT calculations and quantum chemistry calculations were carried in analogy to section 2 and appendix 5.4.

In contrast to earlier interpretations which stress the importance of the Madelung potential we find exchange, i.e. ion-size effects, to be the predominant mechanism forming the potential well within which the defect electron is bound. The sizes of the neighbor ions determine the shape of the defect-electron wave function and are, therefore, responsible for the fractional Mollwo–Ivey exponent of 1.81. If it were not for ion-size effects a Mollwo–Ivey exponent of  $n = 2$  is expected.

We have introduced the model system of scaled LiF in which we can increase the anion-cation distance while keeping ion sizes constant. The  $F$ -center absorption energies in scaled LiF obey a Mollwo–Ivey relation with an exponent of 2 equal to the 3D square-well potential model by Stöckmann [131, 132]. The reduced Mollwo–Ivey exponent for "real" materials suggests neighboring ions compressing the defect electron wave function within the vacancy region. This leads to a reduced growth of the wave function's extent with increasing lattice parameter which, via the Vinti sum rule, is directly connected to the absorption energy. A qualitative picture of this compression is gained by studying ab-initio differences of defect-electron densities in different alkali-halides at a fixed anion-cation distance. A semi-quantitative picture is obtained by examining radial nodes of Hartree–Fock defect electron wave functions the position of which perfectly agree with predictions from the effective ion-radii model.

---

<sup>5</sup>Paul Tiwald, Institute for Theoretical Physics, Vienna University of Technology, Wiedner Hauptstraße 8-10, A-1040 Vienna, Austria

## 4 Adiabatic connection fluctuation dissipation theorem calculations

The correlation energy within the (RPA-)ACFDT is calculated following equation 84

$$E_c^{\text{RPA}} = \int_0^\infty \frac{d\omega}{2\pi} \text{Tr}\{\ln[1 - \chi^{\text{KS}}v] + v\chi^{\text{KS}}\} \quad (134)$$

where  $\chi^{\text{KS}}$  is obtained using equation 41. The calculation of the total energy within the RPA (see also equation 86)

$$E_{\text{tot}} = E_{\text{HF}}[\psi^{\text{KS}}] + E_c^{\text{RPA}}[\chi^{\text{KS}}] \quad (135)$$

consist of three steps:

1. In a preliminary calculation the Kohn–Sham orbitals are calculated using a (semi-)local potential. Since these orbitals are the basis for the RPA calculations, dense  $k$  meshes, a high energy cutoff parameter  $RK_{\text{max}}$  and a large number of conduction states are required for good convergence of the energies.
2. The Hartree–Fock energy is calculated. The Kohn–Sham orbitals are used as a basis and the Hartree–Fock energy is calculated in a single-shot calculation without an update of the orbitals. The Hartree–Fock calculations usually need denser  $k$  meshes than standard DFT calculations to achieve the same accuracy.
3. The RPA correlation energy is calculated within the ACFDT formalism. The response function  $\chi^{\text{KS}}$  is obtained from the Kohn–Sham orbitals and equation 84 is solved to obtain the correlation energy. This energy is then added to the Hartree–Fock energy to obtain the total energy. As in the case of Hartree–Fock the RPA calculations need a denser  $k$  mesh than standard DFT calculations to achieve good accuracy. Additionally the evaluation of  $\chi^{\text{KS}}$  requires a large number of conduction states. Usually all available states within the basis for a given  $RK_{\text{max}}$  are used. The evaluation of the correlation energy also needs a frequency integration up to a maximum frequency (see appendix 5.3). So the integration depends not only on the number of frequency points but also on the value chosen as the maximum frequency.

In our calculations the  $k$  mesh,  $R_{MT}$  and  $RK_{max}$  are always the same in all three steps.

In the following we will show convergence tests for the (RPA-)ACFDT correlation energies. Convergence tests for the Hartree–Fock energies are not provided since regarding the calculation time more or less no limits existed for the investigated compounds and we used very high values for the Hartree–Fock specific parameters. The following parameters have been used (for explanation of these parameters see reference [85]):  $gmax=14$ ,  $lmax=5$ ,  $lmaxv=5$ ,  $tolu=0.0001$ .

All lattice constants and bulk moduli in this chapter are obtained by fitting the calculated total energy vs. lattice constant (or volume) curves to Birch–Murnaghan’s equation of state [142].

## 4.1 Frequency dependency

The correlation energy is calculated as a frequency integral of the response function at imaginary frequencies  $\chi(\omega)$ . Since the integrand  $\text{Tr}\{\ln[1-\chi^{KS}v]+v\chi^{KS}\}$  is more or less a smooth function the integration does not constitute a fundamental problem.

The integrand of the correlation energy with respect to the frequency for the noble gas atoms Ar and Kr and solid C (diamond) is given in figure 25. The correlation energy for the Ar and Kr atom was calculated by placing a single atom in the center of an empty cell with a lattice constant of 15 Bohr and using a single  $k$  point. All functions are quite smooth but at low frequencies the correlation energy shows more structure and an equidistant grid would only converge very slowly. For this we applied a Gauss–Legendre-quadrature scheme on a non-equidistant grid where the integral is of the form (for details see appendix 5.3)

$$I(f) = \int_0^{\omega_{max}} w(x)f(x)dx. \quad (136)$$

The lower limit of the integral is always equal to zero. The upper limit  $\omega_{max}$  has to be chosen for each calculation. For insulators and semiconductors this parameter doesn’t constitute a problem as long as it’s value is chosen above the band gap of the calculated material. Since we didn’t experienced significance of this parameter on the accuracy of the calculations, we will not show convergence tests for this parameter. The total correlation energy with respect to the number of frequency points is given in table 5. For the atoms already 10 frequency points would be sufficient to have a convergence below 0.1 mRyd. In the case of diamond 14 points would be enough to have a convergence below 0.1 mRyd. In the remainder of this work (if not stated

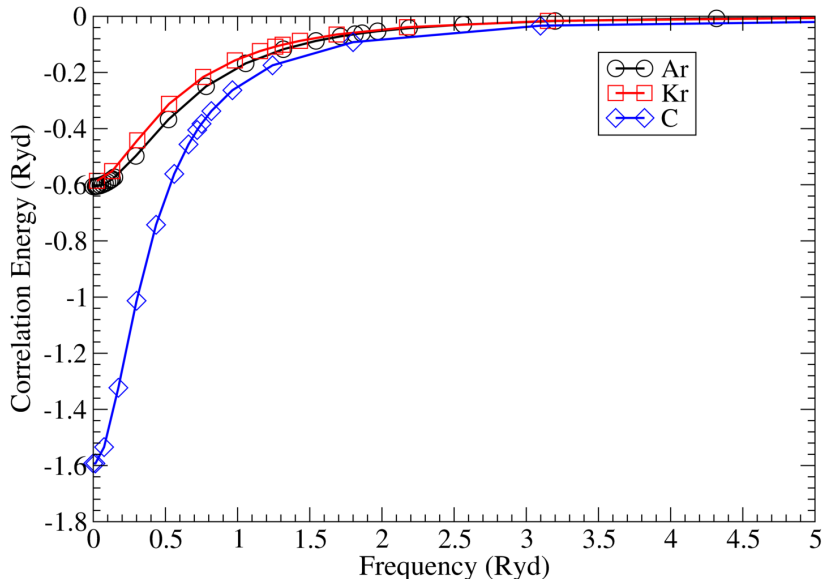


Figure 25: . Integrand of the correlation energy (see equation 134) with respect to the frequency.  $\omega_{max} = 35$ ,  $RK_{max} = 9$ ,  $lm_{max} = 4$  and  $G_{max} = 9$  Ryd were used in the calculations. The correlation energies are only shown for the  $\Gamma$  point.

otherwise) we used 16 points for the frequency integration to be on the save side.

## 4.2 $k$ mesh dependency

Although the  $k$  mesh for insulators represents generally no problem for the (RPA-)ACFDT calculations, we will briefly discuss the behavior of the correlation energy going from small to large  $k$  meshes. The correlation energy with respect to the lattice constant using different  $k$  meshes is shown for diamond in figure 26. The absolute correlation energy converges very slowly with the number of  $k$  points and we would need a very high number of  $k$  points, to converge the absolute value, reaching soon the limits of our computational resources (i.e. by going from a  $k$  mesh of  $4 \times 4 \times 4$  to  $8 \times 8 \times 8$  the computational time is increased by a factor of 10). Since we are mainly interested in the lattice constants and bulk moduli it is sufficient to calculate the relative correlation energies between different volumes. By comparing

Table 5: Calculated correlation energies with respect to the number of frequency points  $N$ .  $\omega_{max} = 35$  Ryd was used in all calculations. All units in mRyd.

$N$	Kr	Ar	diamond
6	-457.460	-554.408	-
8	-457.404	-554.692	-
10	-457.474	-554.982	-987.196
12	-457.480	-554.988	-987.700
14	-457.480	-554.980	-987.886
16	-457.482	-554.982	-987.944
18	-457.482	-554.986	-987.964
20	-457.482	-554.986	-987.974

the slopes in figure 26 it can be seen that the relative energies converge much faster. While a  $k$ -mesh of  $4 \times 4 \times 4$  shows small oscillations, the curve gets smooth for  $6 \times 6 \times 6$ . Also the lattice constant and the bulk modulus are converged for  $6 \times 6 \times 6$  (see table 6), so that a  $k$  mesh of  $6 \times 6 \times 6$  seems sufficient for diamond.

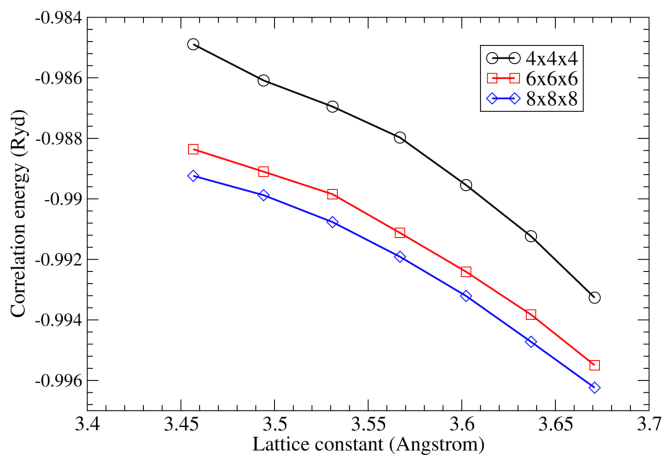


Figure 26: Correlation energy vs. lattice constant for diamond using different  $k$  meshes.  $RK_{max} = 8$ ,  $G_{max} = 4.9$  Bohr $^{-1}$ ,  $lm_{max} = 4$ ,  $\omega_{max} = 35$  Ryd and 16 frequency points were used.

Table 6: Calculated lattice constants  $a_0$  in Å and bulk moduli  $B_0$  in GPa of diamond for different  $k$  meshes.  $RK_{max} = 8$ ,  $G_{max} = 4.9 \text{ Bohr}^{-1}$ ,  $lm_{max} = 4$ ,  $\omega_{max} = 35 \text{ Ryd}$  and 16 frequency points were used. The values obtained using the code VASP [143–146] are taken from reference [59]. The experimental lattice constant and bulk modulus are taken from references [147] and [148], respectively.

$a_0$				$B_0$			
$k$ mesh	PBE	HF	RPA	$k$ mesh	PBE	HF	RPA
$4 \times 4 \times 4$	3.578	3.553	3.572	$4 \times 4 \times 4$	434	510	422
$6 \times 6 \times 6$	3.575	3.550	3.569	$6 \times 6 \times 6$	435	512	443
$8 \times 8 \times 8$	3.575	3.550	3.569	$8 \times 8 \times 8$	435	512	444
VASP		3.572		VASP		442	
experiment		3.567		experiment		443	

### 4.3 basis set dependency

The basis set within the (RPA-)ACFDT calculations mainly depends on three parameters:

- The first parameter is  $RK_{max}$ , the product of the largest reciprocal vector  $K_{max}$  and the smallest atomic radius  $R_{MT}$ , which is already defined for the (semi-)local calculations.
- The second parameter is  $G_{max}$ , the cutoff for the largest reciprocal vector used for the plane wave expansion of the matrix elements in the calculation of the response function ( $e^{i(\mathbf{G}+\mathbf{q})\mathbf{r}}$  in equations 42 and 144).
- The third parameter is  $lm_{max}$ , the largest quantum number of the  $l$  and  $m$  combinations used in the Rayleigh expansion of the plane waves and the wave functions within the muffin-tin spheres (see equations 149 and 150). In principle one could use separate  $lm_{max}$ 's for the Rayleigh expansion and the wave functions within the muffin-tin spheres. Since  $lm_{max}$  converges very fast we used the same value for both.

Figure 27 shows the correlation energy vs. lattice constant curves for varying  $RK_{max}$ ,  $G_{max}$  and  $lm_{max}$ . As for the  $k$  mesh the absolute value of the correlation energy is very hard to converge for  $RK_{max}$  and  $G_{max}$ . The absolute

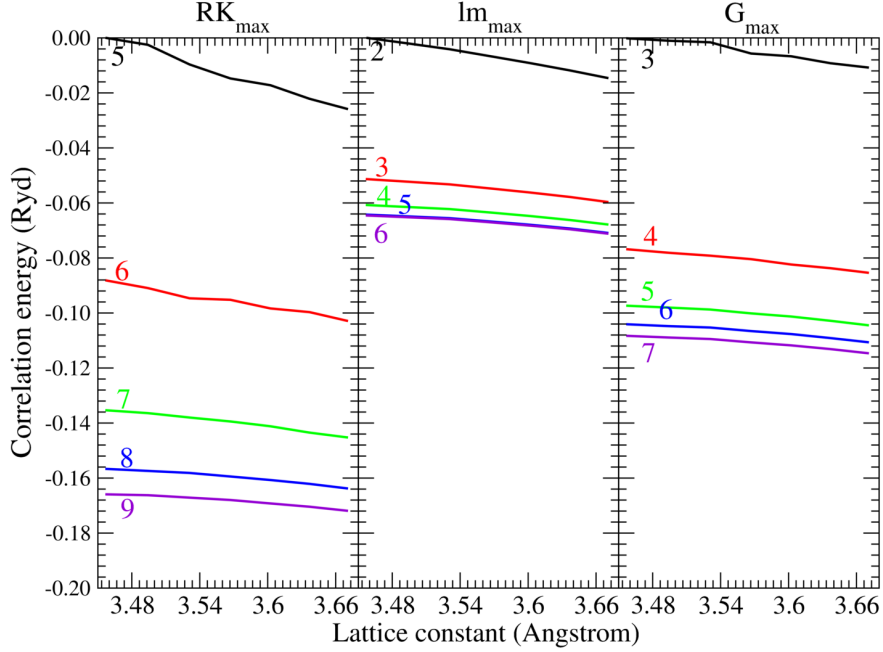


Figure 27: Correlation energy vs. lattice constant for diamond. A  $k$  mesh of  $6 \times 6 \times 6$ ,  $\omega_{max} = 35$  Ryd and 16 frequency points were used in all calculations. Left: Variation of  $RK_{max}$ .  $G_{max} = 4.9$  Bohr $^{-1}$  and  $lm_{max} = 4$  were used. Energies are shifted up by 0.831669 Ryd. Center: Variation of  $lm_{max}$ .  $RK_{max} = 8$  and  $G_{max} = 4.9$  Bohr $^{-1}$  were used. Energies are shifted up by 0.927567 Ryd. Right: Variation of  $G_{max}$ .  $RK_{max} = 8$  and  $lm_{max} = 4$  were used. Energies are shifted up by 0.892315278 Ryd.

correlation converges much faster for  $lm_{max}$  than for the other three parameters. Also the relative correlation energies in figure 28 and the structural data given in table 7 show no significant change for an  $lm_{max}$  larger than 4. Convergence tests for other elements and compounds (MgO, LiF, Si, Ar and Kr) also show that  $lm_{max} = 4$  is save.

Since the calculation time depends very strongly on the size of  $G_{max}$  and in principle an infinitely large  $G_{max}$ , denoted as  $G_{\infty}$  is needed for the exact absolute correlation energies, in reference [59] it is suggested that the correlation energy for  $G_{\infty}$  is approximated by the following expression

$$E_c(G_i) = E_c(G_{\infty}) + \frac{A}{(G_i)^3}. \quad (137)$$



In practice the calculation is carried out by calculating the correlation energy for a series of decreasing cutoffs for  $G_{max}$  denoted as  $G_i$  (usually 5 to 8 steps with a decrease of 2 to 5 percent per step) and extrapolated to infinity by using equation 137. Figure 29 shows the correlation energies for different  $G_{max}$ . The correlation energy for  $G_\infty$  (denoted as  $G_{extrapolated}$  in figure 29) was calculated for an initial  $G_{max}$  of 5 Bohr<sup>-1</sup>, 6 reduction steps and a reduction of 2 percent per step. The  $1/G_{max}^3$  behaviour of the correlation is plotted in figure 30. We can see that this behaviour is more or less only fulfilled for intermediate values of  $G_{max}$ . Since the extrapolation scheme introduces oscillations in the correlation energy vs. lattice constant curves in figure 29 we will not use this scheme in the remainder of this work. Actually the relative correlation energy with respect to the volume seems to converge quite well in figure 29 for 5 Bohr<sup>-1</sup> which is approximately 85 percent of  $K_{max} = 5.76$  Bohr<sup>-1</sup> (from  $RK_{max} = 8$  with,  $RK_{max} = R_{MT}K_{max}$  and  $R_{MT} = 1.39$  Bohr for diamond). This is in good agreement with reference [149] which suggests that  $G_{max}$  should be 75 to 90 percent of  $K_{max}$  to obtain a balanced basis set. Since  $lm_{max}$  and  $G_{max}$  can be fixed to

Table 7: Calculated lattice constants  $a_0$  in Å and bulk moduli  $B_0$  in GPa of diamond for different  $G_{max}$  and  $lm_{max}$ .  $RK_{max} = 8$ ,  $k$  mesh of  $6 \times 6 \times 6$ ,  $\omega_{max} = 35$  Ryd and 16 frequency points have been used. In the case of varying  $G_{max}$   $lm_{max} = 4$  has been used. For varying  $lm_{max}$   $G_{max} = 4.9$  Bohr<sup>-1</sup> was used. Units for  $G_{max}$  are given in Bohr<sup>-1</sup>. The values obtained using the code VASP [143–146] are taken from reference [59]. The experimental lattice constant and bulk modulus are taken from references [147] and [148], respectively.

$G_{max}$	$a_0$	$B_0$	$lm_{max}$	$a_0$	$B_0$
3	3.588	492	2	3.591	426
4	3.573	456	3	3.573	441
5	3.569	442	4	3.569	444
6	3.567	443	5	3.568	445
7	3.567	444	6	3.568	445
VASP	3.572	442	VASP	3.572	442
experiment	3.567	443	experiment	3.567	443

$lm_{max} = 4$  and  $0.75K_{max} \leq G_{max} \leq 0.90K_{max}$  the main parameter for the quality of the basis set to converge is  $RK_{max}$ . The correlation energies vs lattice constants for different values of  $RK_{max}$  are plotted in figure 31 for

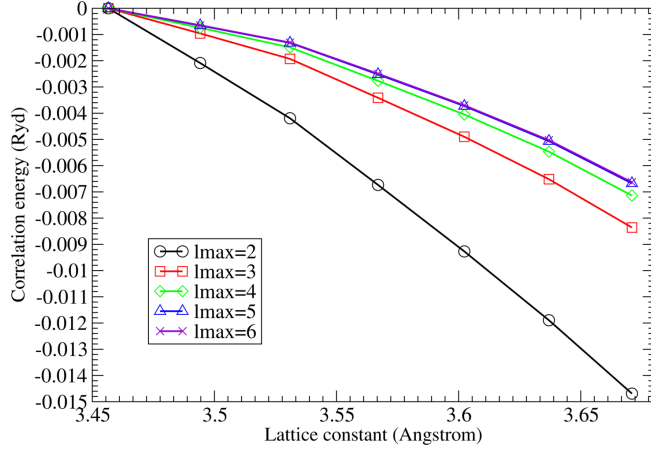


Figure 28: Relative correlation energy vs. lattice constant for diamond using different values for  $l_{max}$ . All curves are relatively shifted to zero by the energy of the smallest lattice constant. A  $k$  mesh of  $6 \times 6 \times 6$ ,  $RK_{max} = 8$ ,  $G_{max} = 4.9$  Ryd and  $\omega_{max} = 35$  Ryd and 16 frequency points were used.

diamond. The energies for a given volume are shifted relative to zero by the value of the correlation energy for the smallest volume. For small  $RK_{max}$  the correlation energy curves show strong oscillations which disappear for higher  $RK_{max}$ . This is a similar behavior observed also in (semi-)local and Hartree–Fock calculations, due to the incomplete basis set. Actually the calculated (RPA-)ACFDT lattice constants and bulk moduli converge similarly with respect to  $RK_{max}$  as the ones obtained from PBE and Hartree–Fock (see table 8).

Table 8: Calculated lattice constants  $a_0$  in Å and bulk moduli  $B_0$  in GPa of diamond for different  $RK_{max}$ . A  $k$  mesh of  $6 \times 6 \times 6$ ,  $lm_{max} = 4$ ,  $G_{max} = 4.9 \text{ Bohr}^{-1}$ ,  $\omega_{max} = 35 \text{ Ryd}$  and 16 frequency points have been used. The values obtained using the code VASP [143–146] are taken from reference [59]. The experimental lattice constant and bulk modulus are taken from references [147] and [148], respectively.

$a_0$				$B_0$			
$RK_{max}$	PBE	HF	RPA	$RK_{max}$	PBE	HF	RPA
5	3.575	3.550	3.611	5	494	536	633
6	3.574	3.550	3.560	6	441	526	445
7	3.575	3.550	3.569	7	435	512	443
8	3.575	3.550	3.569	8	435	512	444
9	3.575	3.550	3.567	9	435	512	445
VASP		3.572		VASP		442	
experiment		3.567		experiment		443	

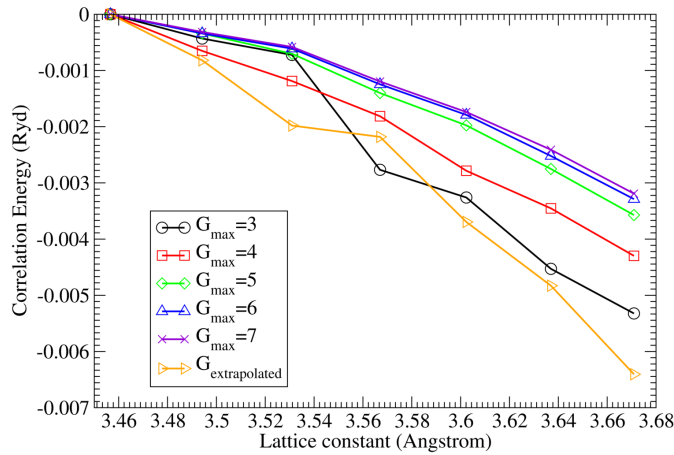


Figure 29: Relative correlation energy vs. lattice constant for diamond using different values for  $G_{max}$ . All curves are relatively shifted to zero by the energy of the smallest lattice constant. A  $k$  mesh of  $6 \times 6 \times 6$ ,  $RK_{max} = 8$ ,  $lm_{max} = 4$ ,  $RK_{max} = 8$ ,  $G_{max} = 4.9 \text{ Bohr}^{-1}$ ,  $\omega_{max} = 35 \text{ Ryd}$  and 16 frequency points were used.

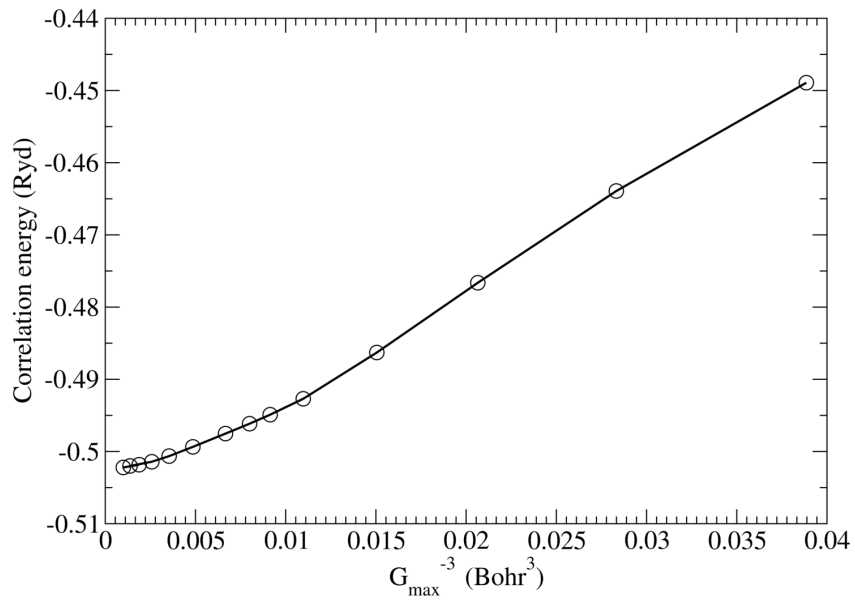


Figure 30: Correlation energy vs.  $G_{\max}^{-3}$  for diamond. The experimental lattice constant of  $3.572 \text{ \AA}$  was used in the calculations. A  $k$  mesh of  $6 \times 6 \times 6$ ,  $RK_{\max} = 8$ ,  $lm_{\max} = 4$ ,  $\omega_{\max} = 35$  Ryd and 16 frequency points were used.

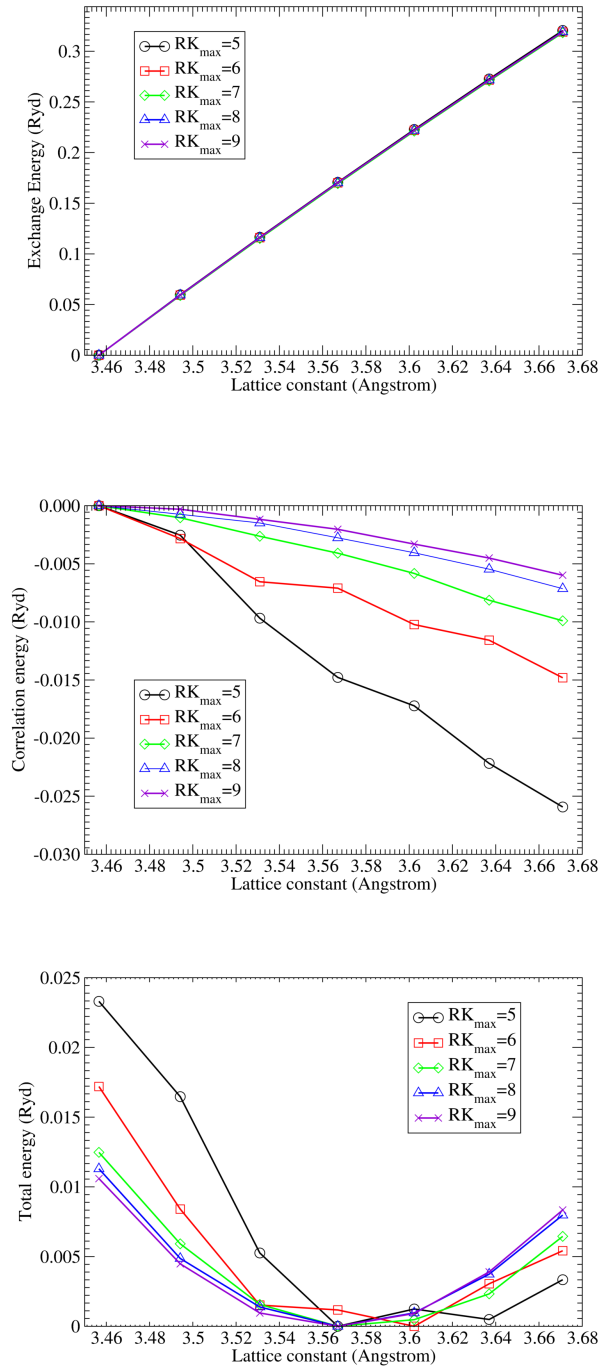


Figure 31: Relative exchange energy, relative correlation energy and total energy vs. lattice constant for diamond using different values for  $RK_{max}$ . All curves for the exchange and correlation energies are relatively shifted to zero by the energy of the smallest lattice constant. A  $k$  mesh of  $6 \times 6 \times 6$ ,  $lm_{max} = 4$  and  $G_{max} = 4.9$  Ryd,  $\omega_{max} = 35$  Ryd and 16 points for the frequency integration were used.

## 4.4 ACFDT calculations for solids

In this chapter we show the calculated lattice constants and bulk moduli for selected solids and compare them to results [59, 150] obtained from VASP [143–146] and from experiment. A comparison of the correlation energies for selected cases to available data from VASP is also given in this section.

The investigated solids together with the most important calculational parameters are listed in table 9. The calculated lattice constants and bulk moduli are given in tables 10 and 11, respectively. The tables compare the results for different levels of treatment for exchange and correlation (PBE, Hartree–Fock, and RPA). In most of the cases we have a close agreement with VASP for the PBE and Hartree–Fock results. The discrepancy for the Hartree–Fock lattice constant for Si is explained by the fact that no 2s and 2p semi-core states were used in the pseudo-potential configuration of the valence electrons in reference [59] (there is a second calculation available in reference [59] including 2s and 2p states in the valence which agrees very well with our Hartree–Fock calculations).

A very good agreement between our (RPA-)ACFDT result, the results obtained from VASP and experiment is present for diamond. Although the noble gas solids are very hard to converge since the energy vs. lattice constant curves have a very shallow minimum a nice agreement is found for the lattice constants and bulk moduli for solid Ar and Kr between our results and VASP. The excellent agreement of the exchange and (RPA-)ACFDT correlation energies for Kr with VASP is shown in figure 32. However, with the exception of C, Ar and Kr we find in general a poor agreement with VASP for the (RPA-)ACFDT lattice constants and bulk moduli, which we account to the different steepness of the slopes for the correlation energies with respect to the lattice constants, since the direction of the corrections is correct but the magnitude is different (compare the difference between HF and RPA lattice constants in table 10). The correlation energy with respect to the lattice constant obtained with WIEN2k and VASP is plotted for Si in figure 33. It is clearly visible that the VASP calculations have a slope that is approximately by a factor of two larger than in our calculations, leading to larger corrections for the lattice constant in table 10. We believe that the VASP results are calculationally intact. In all of our calculations we neglect core to conduction band transitions in the calculation of the response function, while we calculate the the Hartree–Fock exchange between core-valence and core-core states too. Possible important contributions to the correlation energy and counteracting effects of exchange could be missing when the core to conduction band transitions are missing in the calculation of the response

function. This could be the case for heavier elements such as Si and MgO. The inclusion of core states is not straight forward and needs sophisticated methods to be able to converge the results [149]. The discrepancy for LiF cannot be described with the missing core states, since all electrons are considered in the calculation of this material. Another explanation might be, that the basis sets are not well suited for the excited states. The FLAPW method is known to be good for the ground state but in many cases the wave functions in the excited states are not well described within the spheres around the atoms. To solve this problem an extension of the basis set would be needed such as in reference [149] for the OEP method. Nevertheless we cannot exclude possible errors in our code.

Table 9: Calculational parameters of the calculated solids.  $N_{freq}$  is the number of points for the frequency integration. The units for  $G_{max}$ ,  $R_{MT}$  and  $\omega_{max}$  are in Bohr<sup>-1</sup>, Bohr and Ryd, respectively.

	$RK_{max}$	$k$ mesh	$G_{max}$	$lm_{max}$	$N_{freq}$	$\omega_{max}$	$R_{MT}$
C	8.0	$8 \times 8 \times 8$	4.9	4	20	35	1.39
Si	9.0	$8 \times 8 \times 8$	4.9	5	16	35	2.10
LiH	10.0	$8 \times 8 \times 8$	5.0	4	16	35	1.70
LiF	9.8	$8 \times 8 \times 8$	4.9	5	16	35	1.77
MgO	9.0	$8 \times 8 \times 8$	5.0	6	16	35	1.90
Ar	9.8	$8 \times 8 \times 8$	9.0	4	16	35	2.30
Kr	9.8	$6 \times 6 \times 6$	8.0	4	16	35	2.50

Table 10: Calculated lattice constants in Å for different solids. The values [59, 150] obtained using the code VASP [143–146] are given in parenthesis. The experimental values are taken from the following references: LiH [151]. Ar, Kr [152]. LiF, MgO [153]. C, Si [147].

	PBE	HF	RPA	EXP
C	3.575(3.569)	3.550(3.540)	3.569(3.572)	3.567
Si	5.476(5.466)	5.499(5.482)	5.483(5.431)	5.430
LiH	4.007	4.124	4.095	4.084
LiF	4.074(4.069)	4.001(3.991)	4.066(3.998)	4.010
MgO	4.260(4.259)	4.178(4.173)	4.289(4.225)	4.207
Ar	5.961(6.0)	–	5.232(5.3)	5.23
Kr	6.413(6.4)	–	5.693(5.7)	5.61

Table 11: Calculated bulk moduli in GPa for different solids. The values [59, 150] obtained using the code VASP [143–146] are given in parenthesis. Experimental values for LiH, C, Si, LiF and MgO are taken from references [154], [148], [153], [155] and [156], respectively.

	PBE	HF	ACFDT	EXP
C	435(434)	511(512)	444(442)	443
Si	89(89)	107(108)	99(99)	99.2
LiH	36	32	29	33
LiF	67(68)	81(80)	69(76)	69.8
MgO	150(149)	195(196)	156(168)	165



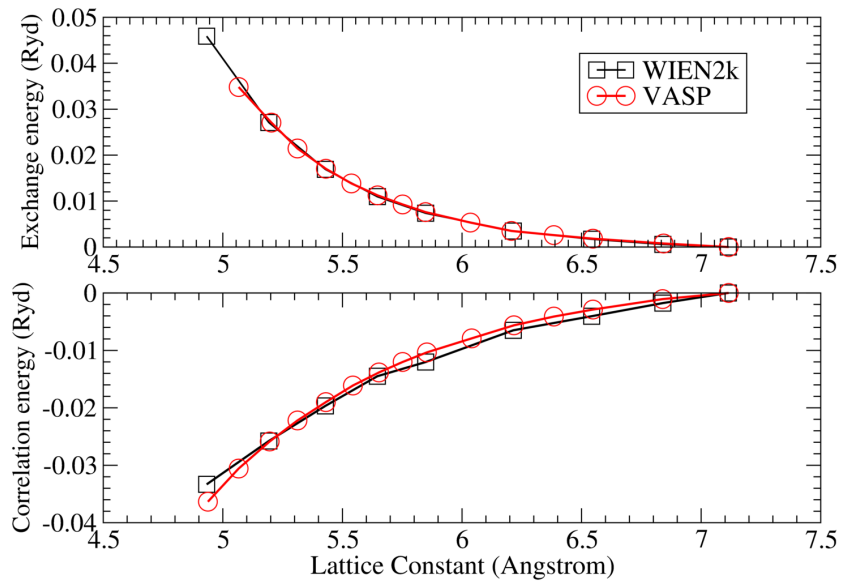


Figure 32: Comparison of the exchange energy and the correlation energies for solid Kr between WIEN2k and VASP. The VASP results were taken from reference [59]. Both calculations used the wave functions from LDA. The correlation energies for the largest volumes are arbitrarily set to zero. A  $k$  mesh of  $4 \times 4 \times 4$ ,  $RK_{max} = 8$ ,  $lm_{max} = 4$ ,  $G_{max} = 8 \text{ Bohr}^{-1}$ ,  $\omega_{max} = 35 \text{ Ryd}$  and 16 frequency points were used in the WIEN2k calculations.

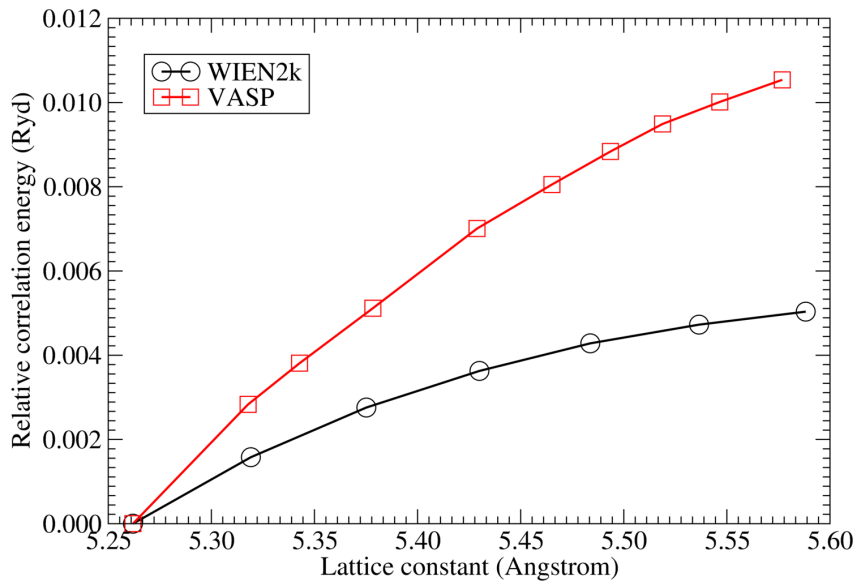


Figure 33: Comparison of the correlation energies for Si between WIEN2k and VASP. The VASP results were taken from reference [59]. Both calculations used the wave functions from PBE. The correlation energy for the smallest volume was set to zero. A  $k$  mesh of  $8 \times 8 \times 8$ ,  $RK_{max} = 9$ ,  $G_{max} = 5 \text{ Bohr}^{-1}$ ,  $lm_{max} = 4$ ,  $\omega_{max} = 35 \text{ Ryd}$  and 16 frequency points were used in the WIEN2k calculations.

## 4.5 Summary and conclusions

This chapter is dedicated to the investigation of the correlation energies calculated using the adiabatic connection dissipation theorem. By adding the correlation energies to the Hartree–Fock energies one can obtain in principle very accurate total energies.

In the main part of this chapter the convergence behavior of the correlation energy for different parameters within the full potential linearized augmented plan-wave method has been investigated. The main parameters which have to be converged most carefully are the Brillouin zone sampling or  $k$  mesh and the energy cutoff parameter  $RK_{max}$  the product of the largest reciprocal vector and the smallest atomic radius. Our calculations for diamond show that a  $k$  mesh of  $6 \times 6 \times 6$  and  $RK_{max} = 8$  is enough for good convergence. Parameters such as  $G_{max}$ , the cutoff for the largest reciprocal vector used for the plane wave expansion of the matrix elements in the calculation of the response function and  $lm_{max}$ , the largest quantum number of the  $l$  and  $m$  combinations used in the Rayleigh expansion of the plane waves and the wave functions within the muffin-tin spheres can be chosen with lesser care. Our calculations showed that  $G_{max} = 5 \text{ Bohr}^{-1}$  and  $lm_{max} = 4$  are quite save values.

In the last part of this chapter we calculated the lattice constant and bulk moduli of several solids using the adiabatic connection dissipation theorem. A good agreement to VASP and experiment is achieved for diamond, Ar and Kr. The adiabatic connection dissipation theorem is very important for solid Ar and Kr since standard DFT methods doesn't include the long range behavior of the important van der Waals interactions in these materials and lead to very nonphysical and wrong results. Sadly for some of the other calculated materials (Si, MgO and LiF) we find bad agreement with VASP and experiment. The disagreements might be due to the possible neglect of core states in the calculation of the correlation energy and to incomplete basis sets for the excited states within the spheres around the atoms. Nevertheless we cannot exclude possible errors in our code.

## 5 Appendix

### 5.1 Hohenberg Kohn theorems

The first Hohenberg–Kohn theorem states that in a system with  $N$  interacting electrons the external potential is uniquely determined (up to an additive constant) by the ground-state electron density and vice-versa. The proof is obtained (*reductio ad absurdum*) in the following way:

Lets assume we have a system with the ground-state density  $\rho_0(\mathbf{r})$ , the external potential  $v_1(\mathbf{r})$ , the Hamiltonian  $\hat{H}_1$  and the wave function  $\psi_1$  leading to the total energy

$$E_1 = \langle \psi_1 | \hat{H}_1 | \psi_1 \rangle = \int d^3r v_1(\mathbf{r}) \rho_0(\mathbf{r}) + \langle \psi_1 | \hat{T} + \hat{U} | \psi_1 \rangle. \quad (138)$$

Also assume that we have a second system

$$E_2 = \langle \psi_2 | \hat{H}_2 | \psi_2 \rangle = \int d^3r v_2(\mathbf{r}) \rho_0(\mathbf{r}) + \langle \psi_2 | \hat{T} + \hat{U} | \psi_2 \rangle \quad (139)$$

leading to the same ground-state density  $\rho_0(\mathbf{r})$ . If we substitute  $\hat{H}_1$  in the first system by  $\hat{H}_2$  we get following inequalities due to the Rayleigh-Ritz principle

$$\begin{aligned} E_1 &< \langle \psi_2 | \hat{H}_1 | \psi_2 \rangle \\ &= \int d^3r v_1(\mathbf{r}) \rho_0(\mathbf{r}) + \langle \psi_2 | \hat{T} + \hat{U} | \psi_2 \rangle \\ &= E_2 + \int d^3r [v_1(\mathbf{r}) - v_2(\mathbf{r})] \rho_0(\mathbf{r}). \end{aligned} \quad (140)$$

Analogously we do the same for system 2

$$\begin{aligned} E_2 &< \langle \psi_1 | \hat{H}_2 | \psi_1 \rangle \\ &= \int d^3r v_2(\mathbf{r}) \rho_0(\mathbf{r}) + \langle \psi_1 | \hat{T} + \hat{U} | \psi_1 \rangle \\ &= E_1 + \int d^3r [v_2(\mathbf{r}) - v_1(\mathbf{r})] \rho_0(\mathbf{r}). \end{aligned} \quad (141)$$

After adding up equations 140 and 141 we arrive at

$$E_1 + E_2 < E_1 + E_2. \quad (142)$$

This is clearly a contradiction leading to the only logical conclusion that our hypothetical assumption where two different external potentials can lead

to the same ground-state electron density is wrong, giving proof that the external potential is uniquely determined by the electron density.

The second Hohenberg–Kohn theorem states that the total energy of the  $N$  electron system is a functional of the electron density and that the ground-state electron density  $\rho_0(\mathbf{r})$  minimizes the total energy of the system leading to the ground-state total energy

$$E_0 = E[\rho_0(\mathbf{r})] = \min E[\rho(\mathbf{r})]. \quad (143)$$

The proof of equation 143 is quite straight forward and will not be shown here. For details see reference [1].

## 5.2 Matrix elements within the LAPW basis

In the following we will give an exact expression for the matrix element

$$M_{m,n}^{\mathbf{G}}(\mathbf{k}, \mathbf{q}) = \langle \psi_{m\mathbf{k}+\mathbf{q}} | e^{i(\mathbf{q}+\mathbf{G})\mathbf{r}} | \psi_{n\mathbf{k}} \rangle \quad (144)$$

given in section 1.4.1. We divide  $M_{m,n}$  into contributions from the muffin-tin spheres and the interstitial region

$$M_{m,n}^{\mathbf{G}}(\mathbf{k}, \mathbf{q}) = M_{m,n}^{\mathbf{G},\text{MT}}(\mathbf{k}, \mathbf{q}) + M_{m,n}^{\mathbf{G},\text{I}}(\mathbf{k}, \mathbf{q}) \quad (145)$$

The matrix element for the interstitial region is obtained within the plane-wave basis as

$$\begin{aligned} M_{m,n}^{\mathbf{G},\text{I}}(\mathbf{k}, \mathbf{q}) &= \int_{V_I} d^3r \psi_{m\mathbf{k}+\mathbf{q}}^*(\mathbf{r}) e^{i(\mathbf{q}+\mathbf{G})\mathbf{r}} \psi_{n\mathbf{k}}(\mathbf{r}) \\ &= \frac{1}{V_I} \sum_{\mathbf{G}''} \sum_{\mathbf{G}'''} c_{m,\mathbf{k}+\mathbf{q}}^*(\mathbf{G}'') c_{n,\mathbf{k}}(\mathbf{G}''') \int_{V_I} d^3r e^{i(\mathbf{G}+\mathbf{G}''-\mathbf{G}''')\mathbf{r}}. \end{aligned} \quad (146)$$

The integral over the plane waves in the interstitial region is obtained (as given in reference [157]) by integrating over the whole unit cell and subtracting the atomic sphere contributions

$$\begin{aligned} M_{m,n}^{\mathbf{G},\text{I}}(\mathbf{k}, \mathbf{q}) &= \frac{1}{\Omega} \sum_{\mathbf{G}} \sum_{\mathbf{G}'} c_{m,\mathbf{k}+\mathbf{q}}^*(\mathbf{G}) c_{n,\mathbf{k}}(\mathbf{G}') \\ &\quad \times \left( \Omega \delta_{\mathbf{G},\mathbf{G}'} - \sum_{\alpha} \int_{\text{MT}_{\alpha}} e^{i(\mathbf{G}-\mathbf{G}')\mathbf{r}} d\mathbf{r} \right). \end{aligned} \quad (147)$$

$\Omega$  denotes the unit cell volume. The atomic sphere contributions are given as

$$\int_{\text{MT}_{\alpha}} e^{i(\mathbf{G}-\mathbf{G}')\mathbf{r}} d\mathbf{r} = \begin{cases} V_{\alpha} & \text{if } \mathbf{G} = \mathbf{G}' \\ 3V_{\alpha} \frac{j_1(\mathbf{R}_{\alpha}|\mathbf{G}-\mathbf{G}'|)}{\mathbf{R}_{\alpha}|\mathbf{G}-\mathbf{G}'|} e^{i(\mathbf{G}-\mathbf{G}')\mathbf{S}_{\alpha}} & \text{if } \mathbf{G} \neq \mathbf{G}'. \end{cases} \quad (148)$$

where  $\mathbf{S}_\alpha$  denotes the position vector of atom  $\alpha$  with radius  $\mathbf{R}_\alpha$ . For the description of the plane waves within the muffin tin spheres a Rayleigh expansion in terms of spherical harmonics  $Y_{LM}$  and Bessel functions  $j_L$  is utilized

$$e^{i\mathbf{G}\mathbf{r}} = 4\pi e^{i\mathbf{G}\mathbf{S}_\alpha} \sum_{LM} i^L j_L(\mathbf{G}|\mathbf{r} - \mathbf{S}_\alpha|) Y_{LM}^*(\hat{\mathbf{G}}) Y_{LM}(\widehat{\mathbf{r} - \mathbf{S}_\alpha}). \quad (149)$$

The matrix element within the muffin-tin spheres is given as

$$\begin{aligned} M_{m,n}^{\mathbf{G},\text{MT}}(\mathbf{k}, \mathbf{q}) &= \int_{V_{\text{MT}}} d^3r \psi_{m\mathbf{k}+\mathbf{q}}^*(\mathbf{r}) e^{i(\mathbf{q}+\mathbf{G})\mathbf{r}} \psi_{n\mathbf{k}}(\mathbf{r}) \\ &= \sum_p \sum_{p'} \sum_{LM} \sum_{L'M'} \sum_{L''M''} \int_{V_{\text{MT}}} d\Omega Y_{LM}^* \times (\hat{\mathbf{r}}) Y_{L'M'}(\widehat{\mathbf{r} - \mathbf{S}_\alpha}) Y_{L''M''}(\hat{\mathbf{r}}) \\ &\quad \times \int_{V_{\text{MT}}} dr \mathbf{r}^2 u_{L,p}^*(\mathbf{r}, \epsilon_L) u_{L'',p'}(\mathbf{r}, \epsilon_{L''}) j_{L'}(|\mathbf{q} + \mathbf{G}||\mathbf{r} - \mathbf{S}_\alpha|) \\ &\quad \times \tilde{A}_{LM,p}^m(\mathbf{k} + \mathbf{q}) \tilde{A}_{LM,p'}^n(\mathbf{k}) \tilde{B}_{L'M'}^n(\mathbf{q} + \mathbf{G}) \end{aligned} \quad (150)$$

where the following relations have been used

$$\begin{aligned} \tilde{A}_{LM,p}^m(\mathbf{k} + \mathbf{q}) &= \sum_{\mathbf{G}''} c_{m,p,\mathbf{k}+\mathbf{q}}^*(\mathbf{G}'') A_{LM,p}^*(\mathbf{k} + \mathbf{q} + \mathbf{G}'') \\ \tilde{A}_{LM,p'}^n(\mathbf{k}) &= \sum_{\mathbf{G}'''} c_{n,p',\mathbf{k}}(\mathbf{G}''') A_{L''M'',p'}(\mathbf{k} + \mathbf{G}''') \\ \tilde{B}_{L'M'}^n(\mathbf{q} + \mathbf{G}) &= i^{L'} 4\pi e^{i(\mathbf{q}+\mathbf{G})\mathbf{S}_\alpha} Y_{L'M'}^*(\widehat{\mathbf{q} + \mathbf{G}}). \end{aligned} \quad (151)$$

### 5.3 Gauss quadrature

According to the Gauss quadrature integration scheme, the integral of a polynomial function  $f(x)$  of degree  $2N - 1$  in the interval  $[a, b]$  with the weight function  $w(x) > 0$

$$I(f) = \int_a^b w(x) f(x) dx \quad (152)$$

is approximated by an  $N$ -point sum

$$I(f) \approx \sum_i^N w_i f(x_i) \quad (153)$$

where  $w_i$  and  $f(x_i)$  are the weights and abscissas, respectively. Hence the idea of the Gauss quadrature is to not only choose the supporting points freely but be free to choose the weighting function too. One choice for the weighting function and the interval of the abscissas is  $w(i) = 1$  and  $-1 < x < 1$ , respectively. This is also known as Gauss–Legendre integration (a table of the other most common weight functions and abscissas is given in chapter 4.5 of reference [158]).

The integral for the correlation energy in equation 84 has the form of

$$E_c = \int_0^{\infty} f(\omega) d\omega = \int_0^{\infty} (\ln[1 - \chi v] + v\chi). \quad (154)$$

We calculate this integral with the general Gauss–Legendre integration formula

$$E_c \approx \int_0^{\omega_{max}} f(\omega) d\omega = \sum_i^N w_i f(\omega_i) \quad (155)$$

following the FORTRAN [159] implementation given in chapter 4.5 of reference [158].

## 5.4 Quantum chemistry calculations

All calculations in this chapter and in appendix 5.4.1 were carried out by Paul Tiwald<sup>6</sup>.

Active clusters of the sizes (1) Li<sub>14</sub>F<sub>12</sub>, (2) Li<sub>38</sub>F<sub>18</sub>, (3) Li<sub>62</sub>F<sub>62</sub>, and (4) Li<sub>92</sub>F<sub>86</sub> were used. For proper embedding, several layers of *ab-initio* model potentials (AIMPs) [160, 161] and a large matrix of point charges of cubic shape arranged as proposed by Evjen [162] with fractional charges of +/- 0.5, 0.25 and 0.125 at faces, edges and corners, respectively, were used. AIMPs are all-electron potentials in which, in contrast to pure point charges, also exchange terms are included by using non-local potentials. Exchange leads to repulsive forces between electrons of equal spin, or in this case, between the active electrons and the “frozen” electrons of the AIMPs. Their use is crucial in order to prevent nonphysical excessive polarization of the active anions due to neighbouring point charges and leakage of the electron cloud out of the region of the active cluster. For every cluster the size of AIMP and point charge embedding was chosen such that convergence of the absorption energy was reached. For the large cluster, which has cubic shape, four layers of

---

<sup>6</sup>Paul Tiwald, Institute for Theoretical Physics, Vienna University of Technology, Wiedner Hauptstraße 8-10, A-1040 Vienna, Austria

AIMPs (2072 in total) and five layers of point charges (9970 in total) enclosing the active region were used. Dunning’s correlation-consistent polarized valence only basis sets [163] of double, triple and quadruple zeta quality (cc-pVDZ, cc-pVTZ, cc-pVQZ) were applied which are in the following referred to as the small, medium and large basis set, respectively. In addition to the basis sets localized at the ionic sites, a set of basis states pertaining to the F atom at the vacancy site were placed. It should be noted, however, that in line with earlier studies [164–166] this latter basis set has only little effect on the convergence. On the Hartree–Fock level, the absorption energy of the cluster is calculated as the energy difference of two restricted open shell Hartree–Fock (ROHF)  $N$ -electron wave functions with different symmetries corresponding to the ground state and the first optically allowed excited state. Quantum chemistry offers a large variety of methods beyond the Hartree–Fock level allowing for the inclusion of correlations. Methods specifically suited for accounting for dynamical correlation were applied such as complete active space second order perturbation theory based on a single ROHF determinant CASPT2(ROHF) (a generalization of second-order Møller–Plesset perturbation theory (MP2)), the coupled cluster single-double (CCSD) and the coupled cluster single-double-perturbative triple (CCSD(T)) methods. For this group the starting point is the ROHF wave function of either the ground or the excited state. The influence of static correlation by applying the complete active space self-consistent field (CASSCF) method and second order perturbation theory based on a multi-determinant wave function (CASPT2(CAS)) was also checked. The CAS size for the ground state ( $A_g$  symmetry) was determined by correlating all occupied valence orbitals (F-2p orbitals) of  $A_g$  symmetry plus a number of virtual orbitals also of  $A_g$  symmetry. For the excited state the same procedure was applied within one of the  $B_u$  symmetries. For the medium cluster and medium basis set the largest CASs tested were (19,13) corresponding to 19 electrons in 13 orbitals and (17,11) for the ground and excited state, respectively leading to only small shifts of the total energies. This indicates the strong dominance of a single configuration. The effect of static correlation, i.e. difference between CASPT2(CAS) and CASPT2(ROHF), on the absorption energy is a decrease of less than 0.02 eV. HF, CASPT2(ROHF), CCSD and CCSD(T) excitation energies of the small cluster are given in table 12 for different basis sets. Note that CCSD and CCSD(T) could not be calculated for the larger basis sets. The last line in table 12 shows values for the converged basis set (CBS) limit obtained by employing the extrapolation scheme proposed by Truhlar [167, 168]. This scheme is tailored to extrapolate perturbation theory, CCSD and CCSD(T) energies from the cc-pVDZ and cc-pVTZ basis sets to the CBS limit allowing for application to cases where cc-pVQZ calcu-



Table 12: Excitation energies of  $\text{Li}_{14}\text{F}_{12}$  cluster calculated with different quantum chemistry methods and basis set sizes using the unperturbed crystal geometry and the experimental lattice constant.

Basis set	ROHF	CASPT2(ROHF)	CCSD	CCSD(T)
cc-pVDZ	6.31	5.99	6.00	5.94
cc-pVTZ	6.27	5.84	5.86	–
cc-pVQZ	6.26	5.79	–	–
CBS limit	6.26	5.73	5.77	–

Table 13: CASPT2(ROHF) excitation energies calculated with different cluster sizes and basis sets using the unperturbed crystal geometry and the experimental lattice constant.

Basis set	$\text{Li}_{14}\text{F}_{12}$	$\text{Li}_{38}\text{F}_{18}$	$\text{Li}_{62}\text{F}_{62}$	$\text{Li}_{92}\text{F}_{86}$
cc-pVDZ	5.99	5.87	5.76	5.74
cc-pVTZ	5.84	5.73	5.61	–
cc-pVQZ	5.79	5.70	–	–
CBS limit	5.73	5.63	5.50	–

lations were not possible. Table 12 shows that the CASPT2(ROHF) method closely reproduces the excitation energy determined by methods that include correlations to a larger degree such as CCSD and CCSD(T). For example, the CBS limits of the CASPT2(ROHF) and the CCSD differ by only 0.04 eV. A comparison between CASPT2(ROHF) and CCSD(T) excitation energies is only possible for the small basis set. In this case the CCSD(T) excitation energy is 0.05 eV lower than the CASPT2(ROHF) value. In view of these negligible deviations ( $\lesssim 1\%$  of the experimental excitation energies) the numerically relatively cheap CASPT2(ROHF) method was employed to larger clusters to check for cluster-size convergence. The CASPT2(ROHF) excitation energies for the different cluster sizes and the different basis sets as well as the extrapolated CBS values are given in table 13. Since for the small basis set the difference between the large and very large cluster is only 0.02 eV, the excitation energy calculated for the large cluster is considered to be converged within a satisfactory level of accuracy. All results given in the following refer to the CBS limit of the large cluster unless otherwise stated.

The solid-state physics approach and the quantum chemistry approach can be compared on several levels. On the single-particle level we can compare the Hartree-Fock and the Kohn-Sham orbitals generated with the TB-

mBJ exchange-correlation potential. Both approaches lead to a similar structure of the single particle levels in a ground-state calculation: the occupied s-type and unoccupied p-type levels lie within the band gap and the corresponding orbitals are localized within the vacancy region. Both orbital pairs agree in size and shape (see figure 34).

We also find good agreement between the two approaches concerning the ground state relaxation of the nearest and next-nearest neighbors surrounding the  $F$  center. DFT and CASPT2(ROHF) lead to an identical outward relaxation of 0.04 Å of the nearest-neighbor  $\text{Li}^+$  ions and to similarly small outward relaxation of the  $\text{F}^-$  ions (0.01 Å in DFT (see chapter 2.5) and 0.024 Å in CASPT2(ROHF)). The small discrepancy for the  $\text{F}^-$  ions might be in parts caused by the limited cluster size for which the CASPT2(ROHF) geometry relaxation was performed. It should be noted that such an agreement between periodic DFT and quantum chemistry cluster calculations is not standard. For example, for the  $F$  center in MgO the relaxation of the  $\text{Mg}^+$  ion obtained from periodic DFT [116] and from cluster calculations on the HF level [169] differ by a factor of  $\sim 5$ .

#### 5.4.1 Calculated line-width

The line width of the  $F$ -center absorption in alkali halides is significantly influenced by electron-phonon interactions. Lifetime broadening can be neglected due to the long lifetime [170] of up to  $\sim 10^{-6}$  s of the excited state. Typically one local mode defining the relevant configuration coordinate dominates the line width and the absorption process [93,171]. In the present case this mode is the symmetric breathing mode of the six  $\text{Li}^+$  ions surrounding the vacancy (inset in Fig. 35). Using the medium basis set and medium cluster size we have calculated the configuration coordinate diagram of this mode for the ground and excited state of the  $F$  center (Fig. 35) and extracted a vibration frequency (15.78 THz, 65.2 meV) and a line width of 0.27 eV due to the zero-point fluctuations. Stoneham [93] proposed, as a “rule of thumb”, that the frequency of this mode is comparable to the transverse optical phonon frequency of the bulk material. For pristine LiF the TO modes lie at  $\sim 10$  THz [172,173] which compares reasonably well with our estimates. Also the resulting theoretical line width extracted from the configuration coordinate curves is in fair agreement with the experimental values [105,174] at low temperatures ranging from 0.42 to 0.61 eV. This single-mode estimate for the line width should be considered as a lower bound to the experimental line width. Possible effects that would further increase the theoretical line width

are additional modes comprising ions beyond the nearest neighbors, thermal broadening, broadening due to imperfections of the crystal (inhomogeneous broadening), and experimental broadening (e.g.: finite line width/resolution of source/detector).

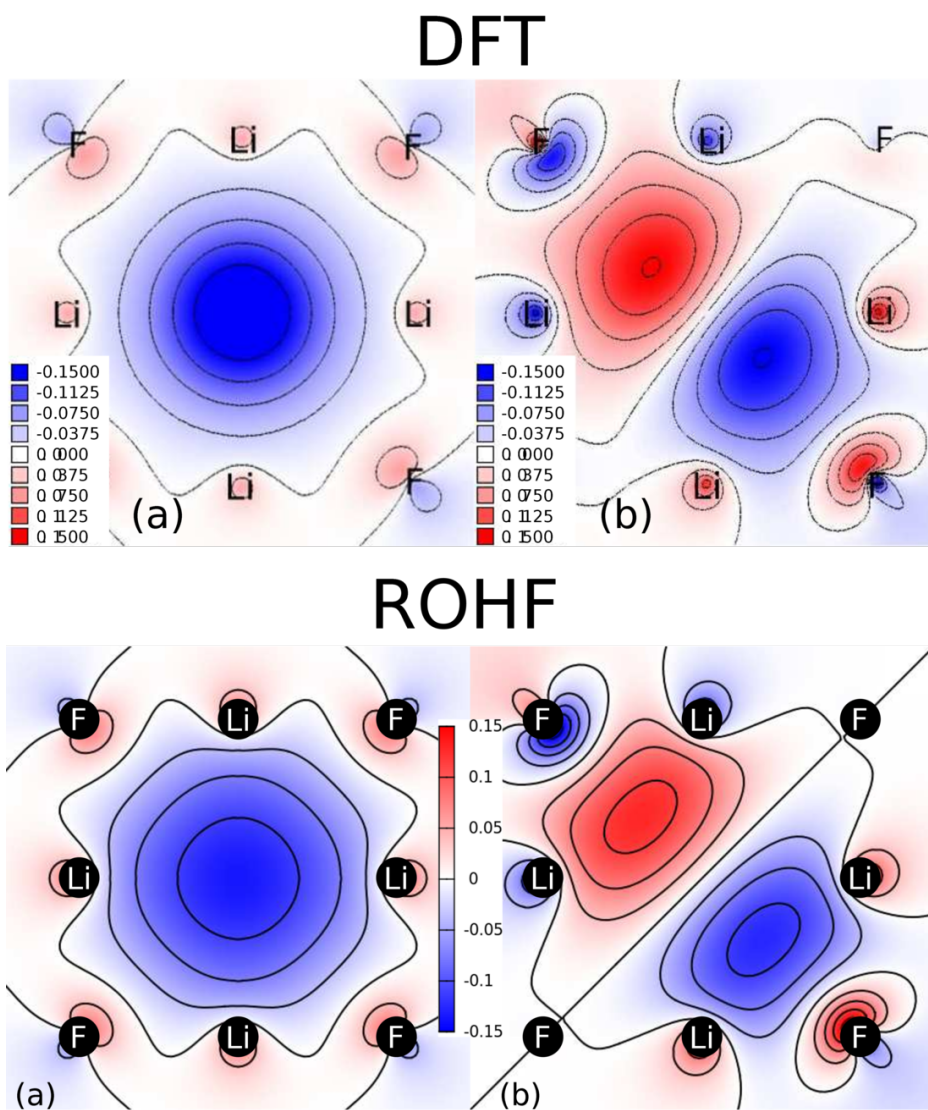


Figure 34: TB-mBJ and ROHF orbitals for the  $F$ -center bands within the [100] plane: a) occupied s-orbital, b) one of the three degenerate unoccupied p-orbitals. The DFT orbitals were calculated using the  $\text{Li}_{32}\text{F}_{31}$  unit cell. The ROHF orbitals are taken from a calculation using the (medium)  $\text{Li}_{38}\text{F}_{18}$  cluster and the (medium) cc-pVTZ basis set. Units are in atomic units.

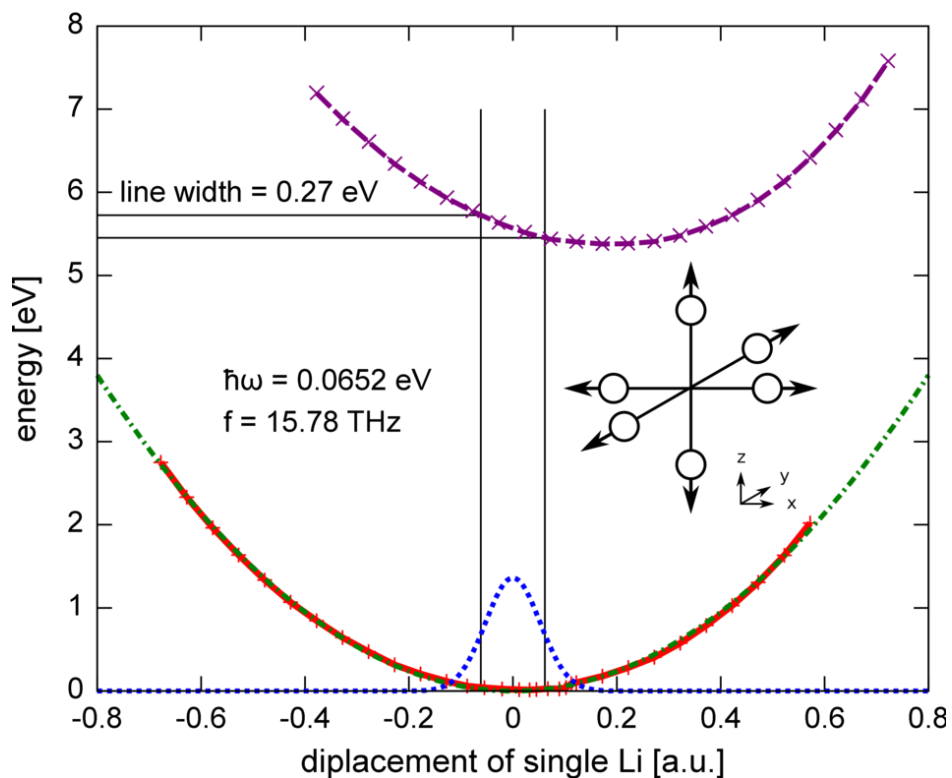


Figure 35: Calculated configuration coordinate curves for ground (red full line) and excited (violet dashed) state of the  $F$  center in LiF as a function of the elongation along the symmetric breathing vibration of the six  $\text{Li}^+$  ions surrounding the defect for the (medium)  $\text{Li}_{38}\text{F}_{18}$  cluster and the (medium) cc-pVTZ basis set. The blue (dotted) line is the absolute magnitude squared of the ground-state wave function of an harmonic potential with  $\hbar\omega=0.0652$  eV (green dash-dotted line). The inset schematically depicts the symmetric breathing vibration of the six  $\text{Li}^+$  ions surrounding the defect.

## 5.5 Tutorials for GW, BSE and ACFDT within the WIEN2k package

A detailed description of how to run GW, BSE and ACFDT calculations within the WIEN2k package is given in this chapter.

### 5.5.1 GW calculations

Since GW calculations are applied perturbatively on standard DFT calculations (using local or semi-local exchange-correlation functionals) good convergence of the underlying standard DFT calculations is required.

The preparation of the GW calculations is done automatically by calling the script "gap2\_init" in the directory of the DFT calculation. All setup options can be viewed by executing the command "gap2\_init -h". The options "-d sample" and "-nkp x" which define the subdirectory "sample" for the GW calculation and the number of  $k$  points  $x$ , respectively, have to be set in each calculation. Since the GW method involves transitions between valence and conduction bands, a high number of conduction bands is required. To account for this the parameter `emax` in the `case.in1` file has to be raised already for the DFT calculations (a good value is around 7.5 to 10 Ryd for many insulators). The GW calculation is started by changing into the GW subdirectory "sample" and calling the mpi command "mpirun -np nproc gap2.x", where `nproc` is the number of processors used. The number of mpi processors and the calculational parameters have to be chosen cautiously, since the calculations can be very time and memory exhaustive (i.g. Li16F15 with 8  $k$ -point,  $RK_{max} = 7$ , `emax` of 7.5,  $Q = 0.4$ , `emingw` of -3.0, `emaxgw` of 5.0 and `barcevtol` of 0.0 using 64 cores needs 15 GB memory per core and roughly 3 days to complete the calculation). The outputfile `case.outgw` contains the most important outputs.

Inputfile:

The main input file for the GW options (which is created automatically by the script "gap2\_init") is the `case.ingw` file which usually looks as follows (all frequencies and energies are in Hartree)

```
# Input file for gw calculation
# Initialization options: gap_init -d Sample -s 2 -nkp 8
# iopk=0
Task = "gw"           # Option for task
Restart = F           # Option for whether restarting a
                       # previous calculations
nspin = 2             # 1 for spin-unpolarized and 2 for
                       # spin-polarized calculations
```

```

ComplexVector = F      # T for for systems without inversal
                       # symmetry
CoreOpt = "all"       # Option for treating core levels
UseScratch=T          # Set F if not using scratch space
                       # in which zzk are all kept in core
                       # and minm is always calculated from
                       # scratch. This might be more
                       # efficient when using IBM Power 5
                       # without local space

SymVector = T         # whether to use Kohn-Sham
                       # eigenvectors in the irreducible
                       # Brillouin zone

Minm_mblksiz = 48    # block size to split m-index for
                       # the calculations of minm
barcevtol = 0.6      # tolerance used to reduce the
                       # bare Coulomb matrix eigenvectors
                       # as the basis set for sp systems,
                       # barcevtol=0.6 is usually quite
                       # safe.

emingw = -3.0         # emingw and emaxgw (Ryd) are used
                       # to control the range of bands
emaxgw = 5.0         # for which GW correction are
                       # going to be calculated. Only
                       # states whose LDA energies falls
                       # between E_Fermi+emingw and
                       # E_Fermi+emaxgw are calculated

%SelfEnergy          # option for correlation self-energy
  2 | 0 | 1          # <npol> | <iopes> | <iopac>
%                   # Number of poles (previous maxexp+1,
                       # valid range: 2.. nomeg/2 )
                       # iopes: 0/1/2/3 - without or with
                       # iteration >
                       # iopsac:0/1 - Pade's approximation
                       # /multipole fitting

%BZConv              # BZ convolution options
  "tetra" | "imfreq"

```

```

%
%FreqGrid          # Frequency grid param.
3 | 16 | 0.42 | 0.0 | 0 # iopf|nom|ommax|ommin|nomeg_blk
%                   # iopfq= 1 (eq. spaced),
%                   # 2 (Gauss-Laguerre) or
%                   # 3 (double Gauss-Legendre)

%MixBasis          # Mixed basis parameters
0.4 | 1 | 1.E-2    # Q, lmax_mb, lamda_mb
%

%BareCoul          # Options to control the calc. of
2.0 | 1.E-15      # the bare Coulomb matrix
%

nvel = 153.0      # the number of valence electrons

```

The most important parameters besides the  $k$  mesh, the energy cutoff parameter  $RK_{\max}$  and the cutoff for the number of conduction bands (emax in case.in1) are given in this file. The parameter  $Q$  is the main parameter to control the quality of the basis set for GW within the product basis expansion (for details on this and all other parameters see reference [86]). The parameter barcevtol is used to control the tolerance for the reduction of the bare Coulomb matrix elements which are quite time and memory exhaustive within the product basis expansion (a value of 0.6 is usually safe for many systems). For most cases a Gauss–Legendre integration routine is used for the frequency integral in equation 1.7.2 (usually 16 points and a maximal frequency of 0.42 Hartree are safe values). In principle all parameters have to be checked for convergence to obtain high quality results, but most of the parameters given in the example file (and set automatically by "gap2\_init") are safe values. In summary the most important parameters controlling the quality and computation time of the calculations are the size of the  $k$  mesh,  $RK_{\max}$ , number of conduction bands,  $Q$  and barcevtol.

### 5.5.2 BSE calculations

The BSE calculations are applied perturbatively on top of standard DFT or GW calculations. The BSE program consists of four separate programs:

- DM: Calculates the microscopic dielectric function.
- WD: Calculates the direct term of the BSE Hamiltonian.



Table 14: Necessary files for BSE calculations. The first column shows the WIEN2k file name. The second column shows the filename for BSE.

WIEN2k	BSE
case.vsp	vsp
case.vns	vns
case.inop	inop
case.struct	struct
case.in1	in1_DM,in1_WDVX
	inBSEkgen
	input
	energy_DM,energy_WDVX
	vector_DM,vector_WDVX
	mommat_DM,mommat_WDVX

- VX: Calculates the exchange term of the BSE Hamiltonian.
- BSEdiag: Solves the BSE Hamiltonian and calculates the coupling coefficients for the macroscopic dielectric function given in the form of equation 125.

The BSE calculations are applied perturbatively on top of standard DFT or GW calculations. Files containing the vectors and the eigenvalues for the whole Brillouin zone are required to run the calculations. Also a higher number of conduction states than in standard DFT calculations is required. To account for this the parameter `emax` in the `case.in1` has to be increased (a good value is around 7.5 to 10 Ryd for many insulators).

The necessary files for running a BSE calculation are listed in table 14. If the calculations are carried out spin-polarized the calculation is split into to calculations for the spin-up and spin-dn states. All files with the exception of `inBSEkgen` and `inop` get an affix `"_up"` and `"_dn"` for the spin-up and spin-dn calculations, respectively. The BSE programs are not using the `"case.ending"` nomenclature.

The following steps are needed to prepare a BSE calculation:

1. Setting up calculational directory
2. Copying the `struct`, `vsp`, `vns`, `in1_DM`, `in1_WDVX` `inBSEkgen`, `inop` and `input` files from the preliminary calculation into the calculational

directory. The parameter `emax` in `in1_DM` and `in1_WDVX` has to be set to a higher value.

3. Executing `"execBSEkgen"`. This program prepares the necessary input files for the  $k, k'$  pairs.
4. Executing `execlapwloptic`: This program calculates the necessary energy, vector and `mommat` files. The `mommat` files are needed for the calculation of the head and the wings of the microscopic dielectric function.

The following `mpi` programs have to be executed consecutively to run the BSE calculation ("`-np nproc`" defines the number of processors `nproc`):

1. `"mpirun -np nproc DM [-up] [-dn]"`
2. `"mpirun -np nproc WD [-up] [-dn]"`
3. `"mpirun -np nproc VX [-up] [-dn]"`
4. `"mpirun -np nproc BSE_diag [-up] [-dn]"`

In the case of no inversion symmetry all of these programs have to be called with the suffix `"c"`, i.e. `DMc`)

In the following the three input files needed to control the BSE calculations are described.

#### **inop:**

```
500000  1      last and first k-point
-7.0 7.5      Emin, Emax for matrix elements
3          number of choices (columns in *outmat)
1          Im xx
2          Im yy
3          Im zz
ON
```

This file controls the input parameters for the macroscopic dielectric tensor, which is calculated by calling the `optic` [157] program available within the WIEN2k package.

#### **inBSEkgen:**

```

1          0 = no symmetry , 1 = with symmetry
0 0  0      5  q-vector (qx,qy,qz,qdiv)
1          switch (see below)
3  3  3      division of Brillouin zone for DM
3  3  3      WD/VX

line 1 :  0 = no symmetry operations are used
          1 = the symmetry of the given q-vector is exploited

line 2 :  qx   qy   qz   qdiv (do not change)

line 3 :  0 = generates 2 k-lists shifted by
           the vector q (case.klist and case.klistq)
           1 = generates list of all possible {k,k+q}
               pairs, a list of all q-vectors
               and a unix-script to calculate the
               dielectric matrix for all q's needed.
           2 = generates 2 k-lists used for the matrix
               elements needed for the computation
               of lifetime of hot electrons.
           case.klist : contains only the q-vector from
                       line 2 (actually it is a k
                       in this context)
           case.klistq : contains all k+q vectors needed

line 4 :  division of Brillouin zone for DM
line 5 :  if exists division of Brillouin zone for VX, WD
line 6 :  if exists extras ( na nb nc)
line 7 :  if exists (1 - only extras, 0 - extras + rest)

```

This file controls the input parameter for the  $k$  mesh.

#### input:

```

scissors  0.0      # scissors shift [eV]
scalebands 1.0 1.0 # scaling factor for (val., cond.) bands
eminmaxDM -7.0 7.5 # energy cutoff for DM
gmax_WD   2.0     # max. magnitude of G vector for exp(iGr)
gmax_VX   2.0     # max. magnitude of G vector for exp(iGr)
gmax_DM   2.0
gmax_DM_max 2.0
lmax_besel 2     # max of l in expansion of exp(-i(q+G)r)

```

```

lmax_wave 2 # max of l in expansion of wave func. (sphere)
offesDM 1 # calculate off-diag elements of eps_GGp(q)
formatVXWD 1 # VX, WD files 0-ascii, 1-binary
nbandsVXWD 1 5 # number of (val.,cond.) bands in VX, WD
nbandsBSE 1 5 # number of (val.,cond.) bands used in BSE
noccbands 77 # number of occupied bands
noccbandsDM 77

nbuf 1000

scrlevel 1 # screening level in WD:
# 1 - the full {g, g'} dependence is used
# 2 - a diag. approx. is used (g = g') using
# the inve. diel. matrix eps^{-1}_{gg}(q)
# 3 - a diag. approx. is used (g = g') using
# the dielectric matrix eps_{gg}(q)
# 4 - a long range screening
# is used (const. tensor)

epstensor #
6.8576111 0.0000000 0.0000000
0.0000000 6.8576105 0.0000000
0.0000000 0.0000000 6.5021884

diroffBSE 1 # 0 : local field effects only
# (direct interaction = zero)
nexoutBSE 10000 # number of states written
# into files
eminemaxBSE 0.0 30.0 0.02 # emin, emax, de in [eV]
broadBSE 0.12 0 # broadending of spectrum [eV]
# , lineshape
polBSE 1 # polarization
spinBSE 1 # 1 -singlet, 2 - triplet
factor_WD 1.0

g_par 0 # 0: parallelization only over
# number of G vectors
# 1: first parallelization over:
# number of k and q in DM
# number of kkp pairs in WD

```

```

#           number of k points in VX
#   second parallelization over number
#   of G vectors
blocksize 64 # blocksize for G vector parallelization

```

This file controls the main input parameters for the BSE calculations. A short description for the parameters is given in the following:

- scissors: Gives a scissor shift in the calculation of the microscopic dielectric function.
- scalebands: Scaling factor of valence and conduction bands
- eminmaxDM: Controls the energy range for the bands involved in the calculation of the dielectric matrix. A value of 7.5 to 10 Ryd is usually safe for many insulators.
- gmax\_DM,gmax\_WD,gmax\_Vx: Sets the maximum value of the  $\mathbf{G}$  vector in the expansion of  $e^{i(\mathbf{q}+\mathbf{G})\mathbf{r}}$  for the matrix elements within the muffin-tin spheres (see equation 150).
- lmax\_bessel: Sets the maximum value of  $l$  in the expansion of  $e^{i(\mathbf{q}+\mathbf{G})\mathbf{r}}$ .
- lmax\_wave: Sets the maximum value of  $l$  in the expansion of the wave function within the muffin-tin spheres.
- offesDM: Controls whether off diagonal elements of the microscopic dielectric function are calculated or not (0 - off-diagonal elements are zero. 1 - off-diagonal elements are calculated).
- formatVXWD: Controls the format of the output files in VX, WD.
- nbandsVXWD, nbandsBSE: Controls the number of valence and conduction bands used in the calculation of the exchange and direct term of the BSE Hamiltonian and the diagonalization of the Hamiltonian, respectively. The calculational time depends very strongly on these values. Usually for good quality calculations all valence bands and a lot of conduction bands are needed. The number of bands can be reduced for e.g. strongly localized valence electrons, but convergence tests have to be conducted in each case.
- noccbands,noccbandsDM: Number of valence bands. This parameter has to be set correctly, otherwise the program will not know how many valence bands are used (these values can be easily obtained from the case.scf files).

- nbuf: Buffer size used in the calculations (a value of 1000 is quite safe).
- scrlevel: Describes the screening for the direct term (always use 1).
- epstensor: Describes the long range tensor if option 4 is chosen for scrlevel.
- diroffBSE: Controls whether direct term is set to zero or not (0 - direct term is set to zero, 1 - direct term is fully calculated).
- nexoutBSE: Number of states written into output files.
- eminemaxBSE: Sets the output parameters for the macroscopic dielectric function.
- broadBSE: Controls the broadening of the spectrum.
- polBSE,spinBSE,factor\_WD: Control parameters for special cases.
- g\_par: Controls how the program is parallelized ( 0 - used for big cells with a very high number of  $\mathbf{G}$  vectors and a low number of  $k$  points or when the memory allocation is a critical issue, 1 - used for small cells with many  $k$  points and low memory usage).
- blocksize: Controls the blocksize for the scalapack routines.

Some comments on running and setting up the BSE calculations:

- Depending on the case several hundreds of computational cores are needed for the calculations, i.e. a calculation for a  $\text{Li}_{16}\text{F}_{15}$  cell with  $RK_{max} = 7$ ,  $k$  mesh of  $6 \times 6 \times 6$ ,  $G_{max} = 2 \text{ Bohr}^{-1}$ ,  $emax = 10.5$  Ryd, 1 valence band and 5 conduction bands for the BSE Hamiltonian requires altogether a calculation time of 36 hours on 800 cores.
- The main output files are `epsilon(_singlet, _triplet)` and `epsilon(_singlet, _triplet)_noint` files which contain the macroscopic dielectric function with and without corrections from the BSE, respectively. The output file `exciton(_singlet, _triplet)` contains the excitonic energies, binding energies and oscillator strengths.

### 5.5.3 Volume optimization within the ACFDT formalism

The ACFDT calculations consist of 3 steps (as described in section 4):

1. A preliminary DFT calculation using a (semi-)local exchange-correlation functional.
2. Calculation of the Hartree–Fock exchange energy using the previously calculated DFT orbitals.
3. Calculation of the ACFDT correlation energy using the DFT orbitals.

These steps are wrapped up into scripts for the volume optimization. The (RPA-)ACFDT calculations are performed starting from the calculational directory of the standard WIEN2k calculation using the following steps:

1. All files and the calculational directory have to be (re)named (from "case.\*") to "HFRPA.\*", since the scripts need this kind of file structure.
2. "x optimize" has to be run in the calculational directory to obtain the desired volumes.
3. The first parameter in "HFRPA.in0" has to be changed from TOT to KXC. Also the IFFT grid and the enhancement factor (at least 4) in "HFRPA.in0" have to be increased.
4. "init\_hf" has to be run in the calculational directory to create the necessary input files.  $\alpha$  has to be set to 1.00 and the line containing  $\lambda$  ( $\lambda=0.165$ ) has to be deleted to obtain pure Hartree–Fock exchange. The line for nband is not used, but should be set to an arbitrary value. gmax has to be set to a very high value ( $\text{gmax}=12$ ) to obtain good convergence.
5. "x kgen" has to be executed again using the same  $k$  mesh as for Hartree–Fock.
6. The parameter emax in HFRPA.in1 has to be set to a higher value (usually 7.5 to 10 is safe for most insulators).
7. The necessary input files input, inop and inACkgen have to be copied into the calculational directory and renamed as HFRPA.input, HFRPA.inop and HFRPA.inACkgen, respectively. The input parameters in these files are described below.

8. The `optimize.job` script for ACFDT calculations has to be copied to the calculational directory. After the setting the parameters in this file the command `"optimize.job"` has to be executed. This script generates the input directories for the ACFDT correlation-energy calculations at different volumes, as e.g. `"AC_HFRPA_vol*"`, and runs the (semi-)local DFT and Hartree–Fock calculations.
9. The (RPA-)ACFDT correlation energy calculations are started for each volume separately in the corresponding subdirectory `"AC_HFRPA_vol*"` by calling the command `"mpirun -np x AC"`, where `"-np x"` defines the number of processors `x`.
10. The main output file is `outputAC`. The lattice constant using ACFDT correlation energies is obtained by calling the script `"hfrpa_analyzer"` in the calculational directory (for available options call the command `"hfrpa_analyzer -h"`).

The input files for the Hartree–Fock calculations are described within the WIEN2k manual [85]. The 4 necessary input files for the calculation of the ACFDT correlation-energy are explained in the following.

#### **HFRPA.inop:**

```
500000  1          last and first k-point
-7.0 10      Emin, Emax for matrix elements
3          number of choices (columns in *outmat)
1          Im xx
2          Im yy
3          Im zz
ON
```

#### Choices:

```
1.....Im(eps)xx
2.....Im(eps)yy
3.....Im(eps)zz
4.....Im(eps)xy
5.....Im(eps)xz
6.....Im(eps)yz
7.....Re(eps)xy
8.....Re(eps)xz
9.....Re(eps)yz
```



This file controls the input parameters for the macroscopic dielectric tensor, which is calculated by calling the optic [157] program available within the WIEN2k package. The macroscopic dielectric tensor is used for the construction of the head and wings of the microscopic dielectric matrix. The only relevant parameters are Emin and Emax in this input file (usually a value of 7.5 to 10 for Emax is quite safe for many insulators).

### HFRPA.inACkgen:

```

1                0 = no symmetry , 1 = with symmetry
0  0  0  10      q-vector (qx,qy,qz,qdiv)
1                switch (see below)
4 4  4          division of Brillouin zone for AC
4 4  4          WD/VX

line 1 :  0 = no symmetry operations are used
          1 = the symmetry of the given q-vector is exploited

line 2 :  qx   qy   qz   qdiv

line 3 :  0 = generates 2 k-lists shifted by the
          vector q (case.klist and case.klistq)
          1 = generates list of all possible {k,k+q}
          pairs, a list of all q-vectors and a
          unix-script to calculate the dielectric
          matrix for all q's needed.
          2 = generates 2 k-lists used for the matrix
          elements needed for the computation
          of lifetime of hot electrons.
          case.klist   : contains only the q-vector
                       from line 2 (actually it is
                       a k in this context)
          case.klistq  : contains all k+q vectors needed

line 4 :  division of Brillouin zone for AC

```

This file controls the input parameter for the  $k$  mesh.

### HFRPA.input:

```

noccbandsAC 4      # Number of occupied bands
scissors    0.0    # scissors shift [eV]

```

```

eminmaxAC -7.0 900.5 # energy cutoff for AC
gmax_AC      8.0      # Cutoff for reciprocal lattice vectors
gmax_AC_max  8.0
gnum_extrapol  5      # Number of G's for extrapolation
gratio_extrapol 0.05 # Reduction for each step in
                  # extrapolation (0.05=5%)
scalebands   1.0 1.0 # scaling factor for (val., cond.) bands
lmax_besel   4      # max of l in expansion of exp(-i(q+G)r)
lmax_wave    4      # max of l in expansion of wave
                  # function (sphere)
g_par        1      # 0: parallelization only over number
                  # of G vectors
                  # 1: first: number of k and q in AC
                  # second: parallelization over
                  # number of G vectors
blocksize    64      # blocksize for G vector parallelization
broadAC      0.0     # opt. input: broadening for polarization
omegaAC 1 0.0 35.0 16 # frequ. grid: integr. scheme, min, max,
                  # number of frequency points(even)
                  # integration schemes:
                  # 0 - equally space
                  # 1 - Gauss-Legendre
calc_head 0      # 0: head calculated
                  # 1: head set to 0
calc_wings 0     # 0: wings calculated
                  # 1: wings set to 0
freq_opt 1      # Option for storage of frequ. points
                  # 0: frequency outer loop
                  # (high cpu time, low mem)
                  # 1: frequency inner loop
                  # (low cpu time, high mem)

```

A short description for the parameters is given in the following:

- `noccbandsAC`: Number of valence bands. This parameter has to be set correctly, otherwise the program will not know how many valence bands are used (these values can be easily obtained from the `case.scf` file).
- `scissors`: Gives a scissor shift in the calculation of the microscopic dielectric function.

- `eminmaxAC`: Controls the energy range for the bands involved in the calculation of the dielectric matrix. `Emax` has to be set to a very high value since all bands are needed to correctly describe the RPA correlation energy (units in Ryd).
- `gmax_AC`: Sets the maximum value of the  $\mathbf{G}$  vector in the expansion of  $e^{i(\mathbf{q}+\mathbf{G})\mathbf{r}}$  for the matrix elements within the muffin-tin spheres (see equation 150). This value should be set to a value which is approximately 75 to 90 percent of  $\mathbf{K}_{max}$ , which is the cutoff for the largest vector of the basis set in `in1_AC` (see  $RK_{max}$ ), to obtain a balanced basis set [149].
- `gnum_extrapol`: The correlation energy in the infinite large  $\mathbf{G}$  limit  $\mathbf{G}_\infty$  is obtained by extrapolation of the correlation energies at different  $\mathbf{G}_i$ 's using the following equation  $E_c(\mathbf{G}_i) = E_c(\mathbf{G}_\infty) + \frac{A}{(\mathbf{G}_i)^3}$ . `gnum_extrapol` controls the number of points  $i$  for the extrapolation.
- `gratio_extrapol`: Sets the reduction step  $s_r$  for  $\mathbf{G}_i$  which are applied as  $\mathbf{G}_i = \mathbf{G}_{max} \cdot s_r^i$ .
- `lmax_bessel`: Sets the maximum value of  $l$  in the expansion of  $e^{i(\mathbf{q}+\mathbf{G})\mathbf{r}}$ .
- `lmax_wave`: Sets the maximum value of  $l$  in the expansion of the wave function within the muffin-tin spheres.
- `g_par`: Always use option 1. This feature is not tested well. Don't change this parameter!!!
- `blocksize`: Controls the blocksize for the scalapack routines.
- `broadAC`: Adds a broadening within the response function.
- `omegaAC`: Controls the options for the frequency integration. Usually 16 points for the Gauss-Legendre integration is enough. The maximum frequency for the integration has to be higher than the band gap of the material. If an equally distant grid is chosen for the frequency points then no integration of the correlation energy is carried out.
- `calc_head,calc_wings`: Controls whether the head and wings are set to zero or calculated using  $\mathbf{k}\cdot\mathbf{p}$  (by using the mommat files). Mommat files are also required to run the program if the head or wings are set to 0!!!

- `freq_opt`: Controls whether the frequency loop is an outer loop or an inner loop. By setting this option to 1 the computational time can be reduced by a factor equal to the number of frequency points, but at the same time the memory requirement grows by the same factor.

**optimize.job:**

```
#!/bin/csh -f

if (-e HFRPA.clmsum && ! -z HFRPA.clmsum) then
  x dstart -super
endif
if (-e HFRPA.clmup && ! -z HFRPA.clmup) then
  x dstart -super -up
  x dstart -super -dn
endif

foreach i ( \
           HFRPA_vol__-9.0 \
           HFRPA_vol__-6.0 \
           HFRPA_vol__-3.0 \
           HFRPA_vol___0.0 \
           HFRPA_vol___3.0 \
           HFRPA_vol___6.0 \
           HFRPA_vol___9.0 \
)

rm HFRPA.struct          # NFS-bug
cp $i.struct HFRPA.struct

clmextrapol_lapw
if (-e HFRPA.clmup && ! -z HFRPA.clmup) then
  clmextrapol_lapw -up
  clmextrapol_lapw -dn
endif

#-----Semi_local_potential-----
run_lapw -ec 0.000001 -cc 0.000001 # -p -it
# runsp_lapw -ec 0.0001 -cc 0.0001 # -p -it
#   min -I -j "run_lapw -I -fc 1.0 -i 40 "
#-----Semi_local_potential-----
```

```

#-----Input_preparation_for_RPA-----
mkdir AC_$i
cp HFRPA.struct AC_$i/struct
cp HFRPA.vns AC_$i/vns
cp HFRPA.vsp AC_$i/vsp
cp HFRPA.in1 AC_$i/in1_AC
cp HFRPA.inACkgen AC_$i/inACkgen
cp HFRPA.inop AC_$i/inop
cp HFRPA.input AC_$i/input
cd AC_$i
/psi19/ferenc/ACFDT/2nd_TRY/execACkgen
/psi19/ferenc/ACFDT/2nd_TRY/execlapw1optic
cd ..
#-----Input_preparation_for_RPA-----

#-----Saving_semi_local_run-----
save SLOUT_$i
#-----Saving_semi_local_run-----

#-----Hartree_Fock_run-----
if (-e HFRPA.vectorhf) then
    rm -f HFRPA.vectorhf
endif
run_lapw -hf -nonself
# runsp_lapw -hf -nonself
save HFOUT_$i
rm -f HFRPA.vectorhf*
rm -f HFRPA.energyhf*
#-----Hartree_Fock_run-----

#    set stat = $status
#    if ($stat) then
#        echo "ERROR status in" $i
#        exit 1
#    endif
#    save_lapw -f -d XXX $i
end

```

This file has to be adapted to the individual needs before running it.  
Some comments on running and setting up the ACFDT calculations:

- The preliminary DFT calculations have to be converged very accurately (usually by running with the option "run\_lapw -ec 0.000001 -cc 0.000001").
- Depending on the case several hundreds of computational cores are needed for the calculations, i.e. solid Kr with an  $RK_{max}$  of 9.8,  $G_{max}$  of  $8.0 \text{ Ryd}^{-1}$  and a  $k$  mesh of  $4 \times 4 \times 4$  needs approximately 500 seconds on 1024 cores.  $k$  mesh and  $RK_{max}$  convergence has to be tested carefully from the bottom up for each compound. The calculation time increases very strongly with the number of  $k$  points and a higher  $RK_{max}$ , so the convergence of the  $k$  mesh and  $RK_{max}$  have to be tested carefully from the bottom up for each compound.

## References

- [1] P. Hohenberg and W. Kohn, *Physical Review* **136**, B864 (1964).
- [2] L. H. Thomas, *Proc. Cambridge Philos. Soc.* **23**, 542 (1927).
- [3] E. Fermi, *Z. Phys.* **61**, 126 (1930).
- [4] W. Kohn and L. Sham, *Physical Review* **140**, A1133 (1965).
- [5] G. Gilat and N. Bharatiya, *Physical Review B* **12**, 3479 (1975).
- [6] J. Phillips, *Physical Review* **112**, 685 (1958).
- [7] V. Heine, *Solid State Physics - Advances in Research and Applications* **24**, 1 (1970).
- [8] P. Blöchl, *Physical Review B* **50**, 17953 (1994).
- [9] G. Kresse and D. Joubert, *Physical Review B - Condensed Matter and Materials Physics* **59**, 1758 (1999).
- [10] J. Slater, *Physical Review* **51**, 840 (1937).
- [11] O. Andersen, *Solid State Communications* **13**, 133 (1973).
- [12] O. Andersen, *Physical Review B* **12**, 3060 (1975).
- [13] D. J. Singh and L. Nordström, *Plane waves, pseudopotentials and the LAPW method*, 2nd ed. (Springer, New York, 1994).
- [14] E. Sjöstedt, L. Nordström, and D. Singh, *Solid State Communications* **114**, 15 (2000).
- [15] D. Singh, *Physical Review B* **43**, 6388 (1991).
- [16] D. Ceperley and B. Alder, *Physical Review Letters* **45**, 566 (1980).
- [17] J. Perdew, K. Burke, and M. Ernzerhof, *Physical Review Letters* **77**, 3865 (1996).
- [18] C. S. Wang and B. M. Klein, *Physical Review B* **24**, 3393 (1981).
- [19] C. S. Wang and B. M. Klein, *Physical Review B* **24**, 3417 (1981).
- [20] J. Heyd, J. E. Peralta, G. E. Scuseria, and R. L. Martin, *The Journal of Chemical Physics* **123**, (2005).

- [21] R. T. Sharp and G. K. Horton, *Physical Review* **90**, 317 (1953).
- [22] J. B. Krieger, Y. Li, and G. J. Iafrate, *Physical Review A* **45**, 101 (1992).
- [23] A. D. Becke and E. R. Johnson, *The Journal of Chemical Physics* **124**, (2006).
- [24] J. C. Slater, *Physical Review* **81**, 385 (1951).
- [25] J. C. Slater, *Physical Review* **82**, 538 (1951).
- [26] F. Tran and P. Blaha, *Physical Review Letters* **102**, 226401 (2009).
- [27] A. D. Becke and M. R. Roussel, *Physical Review A* **39**, 3761 (1989).
- [28] D. Koller, F. Tran, and P. Blaha, *Physical Review B* **85**, 155109 (2012).
- [29] D. R. Hartree, *Proc. Cambridge Phil. Soc.* **24**, 89 (1928).
- [30] V. Fock, *Z. Phys.* **61**, 126 (1930).
- [31] C. Møller and M. Plesset, *Physical Review* **46**, 618 (1934).
- [32] W. H. Adams, *Physical Review* **156**, 109 (1967).
- [33] C. D. Sherrill and H. F. Schaefer III, **34**, 143 (1999).
- [34] O. Sinanoglu, *The Journal of Chemical Physics* **36**, 706 (1962).
- [35] C. J. Cramer, *Essentials of Computational Chemistry* (Chichester: John Wiley and Sons, 2002).
- [36] J. A. Pople, J. S. Binkley, and R. Seeger, *International Journal of Quantum Chemistry* **10**, 1 (1976).
- [37] H. Yukawa, *Proc. Phys. Math. Soc. Jpn.* **17**, 48 (1935).
- [38] J. Heyd, G. E. Scuseria, and M. Ernzerhof, *The Journal of Chemical Physics* **118**, 8207 (2003).
- [39] J. Heyd and G. E. Scuseria, *The Journal of Chemical Physics* **120**, 7274 (2004).
- [40] J. Heyd and G. E. Scuseria, *The Journal of Chemical Physics* **121**, 1187 (2004).



- [41] M. Ernzerhof and G. E. Scuseria, *The Journal of Chemical Physics* **110**, 5029 (1999).
- [42] C. Adamo and V. Barone, *The Journal of Chemical Physics* **110**, 6158 (1999).
- [43] R. Kubo, *Journal of the Physical Society of Japan* **12**, 570 (1957).
- [44] F. Dyson, *Physical Review* **75**, 486 (1949).
- [45] D. Bohm and D. Pines, *Physical Review* **82**, 625 (1951).
- [46] D. Pines and D. Bohm, *Physical Review* **85**, 338 (1952).
- [47] D. Bohm and D. Pines, *Physical Review* **92**, 609 (1953).
- [48] S. L. Adler, *Physical Review* **126**, 413 (1962).
- [49] N. Wiser, *Physical Review* **129**, 62 (1963).
- [50] D. Pines and P. Nozieres, *The theory of quantum liquids* (Benjamin, New York, 1966).
- [51] P. Ziesche and G. Lehmann, *Elektronentheorie der Metalle*, 1st ed. (Springer, Berlin, 1983).
- [52] V. Ambegaokar and W. Kohn, *Physical Review* **117**, 423 (1960).
- [53] R. Del Sole and E. Fiorino, *Physical Review B* **29**, 4631 (1984).
- [54] D. Langreth and J. Perdew, *Solid State Communications* **17**, 1425 (1975).
- [55] O. Gunnarsson and B. Lundqvist, *Physical Review B* **13**, 4274 (1976).
- [56] D. Langreth and J. Perdew, *Physical Review B* **15**, 2884 (1977).
- [57] L. Landau and E. Lifshitz, *Statistical Mechanics*, 2nd ed. (Pergamon Press, Oxford, New York, 1969).
- [58] J. Dobson, M. Marques, C. Ullrich, F. Noqueira, A. Rubio, K. Burke, and E. Gross, *Time-dependent Density Functional Theory*, 1st ed. (Springer, Berlin, 2006).
- [59] J. Harl, *The linear response function in density functional theory: Optical spectra and improved description of the electron correlation*, PhD thesis, University of Vienna, 2008.

- [60] M. Hazewinkel, *Encyclopaedia of Mathematics*, 1st ed. (Springer, Berlin, 2001).
- [61] D. Werner, *Funktionalanalysis*, 7th ed. (Springer Verlag, Berlin, 2011).
- [62] F. R. Gantmacher, *The Theory of Matrices 1* (Chelsea, New York, 1959).
- [63] L. Hedin, *Physical Review* **139**, A796 (1965).
- [64] F. Aryasetiawan and O. Gunnarsson, *Reports on Progress in Physics* **61**, 237 (1998).
- [65] A. L. Fetter and J. D. Walecka, *Quantum theory of many-particle systems* (McGraw-Hill, New York, 1971).
- [66] F. J. Dyson, *Physical Review* **75**, 1736 (1949).
- [67] L. Hedin, *Physical Review* **139**, A796 (1965).
- [68] J. Inkson, *Many body theory of solids: an introduction* (Plenum, New York, 1983).
- [69] H. Jiang, *Acta Phys. Chim. Sin.* **26**, 1017 (2010).
- [70] M. Shishkin and G. Kresse, *Physical Review B* **75**, 235102 (2007).
- [71] G. Baym and L. Kadanoff, *Physical Review* **124**, 287 (1961).
- [72] H. J. de Groot, P. A. Bobbert, and W. van Haeringen, *Physical Review B* **52**, 11000 (1995).
- [73] B. Holm and U. von Barth, *Physical Review B* **57**, 2108 (1998).
- [74] M. Shishkin, M. Marsman, and G. Kresse, *Physical Review Letters* **99**, 246403 (2007).
- [75] M. van Schilfgaarde, T. Kotani, and S. Faleev, *Physical Review Letters* **96**, 226402 (2006).
- [76] E. Salpeter and H. Bethe, *Physical Review* **84**, 1232 (1951).
- [77] G. Strinati, *Physical Review Letters* **49**, 1519 (1982).
- [78] G. Strinati, *Physical Review B* **29**, 5718 (1984).
- [79] G. Strinati, *La Rivista Del Nuovo Cimento Series 3* **11**, 1 (1988).

- [80] S. Albrecht, L. Reining, R. Del Sole, and G. Onida, *Physical Review Letters* **80**, 4510 (1998).
- [81] S. Albrecht, G. Onida, and L. Reining, *Physical Review B - Condensed Matter and Materials Physics* **55**, 10278 (1997).
- [82] S. Albrecht, L. Reining, R. Del Sole, and G. Onida, *Physica Status Solidi (A) Applied Research* **170**, 189 (1998).
- [83] M. Rohlfing and S. Louie, *Physical Review B - Condensed Matter and Materials Physics* **62**, 4927 (2000).
- [84] J.-W. Van der Horst, P. Bobbert, M. Michels, G. Brocks, and P. Kelly, *Physical Review Letters* **83**, 4413 (1999).
- [85] P. Blaha, K. Schwarz, G. K. H. Madsen, D. Kvasnicka, and J. Luitz, *WIEN2K: An Augmented Plane Wave plus Local Orbitals Program for Calculating Crystal Properties* (Vienna University of Technology, Austria, 2001).
- [86] H. Jiang, R. Gómez-Abal, X.-Z. Li, C. Meisenbichler, C. Ambrosch-Draxl, and M. Scheffler, *Computer Physics Communications* **184**, 348 (2013).
- [87] G. Baldacchini and R. M. Montoreali, *Opt. Mat.* **16**, 53 (2001).
- [88] V. V. Ter-Mikirtychev and T. Tsuboi, *Prog. Quant. Electr.* **20**, 219 (1996).
- [89] C. A. Hutchinson, *Physical Review* **75**, 1769 (1949).
- [90] N. W. Lord, *Physical Review Letters* **1**, 170 (1958).
- [91] J. H. Schulman and W. D. Compton, *Color Centers in Solids* (Pergamon, New York, 1962).
- [92] W. B. Fowler, *The Physics of Colour Centers* (Academic, New York, 1968).
- [93] A. M. Stoneham, *Theory of Defects in Solids* (Clarendon Press, Oxford, 1975).
- [94] L. V. E. Caldas, M. R. Mayhugh, and T. G. Stoebe, *J. Appl. Phys.* **54**, 3431 (1983).
- [95] G. Singh and T. E. Gallon, *Solid State Commun.* **51**, 281 (1984).

- [96] G. Roy, G. and Singh and T. E. Gallon, *Surface Science* **152**, 1042 (1985).
- [97] M. Piacentini, D. W. Lynch, and C. G. Olson, *Physical Review B* **13**, 5530 (1976).
- [98] F. Karsai, P. Tiwald, R. Laskowski, F. Tran, J. Burgdörfer, L. Wirtz, and P. Blaha, *Physical Review B - Condensed Matter and Materials Physics* **89** (2014).
- [99] W. Holton, H. Blum, and C. Slichter, *Physical Review Letters* **5**, 197 (1960).
- [100] W. Holton and H. Blum, *Physical Review* **125**, 89 (1962).
- [101] L. Miller and R. Bube, *Journal of Applied Physics* **41**, 3687 (1970).
- [102] M. Mayhugh, R. Christy, and N. Johnson, *Journal of Applied Physics* **41**, 2968 (1970).
- [103] R. Christy and M. Mayhugh, *Journal of Applied Physics* **43**, 3216 (1972).
- [104] T. Marolo, G. Baldacchini, V. Kalinov, and R. Montereali, *Physica Status Solidi C: Conferences* **2**, 367 (2005).
- [105] R. K. Dawson and D. Pooley, *physica status solidi (b)* **35**, 95 (1969).
- [106] K. Schwartz, C. Trautmann, A. S. El-Said, R. Neumann, M. Toulemonde, and W. Knolle, *Physical Review B* **70**, 184104 (2004).
- [107] G. Baldacchini, A. T. Davidson, V. S. Kalinov, A. G. Kozakiewicz, R. M. Montereali, E. Nichelatti, and A. P. Voitovich, *J. Luminescence* **122-123**, 371 (2007).
- [108] M. R. Pederson and B. M. Klein, *Physical Review B* **37**, 10319 (1988).
- [109] G. Mallia, R. Orlando, C. Roetti, P. Ugliengo, and R. Dovesi, *Physical Review B* **63**, 235102 (2001).
- [110] C. Kölmel and C. S. Ewig, *J. Phys. Chem. B* **105**, 8538 (2001).
- [111] C. S. Ewig, J. Tellinghuisen, and M. H. Mendenhall, *Chem. Phys. Letters* **188**, 501 (1992).

- [112] A. S. Shalabi, A. M. El-Mahdy, M. A. Kamel, and H. Y. Ammar, *Physica B* **304**, 444 (2001).
- [113] Y. Ma and M. Rohlfing, *Physical Review B* **77**, 115118 (2008).
- [114] M. Bockstedte, A. Marini, O. Pankratov, and A. Rubio, *Physical Review Letters* **105**, 026401 (2010).
- [115] C. Attaccalite, M. Bockstedte, A. Marini, A. Rubio, and L. Wirtz, *Physical Review B* **83**, 144115 (2011).
- [116] P. Rinke *et al.*, *Physical Review Letters* **108**, 126404 (2012).
- [117] J. Lischner, J. Deslippe, M. Jain, and S. G. Louie, *Physical Review Letters* **109**, 036406 (2012).
- [118] F. Karsai, First-principles Investigations of the Dihydrides of Scandium, Yttrium, Lanthanum, and Lutetium, Master's thesis, Universität Wien, Vienna, 2011.
- [119] P. Cortona, *Physical Review B* **46**, 2008 (1992).
- [120] E. Fermi, *Nuclear Physics* (University of Chicago Press, 1950).
- [121] A. F. Fix, F. U. Abuova, R. I. Eglitis, E. A. Kotomin, and A. T. Akilbekov, *Physica Scripta* **86**, 035304 (2012).
- [122] R. Laskowski, N. E. Christensen, P. Blaha, and B. Palanivel, *Physical Review B* **79**, 165209 (2009).
- [123] R. Laskowski and P. Blaha, *Physical Review B* **82**, 205104 (2010).
- [124] F. Aquilante *et al.*, *J. Comput. Chem.* **31**, 224 (2010).
- [125] R. P. Feynman, *Physical Review* **97**, 660 (1955).
- [126] H. Fröhlich, *Advances in Physics* **3**, 325 (1954).
- [127] E. Mollwo, *Nachr. Ges. Wiss. Göttingen* **97** (1931).
- [128] H. Ivey, *Physical Review* **72**, 341 (1947).
- [129] M. Malghani and D. Smith, *Physical Review Letters* **69**, 184 (1992).
- [130] H. Fröhlich, *Zeitschrift für Physik* **80**, 819 (1933).
- [131] F. Stöckmann, *Die Naturwissenschaften* **39**, 246 (1952).

- [132] F. Stöckmann, *Die Naturwissenschaften* **39**, 226 (1952).
- [133] R. Wood, *Journal of Physics and Chemistry of Solids* **26**, 615 (1965).
- [134] D. Smith and M. Malghani, *Nuclear Instruments and Methods in Physics Research, Section B: Beam Interactions with Materials and Atoms* **141**, 42 (1998).
- [135] J. Vinti, *Physical Review* **41**, 432 (1932).
- [136] C. J. Buchenauer and D. B. Fitchen, *Physical Review* **167**, 846 (1968).
- [137] B. S. Gourary and F. J. Adrian, *Physical Review* **105**, 1180 (1957).
- [138] D. Y. Smith and M. Inokuti, *Radiation Effects and Defects in Solids* **155**, 43 (2001).
- [139] R. D. Shannon, *Acta Crystallographica Section A* **32**, 751 (1976).
- [140] R. H. Bartram, A. M. Stoneham, and P. Gash, *Physical Review* **176**, 1014 (1968).
- [141] A. Smakula, N. C. Maynard, and A. Repucci, *Physical Review* **130**, 113 (1963).
- [142] F. Birch, *Physical Review* **71**, 809 (1947).
- [143] G. Kresse and J. Hafner, *Physical Review B* **49**, 14251 (1994).
- [144] G. Kresse, *Journal of Non-Crystalline Solids* **192-193**, 222 (1995).
- [145] G. Kresse and J. Furthmüller, *Computational Materials Science* **6**, 15 (1996).
- [146] G. Kresse and J. Furthmüller, *Physical Review B* **54**, 11169 (1996).
- [147] Y. S. Touloukian, R. K. Kirby, R. E. Taylor, and P. D. Desai, *Thermal Expansion—Metallic Elements and Alloys, Thermophysical Properties of Matter, Vol. 12* (Plenum, New York, 1975).
- [148] M. Levinshtein, S. Rumyantsev, and M. Shur, *Handbook Series on Semiconductor Parameters, Vol 1.* (World Scientific, Singapore, 1996).
- [149] M. Betzinger, C. Friedrich, A. Görling, and S. Blügel, *Physical Review B - Condensed Matter and Materials Physics* **85** (2012).

- [150] J. Harl, L. Schimka, and G. Kresse, *Physical Review B* **81**, 115126 (2010).
- [151] R. L. Smith and J. W. Miser, *Compilation of the properties of lithium hydride* (NASA, 1963).
- [152] K. Rościszewski, B. Paulus, P. Fulde, and H. Stoll, *Physical Review B - Condensed Matter and Materials Physics* **60**, 7905 (1999), cited By 71.
- [153] K. H. Hellwege, *Landolt–Börnstein, New Series, Group III*, 2nd ed. (Springer, Berlin, 1966).
- [154] J. M. Besson, G. Weill, G. Hamel, R. J. Nelmes, J. S. Loveday, and S. Hull, *Physical Review B* **45**, 2613 (1992).
- [155] C. V. Briscoe and C. F. Squire, *Physical Review* **106**, 1175 (1957).
- [156] K. Marklund and S. A. Mahmoud, *Physica Scripta* **3**, 75 (1971).
- [157] C. Ambrosch-Draxl and J. Sofo, *Computer Physics Communications* **175**, 1 (2006).
- [158] W. Press, *Numerical Recipes in Fortran 90. The Art of Parallel Scientific Computing* (Cambridge University Press, 1996).
- [159] J. Adams, W. Brainerd, R. Hendrickson, R. Maine, J. Martin, and B. Smith, *The Fortran 2003 Handbook: The Complete Syntax, Features and Procedures* (Springer, 2009).
- [160] S. Huzinaga, L. Seijo, Z. Barandiarán, and M. Klobukowski, *J. Chem. Phys.* **86**, 2132 (1986).
- [161] L. Seijo and Z. Barandiarán, *The Ab Initio Model Potential Method: A Common Strategy for Effective Core Potential and Embedded Cluster Calculations* (World Scientific, Singapur, 1999), chap. 2, pp. 55–152.
- [162] H. M. Evjen, *Physical Review* **39**, 675 (1932).
- [163] T. H. Dunning, *J. Comput. Phys.* **90**, 1007 (1988).
- [164] J. Adachi and N. Kosugi, *B. Chem. Soc. Jpn.* **66**, 3314 (1993).
- [165] R. Bader and J. Platts, *J. Comput. Phys.* **107**, 8545 (1997).

- [166] A. Leitão, R. Capaz, N. Vugman, and C. Bielschowsky, *Journal of Molecular Structure: J. Mol. Struct-Theochem.* **580**, 65 (2002).
- [167] D. G. Truhlar, *Chem. Phys. Letters* **294**, 45 (1999).
- [168] P. L. Fast, M. L. Sanchez, and D. G. Truhlar, *J. Chem. Phys.* **111**, 2921 (1999).
- [169] D. Domínguez-Ariza, C. Sousa, F. Illas, D. Ricci, and G. Pacchioni, *Physical Review B* **68**, 054101 (2003).
- [170] G. Baldacchini, Relaxed excited states of color centers, in *Optical Properties of Excited States in Solids*, edited by B. Bartolo and C. Beckwith, , NATO ASI Series Vol. 301, pp. 255–303, Springer US, 1992.
- [171] M. Nisoli *et al.*, *Physical Review Letters* **77**, 3463 (1996).
- [172] H. Bilz and W. Kress, *Phonon Dispersion Relations in Insulators* (Springer-Verlag, Berlin Heidelberg, 1979).
- [173] A. Schüller *et al.*, *Physical Review A* **82**, 062902 (2010).
- [174] G. A. Russell and C. C. Klick, *Physical Review* **101**, 1473 (1956).



# Curriculum Vitae

Name: Ferenc Karsai  
Surname: Karsai

Born on September 9th, 1985 in Budapest, Hungary as the child of Ferenc Karsai and Tar Beata.

Hungarian citizen.

1992–1993: Elementary school in Stockerau, Austria.

1994–1995: Elementary school in Kiskunf elegyhaza, Hungary.

1996–2004: Grammar school in Stockerau, Austria.

2004–2005: Grammar school in Vienna, Austria.

2006–2009: Bachelor studies of chemistry at the University of Vienna.

2009–2011: Master studies of chemistry at the University of Vienna.

Since Nov. 2011: Doctoral studies of technical chemistry at the Technical University Vienna